Study of some Factors Affecting the ~~Operating Characteristics~~ of Microstrip Gas ~~Counters~~ in an ~~ATLAS~~ Environment

Phillip Brian Bignall

Department of Physics & Astronomy,

University College London

A thesis submitted to University College London in accordance with the requirements for the degree of Doctor of Philosophy

September 1995

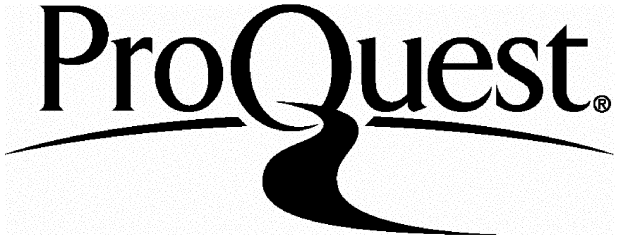

Study of some Factors Affecting the Operating Characteristics of Microstrip Gas Counters in an ATLAS Environment

Abstract

A study of neutron-induced interaction processes in MicroStrip Gas Counters is presented. The MicroStrip Gas Counter (MSGC) is a particle detector intended for use as part of the proposed ATLAS experiment at the LHC in CERN. An overview of ATLAS is presented and the principles of operation of the MSGC are described.

Results from the operation of an MSG test chamber in the lab are presented. The results from an experiment to measure the signal produced in MSGCs by low energy neutrons at the ISIS synchrotron are presented and an account is given of a Monte Carlo model which simulates neutron-induced signals in MSGCs. The results from the model are compared with those from the neutron irradiation experiment at ISIS.

The model is used to make predictions of the neutron-induced signal in MSGCs at ATLAS where a high background flux of low energy neutrons is expected. The model makes predictions of the spectrum and rate of neutron-induced counts and calculates the neutron-induced occupancy and charge loading of MSGCs in ATLAS. The model predicts that neutron interactions in the chamber will result in very large pulses being produced. The model predicts that these pulses could result in an increase in the occupancy of MSGCs of up to 7 % and an increase in charge loading of up to 160 %.

Contents

List of Figures

List of Tables

Chapter 1

Introduction

1.1 An overview of LHC

The **L**arge **H**adron **C**ollider is proposed as a high energy proton - proton collider producing a centre of mass energy of $\sqrt{s} \approx 14$ TeV [1] with a luminosity of greater than $10^{34} cm^{-2} sec^{-1}$.

It is to be constructed at CERN in Geneva, Switzerland using the tunnel of the existing LEP electron-positron collider. The LHC will have four beam crossing points, two of which will be occupied by the experiments ATLAS (**A** Toroidal **LHC** Apparatu**S**) and CMS (**C**ompact **M**uon **S**olenoid). With the much higher energies available to the LHC, a whole new range of physics studies may be realised [2].

- Higgs searches. The Higgs mechanism is a theory within the Standard Model whereby particles acquire mass by spontaneous symmetry breaking. The neutral Higgs boson predicted by the Standard Model couples to other particles depending on their mass, coupling weakly to light objects (u, d quarks) and more strongly to heavier objects (b, t quarks). This may be why the Higgs has not been discovered to date, as heavy particles are in themselves difficult to produce.

  Assuming a light Higgs mass $m_H < 180$ GeV, the Higgs may be observable via the

channels H $\rightarrow \gamma\gamma$ and H $\rightarrow ZZ^* \rightarrow llll$ with the two photon channel indicating 80 GeV $< m_H <$ 130 GeV and the four lepton channel indicating 120 GeV $< m_H <$ 180 GeV. For a heavy Higgs with 80 GeV $< m_H <$ 800 GeV, the four lepton channel provides the greatest potential for Higgs discovery. At higher masses, channels which are not purely leptonic begin to become dominant.

- CP violation. CP violation has already been observed through neutral kaon decays where the kaon decays to either two or three pions with a different lifetime in each case. Proton-proton collisions are a rich source of B particles and at LHC the opportunity arises to study CP violation effects using the decays B $\rightarrow$ J/ψK_d^0 and B $\rightarrow \pi^+\pi^-$.

- Supersymmetric particles. The Supersymmetry theory unifies all forces including gravity and proposes symmetries between bosons and fermions such that for every boson there is a fermion equivalent and vice-versa. This gives us Winos, gluinos and photinos as well as squarks and sleptons. Currently the lower limits on squark and gluino masses are 126 and 141 GeV respectively. LHC will enable the search for these and other supersymmetric particles to continue up to a mass of 1 TeV [3].

- Top quark physics. LHC detector experiments will be in a position to build on the evidence for the existance of the top quark provided by the Tevatron at Fermilab [4]. This will include measurements of the mass of the top quark.

1.2 The ATLAS detector

ATLAS has been designed to be a general purpose detector for proton-proton collisions in LHC operating at luminosities greater than $10^{34} cm^{-2} sec^{-1}$ and has undergone a number of modifications since its first conception [2, 6, 1]. The ATLAS detector as a whole (see Fig. 1.2) may be broken down into three main subsystems: the Calorimeter, the Muon Spectrometer and the Inner Tracking Detector.

1.2.1 The Calorimeter

The ATLAS calorimeter consists of two systems; the Electromagnetic Calorimeter which functions principly to reconstruct and identify photons and electrons; and the Hadron Calorimeter for jet identification.

In ATLAS the em calorimeter will consist of a lead absorber interleaved with thin layers of liquid argon which act as a counter. This configuration has been chosen for radiation hardness, stability and read-out speed. The configuration also includes a preshower detector for determining photon direction and particle identification. These will be installed in both the barrel and end-cap regions and will cover a pseudorapidity range of $0 <| \eta |< 1.4$ in the barrel and $1.4 <| \eta |< 3.2$ in the end cap.

In the end cap, the hadron calorimeter uses a system comprising of liquid argon sampling interleaved with copper absorbers. The pseudorapidity coverage of the end cap calorimeter extends over the range $1.5 <| \eta |< 3.2$.

The construction of the forward calorimeter uses liquid argon technology and comprises one em module and two hadronic modules and will cover the pseudorapidity range $3.2 <| \eta |< 4.9$.

The Hadron barrel calorimeter will use a system of steel absorber plates interleaved with scintillator tiles which will be read out using wavelength shifting fibres. A set of fibres is then grouped together onto a photomultiplier to form a read-out cell.

1.2.2 The Muon Spectrometer

The proposed muon spectrometer for ATLAS includes three superconducting air-core toroid magnets, tracking detectors and a dedicated trigger system. The super-conducting magnets, two End Cap Toroids and a Barrel Toroid are 5.6 and 26 metres in length respectively and are designed to operate at a temperature of 4.5K with a further 2K temperature margin above this.

The muon spectrometer is required to give good resolution over a p_T range from 5 GeV

to greater than 1000 GeV. Precision measurements will be made using Monitored Drift Tube (MDT) chambers [1] and Cathode Strip Chambers (CSCs) [1, 5]. Resistive Plate Chambers (RPCs) [1, 5] and Thin Gap Chambers (TGCs) [1] will provide information for the triggering system as well as the second coordinate for determining muon tracks.

The chambers will be read out using a multiplexed digital read-out system which is required to measure drift times to an accuracy of 1 ns.

1.2.3 The Inner Tracking Detector

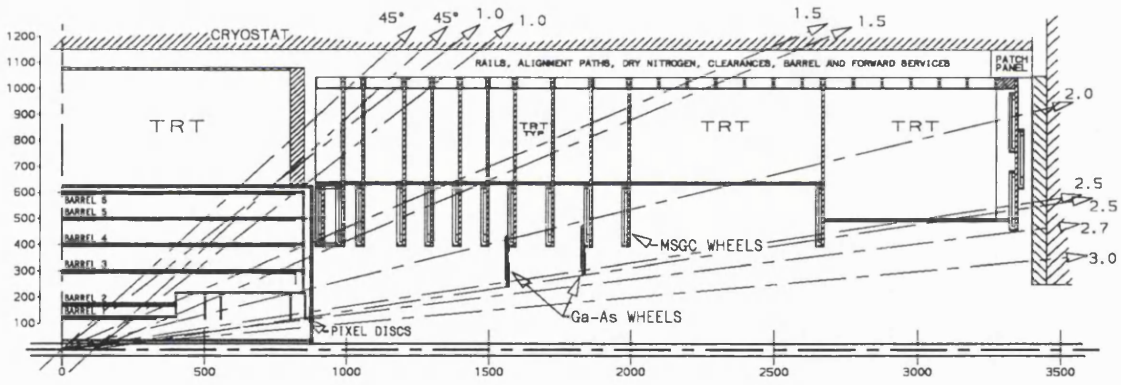

Figure 1.1: The ATLAS inner tracking detector as defined in [1] .

The inner tracking detector (Fig. 1.1) is to have a length of 6.8m and a radius of 1.06m and will be surrounded by a solenoidal coil which will produce a magnetic field of 2T. The proposed design uses a combination of several different technologies in order to meet the performance specifications and to provide accurate, high resolution track reconstruction.

- The **Semi-Conductor Tracker** will consist of silicon strip detectors in the barrel region to provide large area high precision tracking; and silicon pixel detectors in the forward region close to the beam crossing point. In addition, there are two wheels of radiation hard Gallium Arsenide detectors in the forward direction. Both silicon and GaAs detectors operate on the principle of charged particles creating ionization in the depletion zone of a reverse biased p-n junction.

- The **Transition Radiation Tracker** will be made up of a system of straw tube transition radiation detectors in the barrel and forward regions positioned between 0.5m and 1.1m from the beam pipe. Transition radiation detectors use the property that relativistic charged particles emit radiation when crossing the boundary between two media with different dielectric constants. Straw tubes are then employed to detect the radiation. This system will provide large area tracking and electron identification.

- **MicroStrip Gas Counters** measure position by means of the ionization deposited by a particle during its passage through a gas and are proposed for use in the forward region to provide large area, high precision tracking[1]. We describe the role they fulfill in more detail later in section 1.3.

Performance characteristics for each of these detector modules are displayed in Table 1.1.

1.2.4 Triggering and DAQ

The expected trigger rates, bunch crossing frequency and the amount of data produced by the detectors lay down the requirements for the ATLAS trigger system. At LHC luminosities a vast number of events will be generated, a large proportion of which will be 'background' events - of no interest with respect to the physics that is to be studied using the ATLAS detector. Therefore to make analysis easier and to reduce storage space, some way has to be found to reject the unwanted background before the data is stored and this is the purpose of

[1] Currently MSGCs are competing with silicon strips for use in this region.

Detector System	Resolution (μm)	Pseudorapidity Coverage
Si Pixels	$\sigma_{R\phi} = 14$	$\pm$ 2.5
	$\sigma_z = 87$	
	$\sigma_R = 14$	
Si Strips	$\sigma_{R\phi} = 15$	$\pm$ 1.4
	$\sigma_R = 770$	
GaAs Strips	$\sigma_{R\phi} = 10$	2.0 - 2.5
	$\sigma_R = 1200$	
MSGC	$\sigma_{R\phi} = 35$	1.4 - 2.5
	$\sigma_R = 1800$	
TRT	$\sigma_{R\phi} = 170$	$\pm$ 2.5

Table 1.1: Resolution criteria and pseudorapidity coverage for subsystems of the inner tracker [1].

the trigger system. This is achieved by looking for signatures of the interactions of interest in isolated detector systems. The trigger system will operate in three stages or levels:

1. The level 1 trigger (LVL1) will select events based on data from some of the muon and calorimeter subdetectors only. LVL1 will be capable of accepting data at the full LHC bunch crossing rate (40 MHz). The event selection algorithms must reduce this volume of data such that the output rate of LVL1 does not exceed 100 kHz - the maximum acceptance rate of the level 2 trigger.

2. The level 2 trigger (LVL2) will select an event using data from certain subsystems of the muon detector, calorimeters and the inner tracker but only if that event has already been accepted by LVL1. There will be three steps to data processing in LVL2.

   (a) Feature extraction, where data is converted from basic cell information (eg: pulse height on a given channel) to information based on physical effects such as the

integrated charge deposited in the detector by a specific particle.

(b) Object building, where features are combined for each region of interest (RoI) which is an area indicated by LVL1 and identifies for example, large energy deposits in a certain part of a detector subsystem. The combined data is used to provide information on particle characteristics such as energy and direction.

(c) Objects for all RoIs are combined and events are accepted according to the selection criteria.

LVL2 must reduce the rate of events from 100 kHz to the level 3 trigger maximum acceptance rate (1 kHz).

3. The level 3 trigger (LVL3) will use the data from all detector subsystems which it receives via an event builder which has the task of reconstructing events from the data. Only events accepted by LVL1 and LVL2 will reach the event builder and level 3 trigger. LVL3 will use a 'farm' of processors to select events by looking for specific physics signatures. LVL3 must reduce the event rate to 100 Hz before the event data are finally stored.

1.3 MSGCs and ATLAS

This work is particularly concerned with studying the performance of the MSGC proposed for use in the forward region of the ATLAS inner tracker. The relevance of MSGCs to fulfill this role was based on a number of considerations, principly:-

1. The radiation levels in the forward region are very high and so a radiation hard detector is required. The operation of MSGCs is relatively independent of the microscopic structure of its components and is thus unlikely to be affected by radiation damage.

2. The spatial precision required in the forward region is considerably less than that needed for detectors close to the beam crossing point. MSGCs with a 200 μm pitch have a spatial precision of $\sim$ 40 μm which is within design requirements.

3. MSGC modules are relatively inexpensive compared to other technologies.

MSGCs are required to meet the following performance specifications in order for them to be a viable option for use in ATLAS.

- A spatial precision of 40μ or better is required for accurate track reconstruction.
- Inside the inner tracker cavity, the high luminosity of the LHC will produce a charged particle flux of

$$N \approx \frac{2 \times 10^9}{r^2} cm^{-2} sec^{-1} \tag{1.1}$$

  at a radius of r cm from the beam axis. MSGCs must be able to operate in this flux with minimal loss of performance due to detector dead time or aging.
- Inside the inner cavity there will be a low energy neutron albedo flux of about $2 \times 10^6\ cm^{-2}\ sec^{-1}$ as a result of leakage from the inner face of the calorimeter structure. The direction of these neutrons will be essentially isotropic. MSGCs must be able to withstand these high levels of neutron radiation and in addition, suffer an acceptable increase in occupancy from neutron induced background events.

In ATLAS, MSGCs will cover a radial distance of 40 - 100 cm from the beam line. Each wheel will consist of three planes ϕ, u and v. The anode and cathodes strips in the ϕ plane will run radially with respect to the beam line, with the u and v planes rotated through $\pm$ 15 mrad. Such a chamber geometry, known as 'keystone' geometry [7] is required to have uniform gain all the way along the strip pattern.

1.4 The Objective of this Study

ATLAS is designed as a general purpose detector for studying the physics of p-p collisions. This thesis will concentrate on development work for the MSGC proposed for use in the ATLAS inner tracker. Initially we will study basic properties of the MSGC including the

construction and layout of the detector and the theory behind its operation. We then present results illustrating the basic performance characteristics of MSGCs in the laboratory before moving on to study the performance of MSGCs in a high flux of low energy neutrons and present results obtained from these studies. This is followed by a description of a simulation model designed to predict neutron induced effects on MSGCs in ATLAS. We compare the results produced by the simulation with experimental data before moving on to make predictions of the neutron induced count rates, occupancies and charge loading of MSGCs in ATLAS.

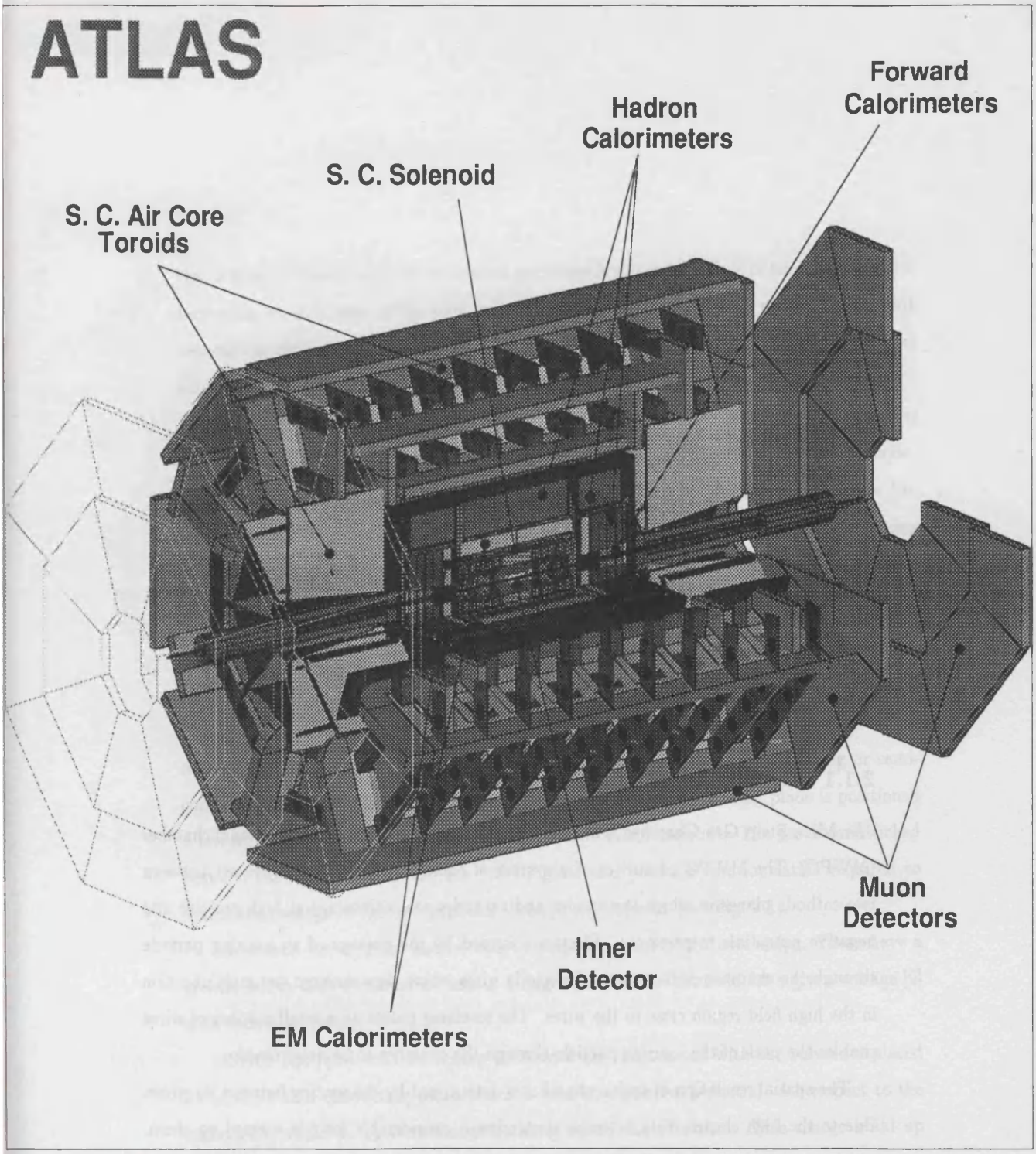

Figure 1.2: The ATLAS detector.[1]

Chapter 2

Theory of Operation of MSGCs

2.1 Introduction to the Microstrip Gas Chamber

2.1.1 Origins of the Microstrip Gas Chamber

The MicroStrip Gas Chamber is a development from the multi-wire proportional chamber (MWPC). The MWPC comprises of a system of equally spaced anode wires set between two cathode planes in which the anodes and cathodes are maintained at high positive and negative potentials respectively. Electrons formed by the passage of an ionizing particle through the chamber drift towards the anode wires where they undergo gas multiplication in the high field region close to the wires. The resulting pulses on a small number of wires enables the path of the ionizing particle through the chamber to be determined.

The spatial resolution of such a chamber is determined by the spacing between its wires. Due to the high electric field between electrodes, a considerable force is exerted on them, which may result in their displacement or deformation. In order that the wires are not displaced from their positions a tension must be applied to each wire. The critical tension (i.e. the tension that must be applied to prevent instability in the wires) varies with $\frac{1}{s^2}$, where s is the distance between the wires. Reducing the spacing between the wires means

that a greater tension needs to be applied and there is a greater chance of breaking the wire. Increasing the thickness of the wire will enable the wire to withstand a greater tension but reduces the electric field close to the wire, thus reducing the gain. Design of a MWPC thus requires a compromise between these two considerations.

A further problem for MWPC is that the positive ions produced by ionizing interactions, especially in the avalanche region close to the anode, take a long time to drift to the cathode. This cloud of positive charge will reduce the effective electric field and hence reduce the gain. This problem is referred to as 'space charge effect'. Reducing the drift space enough to produce a significant decrease in ion drift time would reduce the number of primary electrons produced by an ionizing particle in the gas and hence the detector efficiency.

2.1.2 Layout of an MSGC

The MSGC was first proposed by Oed in 1988 [8]. In its most basic form, the anode wires are replaced by a system of thin conducting strips deposited onto an insulating or semi-conducting substrate using photolithographic techniques. A conducting plane is positioned a few millimetres away from the substrate to form a drift cathode. The gas is sandwiched between the drift cathode and the MSGC plate and produces the ionization required to detect the passage of charged particles through the detector (see Fig. 2.1).

Interleaved between the anode readout strips are a set of cathode strips. These have a greater width than the anodes because a larger gain can be obtained for a given voltage [9] with such a geometry.

MSGCs equipped with insulating substrates are constructed with the substrate placed on top of a thin conducting plane which is kept at a positive potential with respect to the cathodes in order to prevent charge building up on the substrate. This charge build up is caused by positive ions travelling along field lines which end on the substrate and can severely reduce the gain of the detector over a period of operation [10, 11]. It is described more fully in section 2.5.1.

The basic MSGC design described above will produce the field map shown in Fig. 2.2

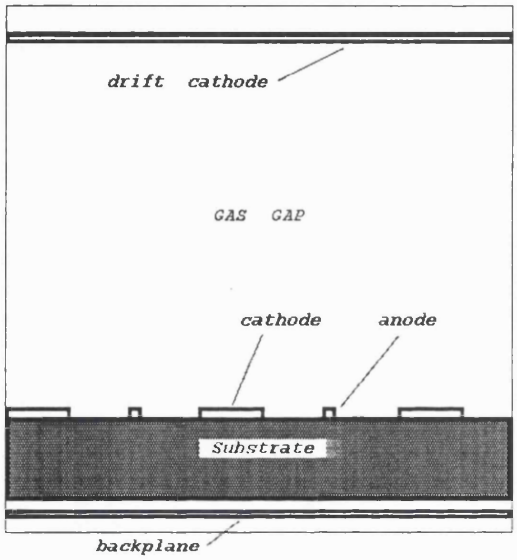

Figure 2.1: Layout of Microstrip Gas Chamber

[12].

MSGC operation can be summarized as follows

- A charged particle passes through the detector creating ion pairs along its path through the gas.
- The electrons so produced drift along the field lines until they reach the high field region close to the anode strips.
- Close to the anode strips the electrons are accelerated between collisions by the electric field to such an extent as to cause further ionization (avalanche multiplication). For a MSGC the maximum sustainable gas multiplication factor is typically a few thousand.
- The electrons are collected by the anodes producing a pulse whose length corresponds, ideally, to the drift time in the gas. A fraction of the positive ions drift sideways to-

wards the neighbouring cathode strips where they are rapidly collected. The remainder travel to the drift cathode in much the same way as in an MWPC. This reduces space charge effect, alleviating the problems of loss of gain and shortening the clearing time, i.e. the chambers may operate at substantially higher rates than MWPCs. Rate capabilities of up to 5×10^5 counts $mm^{-2}s^{-1}$ have been recorded for MSGC's [13]. At these counting rates, MWPCs suffer a significant loss of efficiency [14].

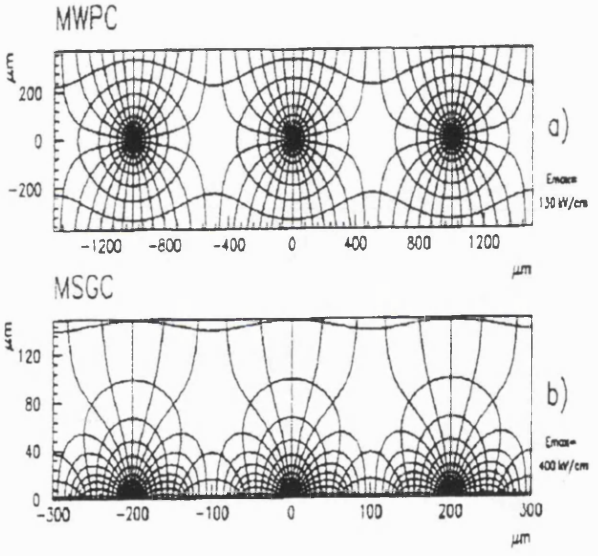

Figure 2.2: Typical electric field maps for a MWPC and a MSGC. [12]

The MSGC, having removed the limitation imposed by using wires maintained at a tension, can therefore yield a better spatial resolution than MWPC's because the separation between the sensing elements can be reduced considerably.

The following sections will outline some of the main factors that affect the operation of gas based detectors in general, and MSGCs in particular.

2.2 Theory of Ionization and Electron Drift

2.2.1 Factors governing Ion pair Creation

When a charged particle passes through a gas it undergoes collisions with atoms in the gas leaving a trail of excited and ionized gas atoms along its path. A fairly good approximation to the average energy per unit length of material deposited by an ionizing particle, is the Bethe-Bloch equation [15]

$$\frac{dE}{dX} = \frac{-KZ\rho}{A\beta^2}\left(\frac{1}{2}\ln\frac{2m(\gamma\beta c)^2}{I} - \beta^2 - \frac{\delta}{2}\right) \tag{2.1}$$

where

$$K = 4\pi z^2 N_A r_e^2 m_e c^2$$

Z,A, ρ and I are the atomic number, atomic weight, density and effective ionisation energy respectively of the material. r_e and m_e are the classical electron radius and the electron mass while z is the charge of the incident particle. δ is a density correction arising from relativistic effects and γ, the Lorentz factor is given by

$$\gamma = \frac{1}{\sqrt{1-\beta^2}} \tag{2.2}$$

where β is the velocity of the incident particle in units of c.

Excluding particles in the extreme relativistic region, equation 2.1 only depends on β. For low β, $\frac{dE}{dX}$ decreases with $\frac{1}{\beta^2}$ as the energy of the incident particle increases, reaching a minimum at $\gamma \approx 3.2$. Particles with energies in this region are referred to as Minimum Ionizing Particles[1]. As the energy increases further, $\frac{dE}{dX}$ begins to increase, an effect known as the relativistic rise.

Knowledge of the average energy required to create an ion pair in a particular gas, denoted by W_i, leads to an expression for the total number of ion pairs created in a given

[1] Referred to from now on in this work as mips

length of gas [14]

$$n_T = \frac{\Delta E}{W_i} \tag{2.3}$$

where ΔE is the energy lost in the gas. This equation assumes a uniform deposition of energy per unit length and also includes ion pairs produced by secondary ionization, in which an electron produced by the incident particle via ionization, receives enough energy to cause further (secondary) ionization. The number of ion pairs produced by direct interaction between the incident particle and the gas (primaries) is much smaller than the total number (primaries and secondaries) of ion pairs.

The spatial distribution of primary ion pairs is governed by Poissonian statistics. If n_p is the average number of primary ion pairs created in a given length, then the probability of an actual number n_i of primaries being created by an ionizing particle is

$$P_{n_i}^{n_p} = \frac{n_p^{n_i}}{n_i!} e^{-n_p} \tag{2.4}$$

This imposes limitations on the length of the drift space inside a chamber - a short drift space means that n_p is small and therefore the probability that an ionizing particle will produce no ion pairs in the chamber increases. In an ideal chamber, the chance of producing no ion pairs i.e. its inefficiency, is given by

$$1 - \epsilon = P_0^{n_p} = e^{-n_p} \tag{2.5}$$

For a chamber with drift space 3mm filled with 75 % argon, 25 % isobutane, the inefficiency due to this reason alone will be 5 $\times 10^{-3}$%. If the drift space is reduced to 1 mm, the inefficiency rises to 5.0 %.

The energy lost by an electron is not uniform but follows a probability distribution which can be approximated by the Landau distribution:

$$P(\lambda) = \frac{1}{\sqrt{2\pi}} e^{-0.5(\lambda + e^{-\lambda})} \tag{2.6}$$

where $\lambda = (\Delta \text{ E - } \Delta_{mp})/\frac{dE}{dX}$ is the normalized deviation from the most probable energy loss. Eq. 2.6 is plotted as Fig. 2.3, showing that some electrons may lose much more energy than

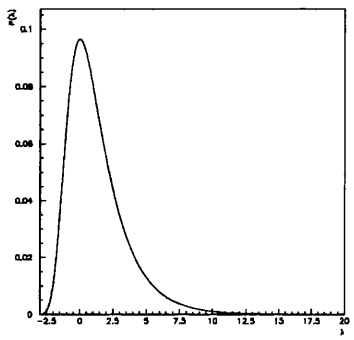

Figure 2.3: Landau energy loss distribution.

the average. This energy is transferred to other electrons via collisions and these electrons can then go on to produce more secondary ionization. Energetic electrons with energies of a few keV or more are referred to as delta rays [14].

Primary ion-pairs are thus not evenly distributed either in space or energy but are deposited in varying sized clusters randomly along the track of the particle. In thick detectors, or for slow moving incident particles, the large number of collisions results in a total energy deposition close to that predicted by eq. 2.1. Mips passing through thin gaseous detectors however, produce variable energy depositions obeying the above statistical behaviour.

2.2.2 The Effects of Electric and Magnetic fields on Electron Drift

The motion of electrons within a chamber is influenced by the presence of electric and magnetic fields. Obviously if no electric field were present, the chamber would not operate because electrons would not drift towards the electrodes and hence no signal would be collected. The inner tracker of ATLAS is situated within a 2T magnetic field for identification of high p_t tracks and the effects of magnetic fields must be taken into account.

A charged particle in a vacuum with an electric field **E** and a magnetic field **B** present

experiences a force given by the Lorentz equation:

$$\boldsymbol{F} = q(\boldsymbol{E} + \boldsymbol{v} \times \boldsymbol{B}) \tag{2.7}$$

However in a gaseous detector the electron does not move in a vacuum but in a volume filled with gas molecules. With no field present the electron follows a random path as it undergoes collisions with these molecules. When an electron moves in a gas with electric and magnetic fields present, the Lorentz equation must be modified to take into account the impulsive force an electron experiences when it undergoes a collision.

$$m\frac{\mathrm{d}\boldsymbol{v}}{dt} = q(\boldsymbol{E} + \boldsymbol{v} \times \boldsymbol{B}) + m\boldsymbol{A}(t) \tag{2.8}$$

where A(t) represents the instantaneous acceleration experienced by the electron due to collisions with atoms in the gas. This equation can be averaged in time and has a solution in which the electron drift velocity v_D is constant in time [16]. The acceleration due to collisions with molecules compensates the translational acceleration due to electric and magnetic fields. Hence eq. 2.8 becomes

$$m\frac{\mathrm{d}\boldsymbol{v}}{dt} = q(\boldsymbol{E} + \boldsymbol{v} \times \boldsymbol{B}) - m\frac{\boldsymbol{v_D}}{\tau} \tag{2.9}$$

For a constant electric field, ($\dot{\boldsymbol{v_D}} = 0$) the above equation can be solved to give

$$\boldsymbol{v_D} = \frac{\mu(\boldsymbol{E} + \mu(\boldsymbol{E} \times \boldsymbol{B}) + \mu^2(\boldsymbol{B}.\boldsymbol{E})\boldsymbol{B})}{1 + \mu^2 B^2} \tag{2.10}$$

where $\mu = q\frac{\tau}{m}$ and $\boldsymbol{v_D}$ is the velocity at which the electron cloud drifts towards the anodes in a gaseous detector. The instantaneous velocity of an individual electron is about an order of magnitude greater than this and invariably in a different direction. This equation describes the drift of low energy electrons in electric and magnetic fields. From this equation, we see that excluding the case where the magnetic field is parallel to the electric field, the electron cloud will have a velocity component in the $\mathbf{E} \times \mathbf{B}$ direction and will thus travel at an angle to the electric field. This angle, called the Lorentz angle α_L, can be derived from eq. 2.10 using standard vector identities

$$\tan\alpha_L = \frac{\mu B\sqrt{(\frac{1}{2}\mu^2 B^2 \sin 2\theta + \sin^2\theta)}}{(1 + \mu^2 B^2 \cos\theta)} \tag{2.11}$$

where θ is the angle between the electric and magnetic fields. For relatively small electric fields these equations hold true but in a real gas, the drift velocity tends to plateau out [14] and this simple treatment is in sufficient and more complex methods must be used [17, 18].

If an MSGC is operated in a magnetic field that is not parallel to the drift field, the charge deposited in the chamber may be spread over more than one detection cell and hence could reduce the efficiency of the chamber. However MSGCs in ATLAS will operate in a 2T magnetic field parallel to the drift field and hence these problems should not arise.

2.2.3 Diffusion of Electrons and Positive Ions

In the absence of an electric field, electrons produced by ionization will follow a random path transferring energy via collisions with gas molecules until they recombine. The charge density distribution resulting from this diffusion from the point of origin of the original primary cluster is Gaussian in shape. The standard deviation of the charge distribution in one dimension is given by

$$\sigma_x = \sqrt{2D_x t} \tag{2.12}$$

where D_x is the diffusion coefficient of the gas and t is the time after creation of the orignal primary. This equation also describes the diffusion of an electron cloud when an electric field is present. In this situation, D_L is the diffusion coefficient used to describe the distribution parallel to the field, and D_T is used for transverse diffusion.

Diffusion can improve the spatial precision of an MSGC because of the finite spread of the electron cloud. If the electron cloud covers a number of MSGC cells, the centre of the cloud and hence the position of the incident particle may thus be determined more accurately simply by finding the midpoint of the group of 'hit' strips. The charge collected on a strip is proportional to the amount of ionization produced in the gas volume above the strip. If the position is determined by taking a weighted average of the charge collected by a number of strips, the spatial precision may be improved further.

2.3 Gain in Gaseous Detectors

MSGC's (like MWPC's and drift chambers) have an electric drift field so that electrons created by the ionizing particle will drift to the anodes. Close to the anodes, they will undergo avalanche multiplication.

When operating a chamber with a low drift field, little charge is collected because many ion pairs recombine before collection can occur. Increasing the drift field slightly enables the chamber to operate as an ionization counter where all of the charge deposited in the chamber is collected at the anodes and little or no electron multiplication occurs.

At higher fields electrons are accelerated in the region close to the anode wires such that they acquire enough kinetic energy to cause further ionization which gives rise to avalanche multiplication. For standard MWPCs and drift chambers this is achieved simply by increasing the drift field whereas for MSGCs, gain is produced primarily by the field produced between the anode and cathode strips with the drift field making a smaller contibution. The mean number of electrons collected by the anode from an avalanche initiated by a single electron is called the Multiplication Factor or gas gain. The number of electrons collected is directly proportional to the number of electrons produced in the drift space by ionizing particles and this is therefore called the proportional mode of operation.

As the field is increased still further the effect of ionization due to ultraviolet photons produced by the de-excitation of atoms excited during collisions in the avalanche region becomes important and the number of electrons collected ceases to be proportional to the number of electrons produced in the chamber by ionization.

At even higher fields, the chamber begins to operate in Geiger mode. The UV photons radiate throughout the chamber creating photoelectrons throughout the gas volume. The number of electrons collected is no longer a measure of the initial ionization and in multi-cell chambers, position sensitivity is lost.

2.4 Considerations affecting choice of gas

Two important considerations when selecting the gas to put in a proportional gas chamber are:

- The number of primary ion pairs produced per unit length. This is especially important in detectors with a thin gas gap.
- The maximum gas gain that can be achieved without losing proportionality or causing breakdown (of the gas).

Although avalanche multiplication can be achieved with all gases, the properties of some gases make them more suitable for certain applications than others.

The noble gases are invariably used in gaseous detectors because of the low electric field that is required to produce avalanche multiplication and because noble gases may only lose energy by radiation (ie: the emission of a photon or electron).

However this property of noble gases also gives rise to certain problems. During the avalanche process, atoms of noble gases are excited as well as ionized and may only return to the ground state by radiation of a photon. The minimum energy of such a photon (a few eV) is large enough to ionize the metal in the cathode via the photoelectric effect, producing an electron which will cause a spurious avalanche.

The positive ions drift to the cathode and neutralize, extracting an electron from the surface of the metal when they arrive. The excess energy is emitted as a photon or by extraction of another electron from the cathode which may again cause an avalanche. Both of these processes may cause a gaseous chamber to discharge continuously.

The solution to this problem is to add a quantity of a polyatomic gas such as methane or isobutane known as a quencher. Such gases are very efficient low energy photon absorbers and dissipate energy either by elastic collision or by dissociation into simple radicals. These gases thus absorb low energy photons and prevent secondary emission.

However, aging problems may arise depending upon the quencher used. Radicals from dissociated quencher may recombine into a polymer which may be deposited on the cathodes

forming a thin insulating layer. Positive ions migrating to the cathode will penetrate this layer only very slowly leading to a build up of positive charge on the cathode. The positive potential produced may become large enough to extract electrons from the cathode causing a continuous discharge.

It is therefore important to choose a quenching gas which causes minimum aging - especially in the case of MSGCs whose thin cathode strips ($\sim$ 100 μ wide) are likely to be susceptible to this problem. Dimethyl ether (DME) has been used with MSGC's because it is self quenching and has good aging properties. Tests involving the use of DME with drift chambers have shown very little accumulation of polymer deposits on the electrodes [19, 20].

2.5 Properties of Substrates

2.5.1 Substrate Charging

When an electric field is applied between anodes and cathodes of a MSGC equipped with a high resistivity substrate, it has been found from simulation software [9] that some of the field lines pass through the surface of the substrate between the anodes and cathodes. When electrons produced by a particle passing through the chamber enter the high field region close to an anode strip, an avalanche is initiated. The electrons from the avalanche are collected by the anode but some of the positive ions, instead of drifting to the cathode, follow the field lines to the substrate. The mobility of ions in an insulator is limited so the ions essentially become 'stuck' to the surface of the substrate and thus, after a short period of operation, positive charges begin to build up on the surface of the substrate which decreases the effective field in the avalanche region and hence the gain of the chamber. Such behaviour has been demonstrated experimentally in the laboratory [11] and in test beams [21].

One possible solution is to adjust the potential on the backplane electrode in order to repel the ions from the substrate. However this solution is only effective for very thin

substrates, the backplane potential having relatively little effect on the field lines when the thickness of the substrate becomes much greater than the anode/cathode spacing.

Insulating glasses in which the main charge carriers are positive ions and semi-conducting glasses which feature electronic conduction have been studied in attempts to solve the problem of substrate-induced gain instability in MSGCs under high fluxes of ionizing particles. A conducting substrate permits positive charge to leak away before it can build up on the surface. Two possible methods of giving a substrate conducting properties are to use a semi-conducting glass with relatively low bulk electronic resisitivity, or to use a substrate with modified surface resisitivity. The surface resistivity may be reduced by the deposition of a thin semi-conducting layer onto the surface of a resistive substrate or by implantation of positive ions.

Experimental tests in the laboratory using X-rays [13, 22] have shown that, while MSGCs equipped with semi-conducting substrates exhibited stable gain over time, those equipped with insulating substrates performed poorly by comparison. In addition, substrates whose surface resistivity has been modified by the implantation of positive ions also displayed poor performance characteristics. The poor performance of ion-implanted substrates is caused by migration of the ions to one electrode, causing an increase in resistivity as the substrate becomes depleted of charge carriers. MSGCs using substrates with semi-conducting surface layers have been shown to produce stable gain [22].

2.5.2 Comparative Performances of Different Substrate Types

Using a semi-conducting substrate can eliminate the gain instability of an MSGC in high fluxes of ionizing particles. However for low rate operation, the gain of an MSGC equipped with a semiconducting substrate is less than that of an MSGC equipped with an insulating substrate. The reason for this is that the use of a semiconducting substrate leads to an effective broadening of the electrodes, reducing the density of field lines and hence the gain of the chamber.

2.6 Considerations Affecting Operating Voltages

An MSGC has three different electrode potentials to consider, each one having a specific effect on the operation of the chamber. The considerations affecting the choice of each electrode potential are described below:

- **Anode Potential** The anode potential is usually set to 0V in order to eliminate the need for decoupling when reading out from the chamber.

- **Drift Potential** The principle consideration affecting the drift potential is that it must be high enough for the electrons created in the gas gap to drift to the avalanche region before significant recombination occurs. The drift field may also contribute to the gain of the chamber.

  Setting a high drift potential will increase the proportion of positive ions that travel to the drift electrode relative to the strip cathodes [9] which may affect the performance of the chamber at high rate.

- **Cathode Potential** Of the three electrode potentials, that on the cathode is most important in determining the gas amplifcation of the chamber. A small cathode potential will produce little or no gain along with poor resolution. Setting the cathode potential too high will result in discharges which can damage the electrode structure of the chamber [23] and produce noise together with poor spatial and energy resolution.

- **Backplane Potential** The principle reason for including the backplane was to reduce charging up of highly resistive substrates (see section 2.5.1) by repelling ions from the surface of the substrate. This technique is only effective when the thickness of the substrate is of the same order as the anode-cathode spacing. MSGCs using semiconducting substrates can be operated without a backplane [24].

2.7 Summary

We have presented here some of the ideas behind the operation of MSGCs. The MSGC uses the principle of gas multiplication in an electric field and has been developed from the MWPC and potentially offers enhanced spatial resolution combined with high rate capability. Much research has already been done to study many aspects of MSGC design, especially concerning the choice of suitable substrates.

The following chapter describes the construction and operation of a simple MSGC test chamber in the lab and presents results which serve to illustrate some of the basic operational properties described above.

Chapter 3

Measurements of MSGC Gas Gain and Energy Resolution

The neutron irradiation studies outlined briefly in Chapter 1 and described in detail in Chapter 4 required us to prepare test chambers for operation in a high neutron flux at ISIS. We intended to operate the chambers using two gas mixtures, argon/isobutane and argon/CO_2, in order to investigate the background induced in MSGCs by neutron interactions with gas mixtures containing hydrogenous and non-hydrogenous components. The properties of MSGCs using these gas mixtures were therefore investigated before irradiation.

To this end a test chamber was constructed and measurements of its gas gain and energy resolution were carried out. The chamber was equipped with both insulating (Tempax) and semi-conducting (S8900) substrates and results from these two configurations are compared.

3.1 Design of MSGC Test Chamber

In these preliminary studies we investigated the properties of MSGCs equipped with Tempax and S8900 glass substrates. Tempax is an insulating glass with bulk resistivity of

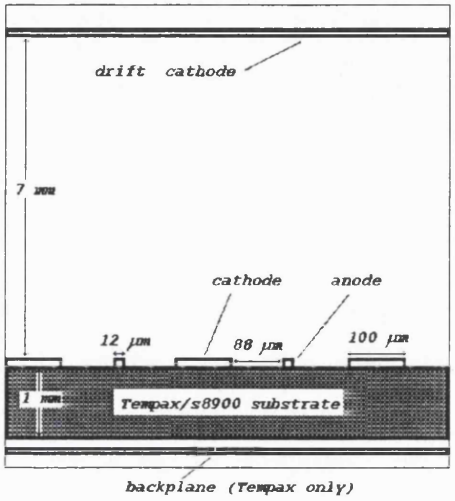

Figure 3.1: Internal geometry of MSGC test chamber.

approximately $10^{14}\Omega$cm whereas S8900 is a semiconducting glass with bulk resistivity of approximately $10^{11}\Omega$cm used in order to reduce the build up of positive charge on the surface of the substrate described in the previous chapter.

The two substrates were identical in layout. Each tile comprised five groups of 20 anode and 21 cathode strips ganged together, of which, only one group of strips was read out at any particular time. The strips were ganged together in order to collect as much of the charge deposited in the drift space as possible. Having only 1 operational strip for example, would have resulted in only the charge deposited in the drift space over that particular strip being collected, thus producing a very poor energy resolution.

The MSGC tiles had the following geometry:

- Anode width 12 μm
- Cathode width 100 μm
- Anode pitch 288 μm

The strips were made of aluminium and were 0.3 μm thick. The drift cathode comprised a sheet of aluminised Mylar, stretched over a frame of laminated epoxy resin and positioned to give a drift gap of 7 mm. This gap was kept constant for both the Tempax and S8900 measurements.

The backplane electrode was made by depositing a 25 μm square of copper onto a sheet of laminated epoxy and placed in rough contact with the substrate. The S8900 chamber was operated without a backplane [24].

Electrical contact to the anode and cathode strips was made by means of flexible phosphor-bronze strips attached to small laminated epoxy boards. The whole structure was enclosed in an aluminium die-cast box with electrical connections to the electrodes being made via SHV terminals sealed in the underside of the casing.

3.2 Test Apparatus

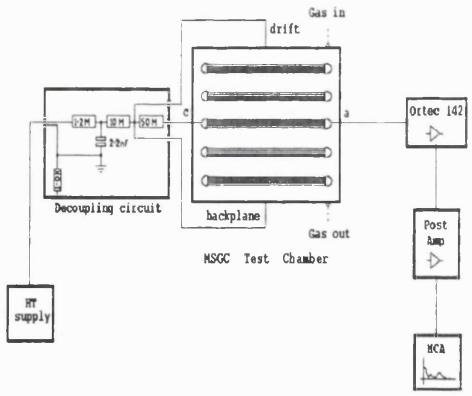

Figure 3.2: Apparatus used to test MSGC equipped with Tempax substrate

Figures 3.2 and 3.3 show the equipment used for testing the Tempax and S8900 glass substrates respectively.

During the tests with the Tempax substrate, the drift cathode, cathode strips and backplane were connected together due to a shortage of suitable power supplies. When the S8900 tiles became available, suitable supplies were obtained permitting the application of different voltages to the drift cathode and cathode strips.

Gas was passed continously through the test chamber using a standard gas rack, allowing us to mix the argon and quencher in varying proportions. The flow rate was maintained at 12 litres hr^{-1} in a gas volume of 4.8 litres.

To make measurements of the energy resolution and the effective gain, the MSGC was irradiated using a 50 μCi Fe^{55} source which emits 5.89 keV X rays . These X-rays produce a distinctive double peak when used to irradiate an argon filled gas chamber.

An Ortec 142pc preamplifier was used having a rise time of 40 ns and a fall time of 96 μs. The Ortec 142pc was also equipped with a test input with capacitance of 1.0pF, allowing a small test signal to be applied in order to calibrate the system and enable us to make gas gain measurements. The test pulse voltage was set by using an oscilloscope calibrated with a standard cell.

The post amplifier was an Ortec 570 [25] having variable gain settings and shaping times. For these tests, the shaping time was set to 2.0 μs and the gain set at 50.

Fe^{55} spectra were acquired from the chamber using an Ortec 916a multichannel analyser [26] which could be configured to acquire data in 512, 1024 or 2048 channels. A data collection time of 10 minutes was used in order to reduce statistical errors to an acceptable level.

3.3 Gas Gain, Energy Resolution and Count Rates.

The effective gain of the chamber is obtained by dividing the number of electrons collected by the anodes by the number of electrons created in the drift space. For a 5.89 keV photon in

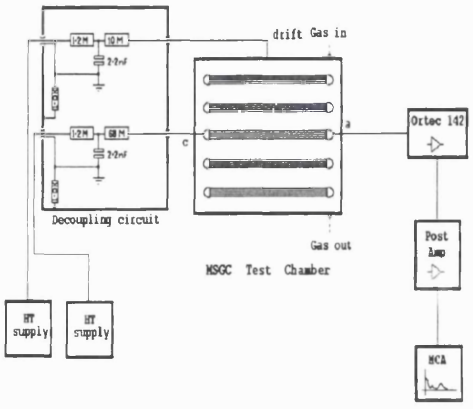

Figure 3.3: Apparatus used to test MSGC equipped with S8900 substrate

argon-isobutane, the number of electrons created is ΔE/W = 233. To measure the effective gain of the MSGC, we located the position of the 5.89 keV Fe^{55} on the MCA scale and compared it with the position of a peak produced by applying a test pulse to the amplifier. The gas gain of the chamber is then given by

$$A = \frac{E_{Fe}}{E_{tp}} \frac{CV_{tp}W}{\Delta Ee} \tag{3.1}$$

Where V_{tp} is the test pulse voltage, e is the charge of the electron and C is the test capacitance of the amplifier. W is the average energy required to create an ion pair for a given gas mix, ΔE is the energy deposited in the chamber and E_{tp} and E_{Fe} are the positions on the MCA energy scale of the peaks produced by a test pulse and the 5.89 keV peak of the Fe^{55} respectively.

The energy resolution of the chamber under these conditions is given by

$$\frac{\sigma(E)}{E} = \frac{FWHM_{Fe}}{2.36M_{Fe}} \tag{3.2}$$

where $FWHM_{Fe}$ is the FWHM of the (Gaussian) 5.89 keV peak.

The observed count rate was obtained by summation over the Fe^{55} energy spectrum recorded on the MCA and dividing the total by the run time.

3.3.1 Voltage Corrections

For a Tempax substrate, $R_{surf} \gg R_b$ where R_{surf} is the surface resistance between one complete set of 20 anode and 21 cathode strips, and R_b is the cathode ballast resistance (see Fig 3.3). However, for the semi-conducting S8900 glass the ballast resistance resistance approaches 2 % of R_{surf} causing a voltage drop across the ballast resistor. The current drawn by the configuration in figure 3.3 is 0.29 nA so the true cathode voltage for S8900 is given by

$$V_c = V_{ht}(1 - 0.29 \times 10^{-9} R_b) = 0.98 V_{ht} \tag{3.3}$$

3.3.2 Sources of Error

- The gas gain varies according to the reduced electric field E/p where p is the atmospheric pressure. Using data obtained from the Meteorological office, the atmospheric pressure was not found to vary from 1000 bar by more than $\pm$ 20 mbar during the measurement period, producing an error in E/P of not more than 2 %.

- The ratio of the two components in the gas mixture was obtained by reading from the flowmeter scales of the gas rack. The accuracy of this ratio is estimated to be 2.5 % including calibration errors.

- The Fe^{55} source produced a count rate of about 9 Hz in the chamber. A run time of 10 minutes therefore produced statistical fluctuations with a standard deviation of 1.5 %.

3.4 Results

3.4.1 Variation of Drift Potential

The chamber was equipped with a S8900 substrate and a gas mix of 75 % argon and 25 $\%CO_2$. The cathode voltage was maintained at 700 V and the drift potential was varied. In each case the gain and count rate were calculated. Fig. 3.4 and Fig. 3.5 show the gas gain and count rate of the chamber as a function of drift voltage. It will be noticed that if the drift voltage is reduced below 500 V, a large reduction in count rate is observed but with no corresponding drop in gain. This effect is caused by recombination of ion pairs in the drift region, resulting in very few electrons reaching the avalanche region.

3.4.2 Differences between Tempax and S8900 Substrates

Fig. 3.6 shows the variation of the relative gain with time after the application of electrode potentials to MSGCs fitted with the two types of substrate[1].

The gain of the MSGC with the Tempax substrate can be seen to decrease quite rapidly during the 45 minutes after volts are first applied to the chamber, with the S8900 substrate, the gain remains stable. This behaviour is caused by positive ions building up on the surface of the substrate as described in the previous chapter and is in agreement with results obtained elsewhere [11]. The gain decreases until the rate of arrival of ions on the surface of the substrate is equal to the rate at which they are conducted away through the substrate. The rate at which the ions are transported away depends on the conductivity of the substrate and so substrates with higher resistivity are more susceptible to this effect.

[1]The data for S8900 was taken using a qVt multichannel analyser and CRO due to the unavailability of the MCA at that time.

3.4.3 Mixtures using Isobutane and Carbon dioxide as a Quenching gas

Fig. 3.7 shows the result of varying the chamber voltages for the MSGC when equipped with a Tempax substrate. The drift, backplane and cathode strips were all held at the same voltage. Using various mixtures of argon and isobutane, gains in excess of 1000 were achieved without the chamber discharging.

When gas mixes using carbon dioxide were tested using the MSGC equipped with an S8900 plate, potentially damaging discharges were observed for all mixtures as the gas gain approached 1000 showing that carbon dioxide is a less efficient quencher. These results are displayed in Fig. 3.8.

3.4.4 Energy Resolution

Results obtained from measuring the energy resolution (see eq. 3.2) of the MSGC when equipped with a S8900 tile are displayed in Fig. 3.9. We see that the energy resolution obtained with argon/isobutane mixes is 8 % whereas that obtained with argon/CO_2 mixes is 9 %. This difference is possibly due to carbon dioxide being less effective in suppressing the propagation of ultraviolet photons created in the avalanche process.

3.4.5 Summary

The results obtained from this development of techniques can be summarized as follows.

- Our test MSGCs require a drift voltage of at least 600 V to prevent ion pairs recombining in the drift space.
- MSGCs using insulating Tempax glass substrates require a certain amount of time to stabilize when first exposed to radiation, dependant on the rate of production of ion pairs in the avalanche region. A loss of gain of $\sim$ 30 % is observed. MSGCs using semiconducting S8900 substrates do not appear to suffer from this problem.

- With this configuration, Ar/CO_2 mixtures can only achieve sustainable gains of $\sim$ 1000 without discharging, confirming that it as a less efficient quenching gas. Gains approaching 2000 can be attained using a mixture of 75 % argon/ 25 % isobutane.
- Using this set up, the energy resolution for 5.89 keV photons is 8 % for 75 % argon/ 25 % isobutane. The energy resolution is 9 % if carbon dioxide mixtures are used.

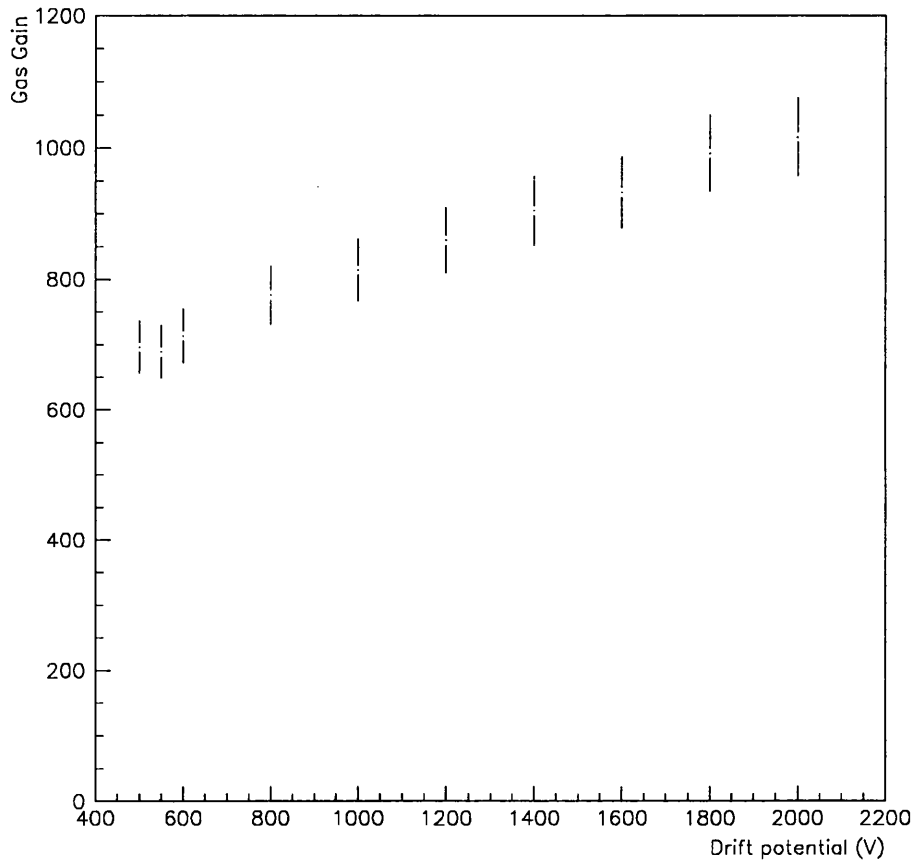

Figure 3.4: Gas gain as a function of drift voltage.

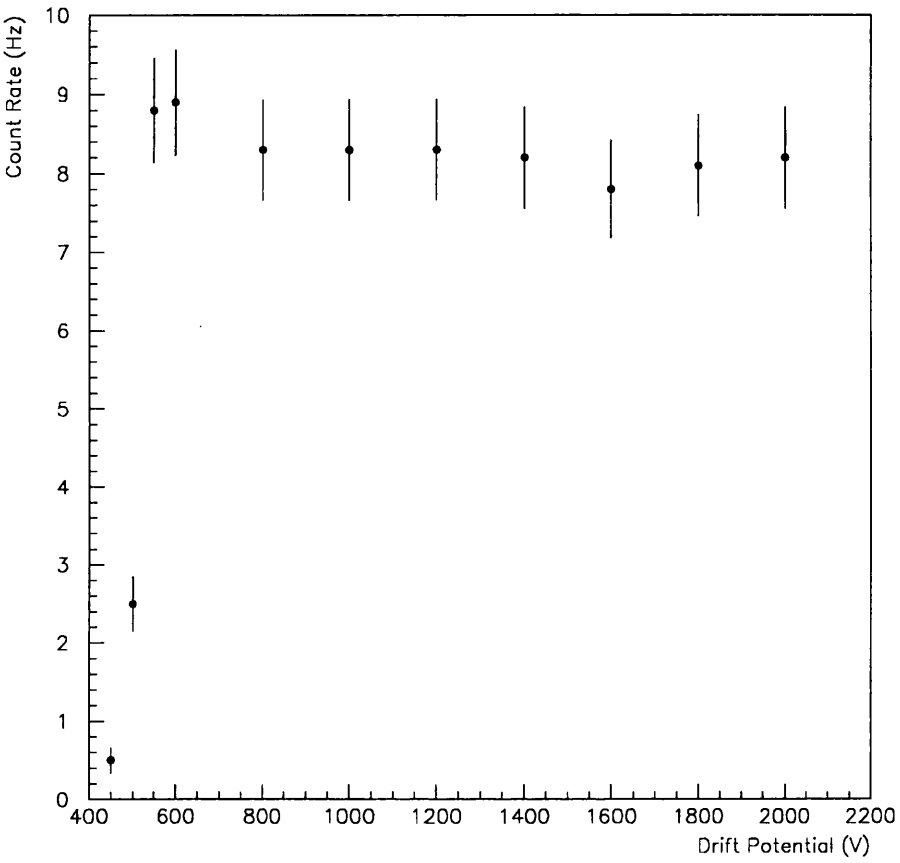

Figure 3.5: Count rate as a function of drift voltage.

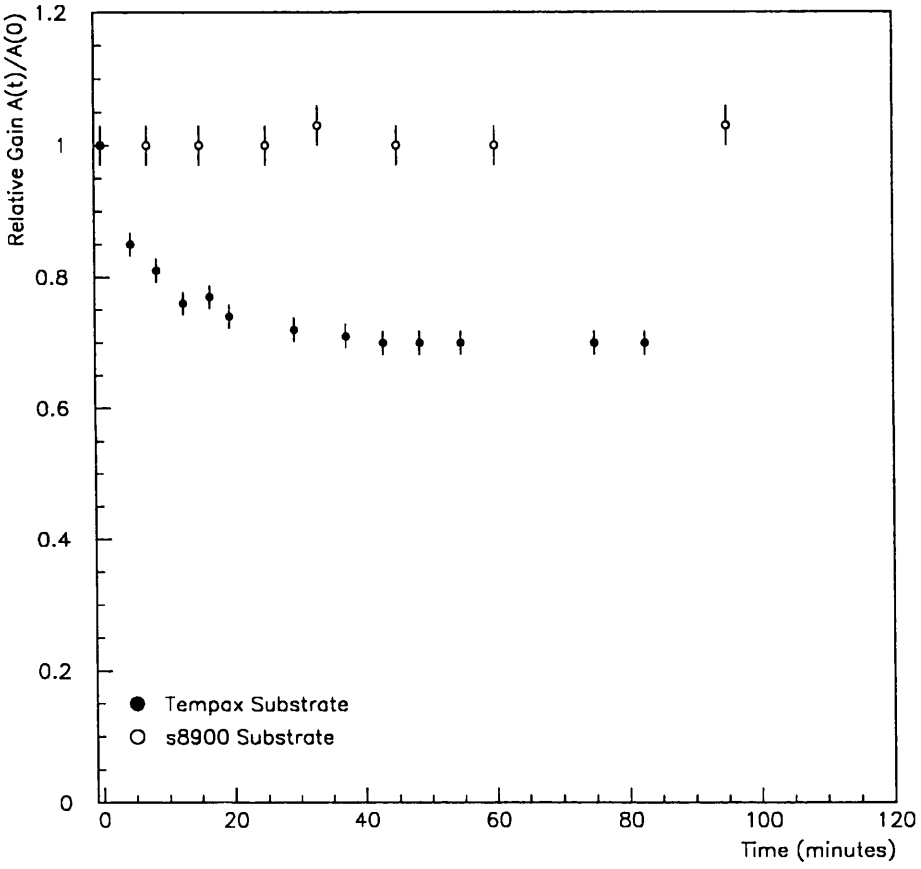

Figure 3.6: Gain variation with time after application of voltage to electrodes.

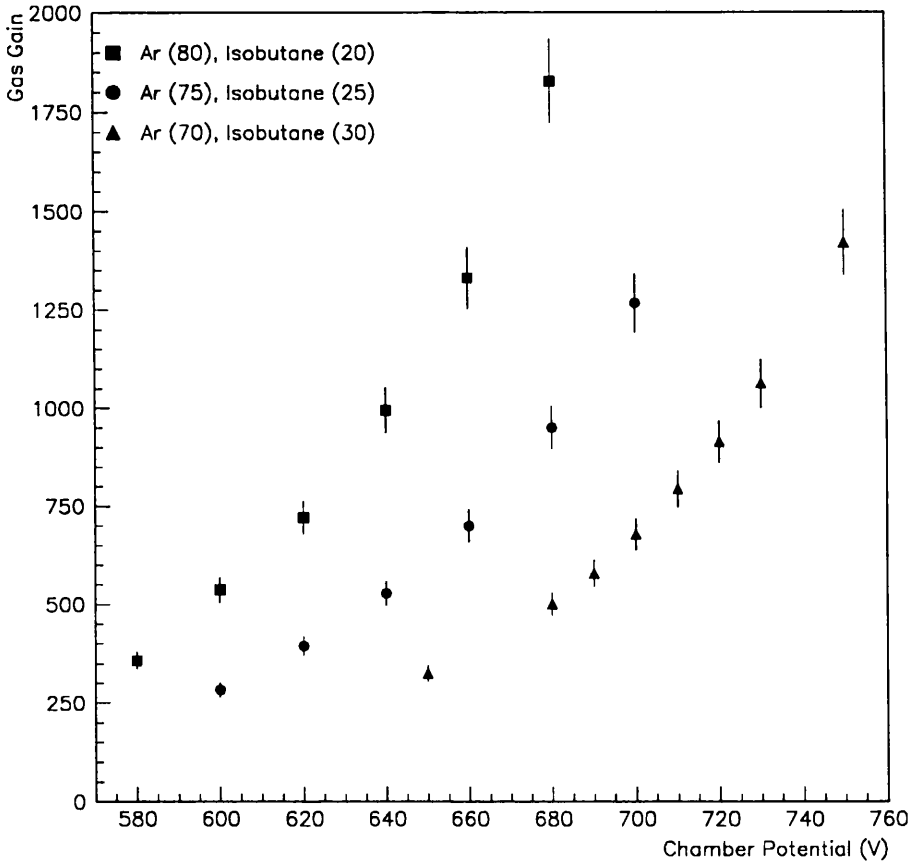

Figure 3.7: Gas gain as a function of chamber voltage ($V_c = V_d = V_b$) for a MSGC equipped with a Tempax tile.

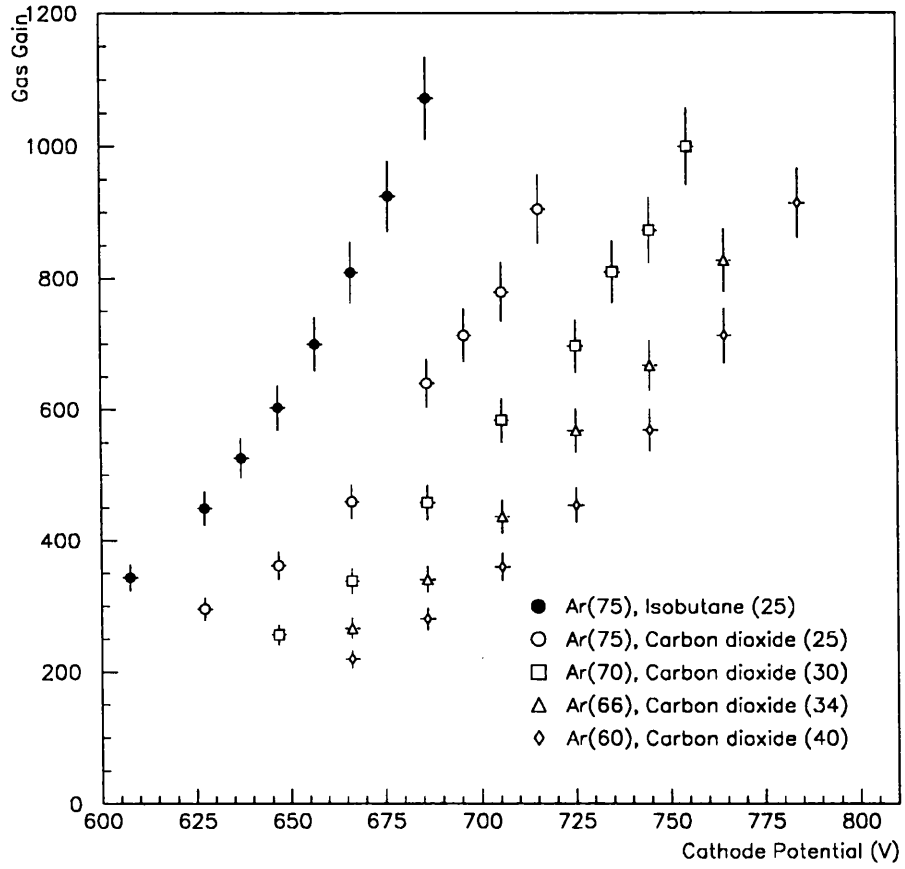

Figure 3.8: Gas gain as a function of cathode voltage for a MSGC equipped with a S8900 tile (V_d = 1000V, no backplane).

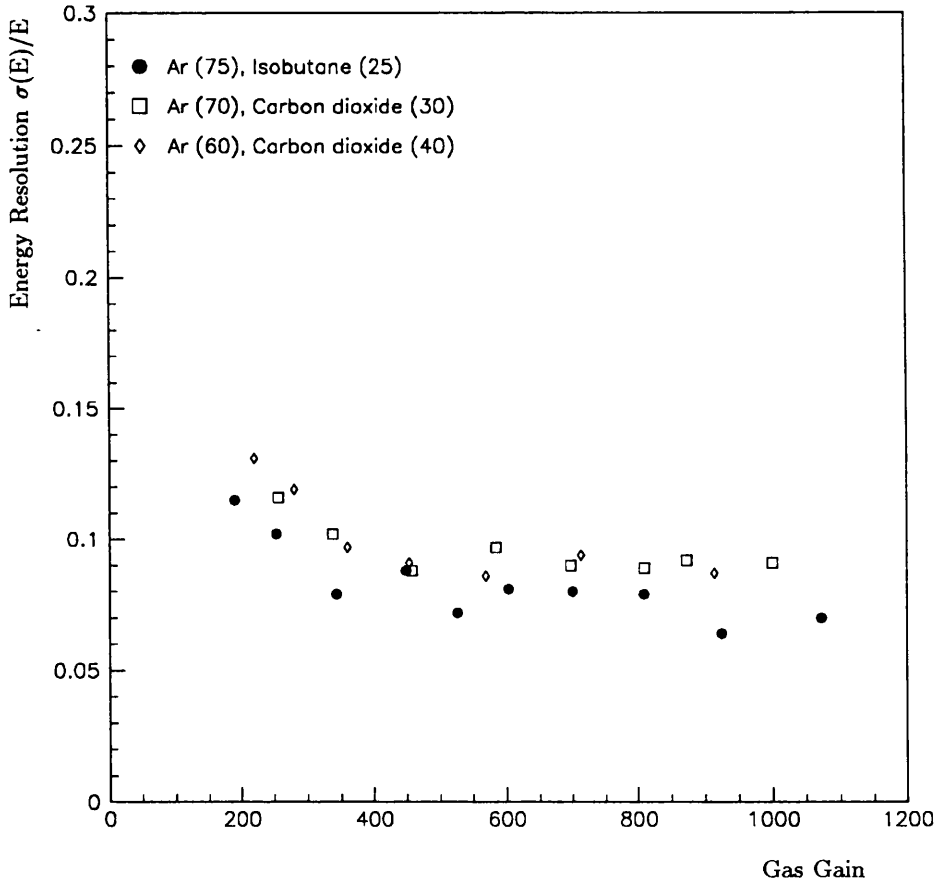

Figure 3.9: Energy resolution as a function of gas gain for a MSGC equipped with a S8900 tile.

Chapter 4

Experimental MSGC Neutron Irradiation Studies

4.1 Introduction

A number of studies and simulations have predicted that the ATLAS inner detector will carry a high flux of low energy albedo neutrons emitted from the calorimeter structure. Any particle detector in the inner cavity is required to operate for 10 years under such conditions.

Depending on the type of detector, these neutrons can give rise to two types of problem:-

1. **Radiation damage** to the structure of the detector, resulting in a permanent degradation of its performance.

2. **An increased count rate** due to detection of radiation produced as a result of prompt or non-prompt neutron interactions in the chamber.

Our aim was to study how the second of these problems could affect an MSGC, and in particular whether the signals so produced will cause a significant increase in the occupancy of the detector or in its charge loading or place extra requirements on the electronics.

4.2 Simulations of Neutron Fluxes in ATLAS

The neutron flux in the inner detector arises from hadron showers in the calorimeter. A high energy hadron interacts inelastically with atomic nuclei in the calorimeter, resulting in the creation of secondary hadrons. Secondary hadrons with sufficient energy then produce further tertiary hadrons in a similar manner. As particle multiplication continues, a hadron shower develops inside the calorimeter, its extent being dependent on the energy of the incident hadron. The shower also includes an electromagnetic component formed by the decay of π^0 mesons to photons which then produce electrons and positrons via pair production etc. Multiplication continues until the particles in the shower have insufficient energy to produce additional particles, after which point energy is lost only via Coulomb and scattering processes.

Although low energy charged particles will ultimately be stopped in the calorimeter due to energy loss via Coulomb interactions, energy loss by neutrons in the calorimeter will effectively cease once the energy of the neutrons falls below the level required for inelastic scattering to take place. These neutrons will permeate the calorimeter structure and ultimately leak out. It is those escaping from the inner surface towards the inner detector which give rise to the problems being investigated here.

The inner cavity of ATLAS will contain a high flux of such neutrons, and simulations using different approximations to its geometry have been undertaken to predict the energy spectra to be expected [27, 28]. The most detailed simulation [29, 30] calculated neutron energies using the proposed ATLAS detector layout with various amounts of polyethylene moderator covering the region between the calorimeter and the inner detectors. The neutron energy spectra obtained from these simulations are shown in Fig. 4.1 and are, in the approximations of their author, assumed to be uniform throughout the inner detector. The main features of these predictions are that apart from a peak in the thermal region ($E_n \approx \frac{1}{40}$ eV), the energy spectrum remains fairly flat up to about 0.1 MeV, beyond which the spectrum peaks at 1.0 MeV and 100 MeV before dropping sharply away.

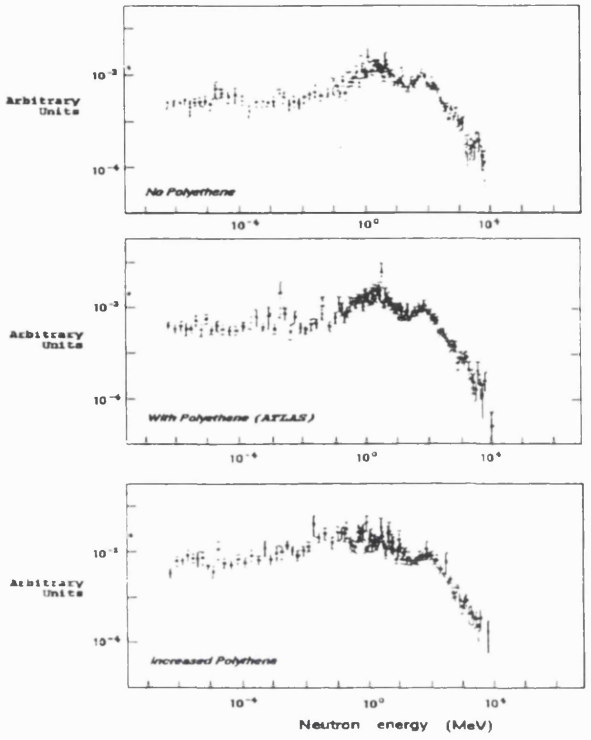

Figure 4.1: Neutron energy spectrum simulation calculated from proposed ATLAS detector geometry.[29]

The only experimental confirmation that could be found for this simulation data is provided by an experiment [31] which investigated the flux of low energy neutrons leaking from a stack of iron plates irradiated by 200 GeV hadrons. The spectrum of neutrons escaping from this structure was inferred by allowing the neutrons to interact with a set of metal foils whose induced activity was subsequently measured. By identifying these decay products and measuring their energy, the energy spectrum of the neutrons was determined. The experiment showed that about 75 % of the neutron flux had energies < 5 MeV with the remainder having energies between 5 and a few 100 MeV. This is not inconsistent with

the spectra in Fig. 4.1 given the very rough approximation to LHC geometry.

4.3 Possible Effects of Neutron Background

The total neutron fluxes in the inner cavity calculated using the proposed ATLAS geometry [30] are summarised in Table 4.1. We first compare these fluxes to the predicted charged particle flux given by [2]

$$N \approx \frac{2 \times 10^9}{r^2} cm^{-2} sec^{-1} \tag{4.1}$$

where r is the radial distance in cm from the beam axis. The region occupied by MSGCs is from r = 40 cm to r = 100 cm, so between 1.25 $\times 10^6$ and 0.2 $\times 10^6 cm^{-2} sec^{-1}$ charged particles are expected to be incident on a given MSGC. At a radius of 40 cm, it will be seen that the neutron and charged particle fluxes are expected to be approximately equal.

distance (Z) (metres)	Total neutrons ($cm^{-2} sec^{-1}$)	Neutrons (E > 100 keV) ($cm^{-2} sec^{-1}$)
1	2 $\times 10^6$	4 $\times 10^5$
2	2 $\times 10^6$	1 $\times 10^6$
3	4 $\times 10^6$	1 $\times 10^6$

Table 4.1: Neutron fluxes at ATLAS as a function of longitudinal distance (Z) from the beam crossing at a radial distance 40 cm from the beam pipe [30].

This neutron flux in ATLAS may affect MSGC operation in the following ways:

1. There will be an increase in counting rate, in occupancy, and charge loading, due to neutrons:

- Neutrons cannot cause direct ionization of the MSGC chamber gas and thus be detected directly. This suggests that the neutron flux in the inner cavity has to be considerably greater than the charged particle flux before there can be a significant increase in counting rate due to neutron interactions in MSGCs. In ATLAS, the neutron flux and the charged particle flux are approximately equal as shown above therefore, neutrons might not be expected to cause a substantial increase in the counting rate compared to that due to charged particles. This requires confirmation as it depends upon the cross-section of the various neutron-induced processes.
- The neutron-induced occupancy might however be very much higher than that given by a simple consideration of the neutron-induced counting rate. Neutrons will transfer energy to protons and light nuclei via scattering interactions. These light nuclei, being highly ionising, may deposit large amounts of energy in the drift space of MSGCs thus producing large pulses. Such large pulses may result in a significant increase in amplifier dead time and hence an increase in the apparent occupancy caused by the amplifier output signal failing to decay within a single LHC bunch crossing.
- Such large pulses will also produce an increased current drawn by the detector which can in turn lead to some of the operational problems listed below.

2. The following operational problems may also arise as a result of the high neutron flux expected at ATLAS:
   - Damage to the MSGC in the form of erosion of the anode and cathode strips as a result of large energy depositions as described above.
   - Aging of the chamber caused by neutrons interacting with certain components such as the electrodes or the substrate thus degrading the performance over a long period of time. In addition, impurities in the gas may give rise to deposits on the electrode structure.

- Damage to the pre-amps resulting from large pulses unless precautions are taken.

These latter operational problems are not covered by this work.

4.4 The Experimental Program at ISIS

On the basis of the discussion in the previous two sections, it was decided to investigate the extent to which the first of the above two considerations will affect the use of MSGCs in ATLAS.

The performance of MSGCs in a high neutron flux was studied experimentally using the neutron spallation facility at ISIS which produces neutrons with an energy spectrum not too dissimilar to that predicted for ATLAS. ISIS is a 0.8 GeV proton synchrotron situated at the Rutherford Appleton Laboratory where a beam of protons is directed onto the collector, a target comprising a layer of copper and a layer of graphite [33]. The protons interact with the copper producing the neutrons and any residual protons are stopped by the graphite.

Throughout these studies ISIS was operating at 'base rate', i.e. with a circulating proton current of 5 μA and an injection rate of 1 Hz, in preference to its normal operating conditions where the proton current is 160 μA and the injection rate is 50 Hz. The reason for this was that the flux of neutrons at the higher proton current (2.6×10^8 n $cm^{-2}sec^{-1}$) would produce radiation damage to the pre-amplifiers which were located with the MSGCs in the collector area, and make the MSGCs too radioactive to handle conveniently.

Fig. 4.2 shows neutron energy spectra measured at three distances from the collector [32]. It will be noted that the fast neutron flux varies more strongly with distance from the collector than does the thermal component of the spectrum. We only had restricted access to the collector area which constrained the chambers to be positioned approximately 475 cm from the collector, particularly if fluxes of a similar magnitude to those expected in ATLAS were required. Although no measured neutron spectra exist at this distance, the approximate flux may be calculated [32] and is described in more detail in Chapter 5. Comparing the fluxes calculated for these base rate conditions with those expected in ATLAS we find that:

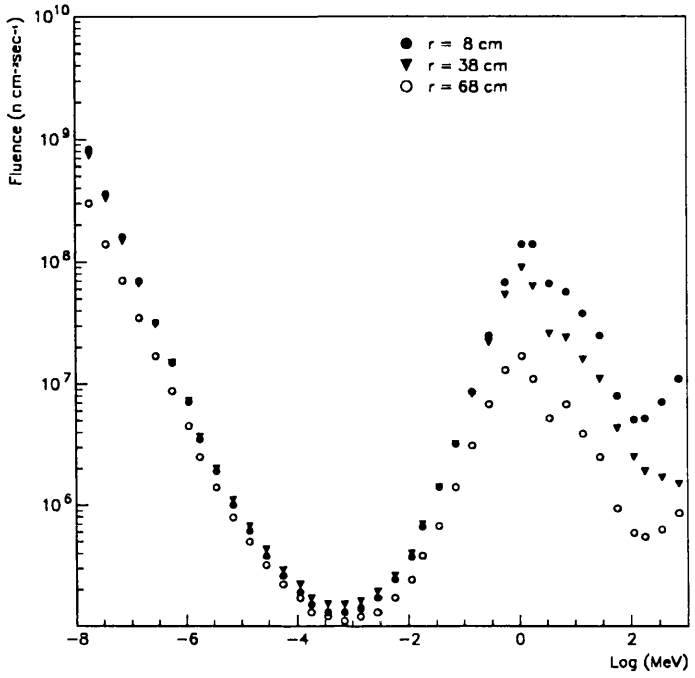

Figure 4.2: ISIS neutron energy spectrum measured at various distances r from the collector [32].

- $ISIS_{slow}(E < 10keV) \approx 2ATLAS_{slow}$
- $ISIS_{fast}(E > 10keV) \approx 0.1ATLAS_{fast}$

Therefore, based on Ferrari's predictions [30], the flux of fast neutrons at our chambers placed at 475 cm from the collector and with ISIS operating at base rate, will be an order of magnitude less at ISIS than at ATLAS, but will be very similar for slow neutrons.

The angular distribution of neutrons from the ISIS collector differs from that expected in ATLAS. Neutrons in ATLAS will be essentially isotropic in direction, whereas those at ISIS will be coming from the collector and thus are not isotropic.

The main objective of this program of tests was to expose an operating MSGC to the ISIS neutron beam and to measure the spectrum of energy deposited in the chamber and the counting rate, and hence infer the impact of albedo neutrons upon the operation of MSGCs within ATLAS.

4.4.1 Test Apparatus

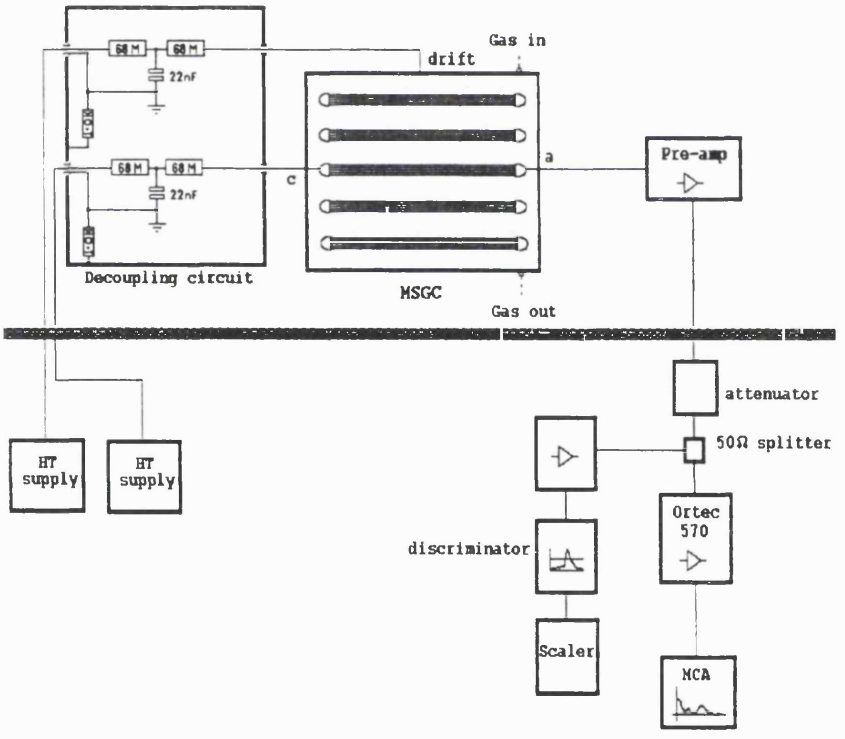

Figure 4.3: Test chamber set-up used for ISIS irradiation tests

The experimental system used for these tests consisted of two MSGC test chambers similar in construction to the one described in Chapter 3. These were mounted one above the other (see Fig. 4.4), with the entrance windows facing so that a 50 μCi Fe^{55} gamma source could be positioned so that it irradiated both chambers simultaneously. The position of the Fe^{55} source was controlled remotely and could be retracted when measurements of the neutron induced spectra were being made.

Each chamber was connected to a read-out chain (see Fig. 4.3) consisting of a pre-amplifier, variable attenuator, post-amplifier and a multi-channel analyser (MCA). A discriminator and scaler provided online count rate monitoring.

Inside the synchrotron hall itself, signals from the MSGCs were input to a pre-amplifier located very close to the MSGC, before being sent down 100m of coaxial cable to the rest of the read-out chain located outside the synchrotron ring. A variable attenuator enabled us to increase the range of energies which could be recorded on the MCA, necessitated by the wide range of pulse heights expected from neutron interactions.

The signal was divided in two using a 50 Ω splitter, one half of the signal being amplified by the post-amp before being input to the MCA. The other half of the signal was amplified and discriminated before being scaled.

The voltage was supplied to each chamber using two HT supplies, one for the drift plane and one for the strip cathodes.

The pre-amp used for the neutron tests was an OPAL pre-amplifier [34] modified to have a 65 ns rise time and a 20 μs fall time. All of the instruments and cables were carefully shielded in order to screen out the extremely high level of interference generated by the synchrotron's rf system with a common ground in order to eliminate earth loops. This was a serious technical difficulty at the start of the experiment.

The post amplifier used was an Ortec 570 which was set with a shaping time of 2 μs, and the MCA was an Ortec 916a.

4.4.2 Chamber Construction

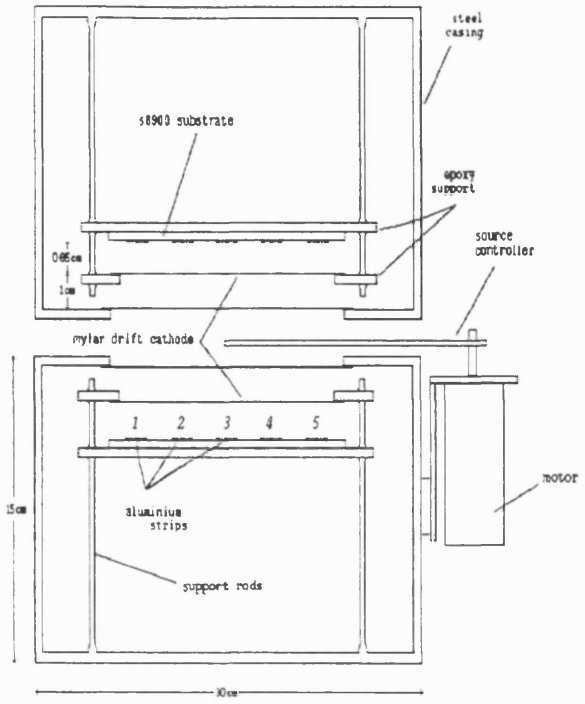

Figure 4.4: Internal layout of test chambers used in ISIS irradiation tests

Apart from the containing box, the MSGC geometry used in these tests was identical to that of the chamber described in chapter 3 except for the drift distance, which was set to 8.5mm in order to increase the rate of neutron interactions in the gas[1].

The aluminium anode and cathode strips were 0.3 μm thick and deposited in a rectilinear pattern on a 1.7 mm thick s8900 glass substrate. The tile was designed so that the strips were ganged together in five groups of 20 thus increasing the signal to noise ratio by up to a factor of 20 (depending on the number of strips hit in any given event). This was very

[1] and to prevent arcing between the plate contacts and the drift cathode due to a design problem in the chambers

important in the high noise environment at ISIS.

A sectional view of the internal structure of the test chamber is shown in Fig. 4.4. The MSGC and its supports were enclosed in a 3 mm thick stainless steel box of dimensions 300 × 270 × 150 mm. This had a 75 × 75 mm window adjacent to the drift cathode which was covered by a sheet of aluminized Mylar in order to allow low energy photons from the Fe^{55} source into the chamber and with which to calibrate the energy scale of the MCA.

Two alternatives to stainless steel were considered for manufacturing the case, namely aluminium and some form of plastic such as polycarbonate. Aluminium was discounted because Al^{27}, the most abundant naturally occuring isotope, would absorb thermal neutrons creating Al^{28} which rapidly decays emitting β particles. These would produce a high count rate in the chamber from a source which was not really a part of the study. Any form of hydrogenous material such as polycarbonate was also rejected on the grounds that elastic collisions between neutrons and hydrogen nuclei could result in large energy depositions in the chamber. Stainless steel was therefore chosen because it was less prone to become active in the short term. However, care had to be exercised when using steel chambers in order that the chambers did not receive too large a radiation dose or otherwise they would have become active for a significant period of time due to the creation of isotopes such as Cr^{51} and Fe^{59} which have half lives of the order of a month.

However, these isotopes have only a relatively small production cross-sections and both Cr^{50} and Fe^{58} which absorb thermal neutrons to form Cr^{51} and Fe^{59} respectively are only present in relatively small quantities. Thus they will make only a small contribution to the neutron-induced signal if the chamber was only irradiated for short periods of time.

The MSGC drift cathode was mounted 1 cm from the entrance window. 5.89 keV photons have a high cross section for absorption in argon[2] therefore any larger space between the Mylar window and the detection area would have resulted in too great an attenuation of photons from the source although it would have resulted in a smaller counting rate due to radioactive nuclei produced in the case.

[2]The mean free path of a 5.89 keV photon in argon is approximately 3 mm.

4.5 ISIS Test Procedure on Active MSGCs

The tests at ISIS were carried out using two different gas mixtures in an effort to identify the origin of various components of the neutron induced signal. The MSGC was initially filled with a mixture of 75 % argon / 25 % isobutane, a gas mix whose properties are well documented and understood. This was later changed to a mixture of 60 % argon, 40 % CO_2 (i.e. no hydrogen) for comparison with the argon/isobutane mixture.

These gas mixes determined the maximum sustainable operating voltages of the chamber. Although it was originally intended to run both chambers with an effective gain of approximately 1000, argon/CO_2 mixtures began to give discharges at gains of above 800 because carbon dioxide is a less efficient quencher than isobutane. As a result of the laboratory studies reported in the previous chapters and the above consideration, the chambers were operated with the following drift and cathode voltages:

- Argon/isobutane: - V_c = 735 V, V_d = 950 V, giving an effective gain of 1100.
- Argon/CO_2: - V_c = 820 V, V_d = 950 V, giving an effective gain of 750.

The test chambers were first set up inside the synchrotron hall with the accelerator and rf systems switched off in order to obtain an Fe^{55} spectrum for energy scale calibration of the MCA. It also provided an opportunity to study the energies deposited in the chamber by background radiation emitted from materials in the synchrotron hall made active by earlier operation of ISIS.

It was intended to carry out argon/isobutane and argon/CO_2 runs simultaneously using the two stacked chambers in order to ensure identical beam conditions for accurate comparison between the two gas mixtures. However technical difficulties prevented this from taking place so the program was executed sequentially using only a single chamber situated 475 cm from the collector, according to the following program:-

- ISIS rf off, injector off, (i.e. radioactive background from collector area only).

- ISIS rf on, injector on, but beam stops in place, thus preventing protons entering the ring (i.e. radioactive background from collector area, plus rf noise, plus a certain (unknown) amount of neutron flux).

The following program was then conducted with ISIS operating under normal base rate conditions, i.e. beam stops removed.

- Gas mixture 75 % argon, 25 % isobutane.
  Chamber oriented so that neutrons passed through it in a direction parallel to the strips.

- Gas mixture 75 % argon, 25 % isobutane.
  Chamber oriented so that neutrons passed through it in a direction perpendicular to the strips.

- Gas mixture 60 % argon, 40 % CO_2.
  Chamber oriented so that neutrons passed through it in a direction perpendicular to the strips.

- Gas mixture 50 % argon, 50 % CO_2.
  Chamber oriented so that neutrons passed through it in a direction parallel to the strips. (The proportion of CO_2 in the mixture was increased because we had begun to experience problems with discharges at 40 % CO_2 .)

4.6 Analysis Technique

4.6.1 Verification of Gain Stability

We had to be sure that the MSGC gain remained constant as a function of rate because if not, measurement of the energy deposited in the drift space would be made extremely difficult as Fe^{55} spectra were not directly visible under data taking conditions and hence not available as a calibration of any shifted energy scale.

Gain stability was demonstrated by showing that the position of the 5.89 keV peak produced by the Fe^{55} source remained static on the MCA scale as the level of radiation increased. Fig. 4.6 shows the position of the Fe^{55} peak with four different levels of radiation incident on the chamber:

- With ISIS turned off, spectra were obtained with the MSGCs in a low background environment away from collector area with recorded count rate $\approx$ counts sec^{-1}, and in a higher background environment in the collector area with recorded count rate $\approx$ 210 counts sec^{-1}. Fig. 4.6 show that the gain of the chamber is the same for these two conditions.

- ISIS was turned on with an injection frequency of 1 Hz (base rate) and protons were dumped on the beam stops 100 metres away from the chamber (instead of entering the ring). This produced a counting rate of about 830 counts sec^{-1}. The spectrum obtained by irradiation of the MSGC under these conditions (Fig. 4.6: "1 Hz radiation bursts") shows a negligible movement in the position of the Fe^{55} peak at this count rate.

- When the beam stops were removed so that protons were allowed into the synchrotron ring, the Fe^{55} peak was no longer directly visible on the MCA due to the comparatively large neutron induced signal and so any loss of gain could no longer be directly observed. However two spectra were obtained, one with the source in place and one with the source removed. By subtracting the latter from the former, the Fe^{55} could just be seen (Fig. 4.6: "1 Hz neutrons + Fe^{55} - 1 Hz neutrons") although the argon escape peak was obscured. Again, little movement was observed in the position of the Fe^{55} peak. The count rate recorded at this level of radiation was approximately 2700 counts sec^{-1} which was similar to the rate used for aquisition of the remainder of the data.

These observations agree with results obtained in test beams at CERN and in the lab

[11] in showing that the gain of MSGCs equipped with s8900 substrates is rate invariant up to an incident charged particle flux of 5 $\times 10^6$ particles $cm^{-2}sec^{-1}$.

4.6.2 Dead Time Corrections and Normalization

1. **Dead Time Correction.**

   The Ortec 916a MCA has a dead time of 25 μs per count and, at the counting rates we observed ($\approx$ 3 kHz), begins to have a significant effect. The MCA keeps a record of the dead time as a percentage of the sample time and reached a maximum value of 10.7 % for unattenuated argon/isobutane operation. The dead time of the post-amplifier was measured to be about 2 μsecs and we estimated the pre-amplifier dead time to be about 10 μsecs, i.e. half the fall time. Therefore the longest dead time per count in the chain is the 25 μsecs of the MCA, making its dead time the effective dead time for the entire chain. The total integrated number of counts is then divided by the live time rather than the sample time in order to find the count rate corrected for dead time.

2. **Normalization of Count Rates**

   The raw ISIS data is the energy spectrum and total number of counts produced in the active part of the detector during the run. Providing the data are correctly normalized, we can use it to estimate the neutron induced count rate in ATLAS (see section 4.8). We normalize the data by dividing our counts by the active area of the MSGC and by the corrected running time to obtain a count rate in counts $sec^{-1}cm^{-2}$. The active detection area comprises 20 detection cells each of width 300 μm which are ganged together; the strip length is 5 cm and hence the total active area of a drift cell is 3 cm^2.

4.7 Results and Discussion

4.7.1 General Pulse Characteristics

Pulses produced by the MSGC at different radiation levels were studied on a digital oscilloscope. Examples of some of these output pulses from the preamp are shown in Fig. 4.5. It can be seen from these pictures that the amplitude of pulses observed with the ISIS beam on (Fig. 4.5b) is over an order of magnitude greater than those obtained from the Fe^{55} source in a low background environment (Fig. 4.5a). They are also much larger than the background pulses observed directly after irradiation (Fig. 4.5c). We attribute these large pulses to the products of prompt neutron interactions for three reasons:

1. Such pulses were not seen when no rf. was running and hence are not due to background in the collector area.

2. Such pulses were not seen when the rf. was running but with no protons injected into the synchrotron ring. Therefore they are not due to rf induced noise.

3. Protons that have escaped the collector and entered the drift space could in principle produce large pulses such as these. However, such protons would need an energy of more than 100 MeV to penetrate the stainless steel casing of the chamber. The collector is specifically designed to absorb protons (see section 4.4) and we consider it most unlikely that there is a sufficient flux of 100 MeV protons to produce the rate of large pulses we observed.

4.7.2 Results from MCA Spectra.

- **Background Radiation from Collector Area**

  Fig. 4.7 shows the background energy spectrum obtained in the collector area with the ISIS beam off before exposing the MSGC to neutrons using the argon/isobutane mixture.

The background radiation we detected is presumably the result of the decay of long lived radioactive isotopes formed by the capture of neutrons by various materials in the synchrotron hall. The multiplicity of elements in material surrounding the MSGC test chambers means that α, $\beta^{\mp}$, and γ particles are all likely to be produced. Of these, only photons in the energy range where Compton scattering or pair production is the dominant process, have sufficent range or penetration to reach the drift space of the MSGC where they then cause ionization in the gas and thus produce a signal. From Fig. 4.7, we see that the maximum energy deposited in the drift space by such background radiation is about 90 keV.

- **Activation of Chamber Materials.**

  Fig. 4.8 shows spectra obtained immediately after irradiation for both gas mixtures, with the MSGC still in the collector area. Comparing the argon/isobutane data with that before irradiation (Fig. 4.7), an increased count rate is observed. A part of this increase is due to materials within the chamber such as iron and argon, both of which may form radioactive isotopes when they absorb thermal neutrons, resulting in the emission of $\beta^{\mp}$ particles and photons. The remainder will be due to photons produced by newly activated materials outside the MSGC enclosure, the composition of which we have no knowledge. It is measured separately as is the previous item in this list but, of necessity, a long time after neutron irradiation. (Monte-Carlo calculations, described later, will however show that all such photon contributions are small.)

- **Neutron Induced Interactions in the MSGC.**

  Fig. 4.9 shows spectra obtained using the argon-isobutane mix with the chamber oriented so that the neutrons are incident both parallel and perpendicular to the strips. The energy deposition spectra show a peak at low energies which rapidly falls away in the range 0 to 0.1 MeV. As the energy deposited increases above 0.1 MeV the count rate decreases more gradually. Energy depositions of 0.6 MeV generated pulses which were sufficient to saturate the pre-amplifier and studies of larger energy depositions

were impossible as, for operational reasons, there was no access to the collector area and hence no possibility to insert variable attenuators before the pre-amp during a run. These saturating pulses could be observed on the oscilloscope and produced a spike at a fixed position at the end of the MCA spectrum. The position of the spike was seen to move when we changed the attenuation between pre-amp and post-amp, showing that it was not caused by saturation of the post-amplifier, but of the pre-amplifier.

In the high energy region, a slightly higher count rate is observed (Fig. 4.9) when the neutrons are incident parallel compared to when they are incident perpendicular to the strips. This effect is presumably due to the directional nature of the elastic scattering processes on light nuclei shown later to be the cause of the larger energy depositions in the chamber. When a neutron scatters from hydrogen or other light nuclei in the gas, a charged ion is produced travelling in the forward direction with respect to the original neutron's direction of travel, which implies that ions scattered by neutrons of parallel incidence travel a greater distance in the detector cell than ions scattered by neutrons of perpendicular incidence. For example, a 0.4 MeV proton has enough energy to escape the active region if travelling in a direction perpendicular to the strips, and will thus deposit less energy than if its direction is parallel to the strips.

The isobutane data (Fig. 4.9) is to be compared with that obtained using carbon dioxide as quencher (Fig. 4.10). However it must be noted that the rate of energy loss (dE/dX) in argon/CO_2 is less than that for argon/isobutane, hence even if the neutron-induced spectra were the same, they would appear to be shifted due to the difference in dE/dX. It will be noticed that, at high energies, the count rate in argon/CO_2 is about one third of that in argon/isobutane. This points to interactions in hydrogenous material as being largely responsible for the rate of high energy depositions. However, the existence of energy depositions above 100 keV (i.e. above the maximum produced by background) in argon/CO_2 suggests that interactions with hydrogen in the gas are not the only source of large neutron-induced deposits. Neutrons must also be interacting with light nuclei such as carbon or oxygen in the gas or hydrogen in the

Mylar drift cathode.

The argon/CO_2 data also shows a large difference in counting rates obtained for neutrons of parallel and perpendicular incidence (Fig. 4.10) in the energy range between 5 and 100 keV. We are not aware of any physical explanation for this, but it may well be caused by the inadequate quenching we experienced while running with argon/CO_2, which tended to result in discharges while running with the beam on.

4.7.3 Analysis of Count Rates

In order to obtain a more accurate value for the neutron-induced counting rate at ISIS, we need where possible, to subtract the count rate produced by the background radiation in the synchrotron hall.

- **Subtraction of Background Radiation.**

  A study of spectra taken before neutron irradiation showed that there was a significant amount of background radiation in the collector area due to the presence of long-lived radioactive isotopes in the synchrotron hall. (Fig. 4.7).

  The background recorded for argon/CO_2 operation was measured after the chamber had been irradiated and thus become active during argon/isobutane data taking. Therefore the background count for argon/CO_2 operation contains a component due to active materials in the chamber itself as well as in the synchrotron hall.

  The background spectra and count rates in Table 4.2 therefore include some induced chamber activity. The background spectra were subtracted from the neutron irradiation spectra obtained with the ISIS beam switched on in order to remove the signal produced by long-lived radioactive isotopes in the hall.

- **Energy Thresholds.**

  For argon/isobutane data, we set a threshold of 2 keV on the MCA discriminator to exclude the signal produced by the various sources of noise (electronics, rf). This

threshold was set during the experimental run at ISIS while the beam was off but with the rf system on. The discriminator level was increased until the rf noise was excluded.

The maximum sustainable gain obtained using CO_2 mixtures was considerably less than that achieved using the isobutane mixture and so for CO_2 operation, a given discriminator threshold would correspond to a higher energy than for the isobutane mixture because of the lower gain obtainable with CO_2. The rf noise dominated the counting rate when using Ar/CO_2 at energies below 5 keV, and we therefore compare count rates in the two mixtures above this threshold.

We also defined a threshold at 100 keV in order to study the count rate induced by neutrons in the chamber alone. Referring to Fig. 4.7, we see that the largest energy deposition in the chamber produced by background radiation is approximately 90 keV. Hence the spectrum for energy depositions below 90 keV will contain a component due to radiation originating outside the chamber. Therefore we study the count rate for energy depositions above 100 keV to exclude events produced by radiation originating outside the MSGC.

We thus present three counting rates for neutron-induced interactions in the chamber:

1. An integrated number of counts for energy depositions greater than 2 keV (argon/isobutane operation only) which excludes rf noise.
2. An integrated number of counts for energy depositions greater than 5 keV to permit comparison of argon/isobutane and argon/CO_2 rates which excludes rf noise for both mixtures.
3. An integrated number of counts for energy depositions greater than 100 keV which excludes the effect of background radiation in the experimental area.

The count rates for all MSGC operating conditions are summarized using these energy boundaries in Table 4.2.

Using eqs 5.33 and 5.7.1 we calculate the approximate neutron flux at 475cm from the collector to be

- 8.1 $\times 10^6$ $cm^{-2}sec^{-1}$ for neutrons with energy $E_n < 10$ keV
- 9.6 $\times 10^4$ $cm^{-2}sec^{-1}$ for neutrons with energy $E_n > 10$ keV.

This gives a total neutron flux of 8.2 $\times 10^6$ $cm^{-2}sec^{-1}$ summed over all energies, and the count rates in Table 4.2 are those obtained when operating the chambers in this flux.

Conditions	Counting Rate (counts $cm^{-2}sec^{-1}$)		
	E > 2 keV	E > 5 keV	E > 100 keV
Neutrons || to strips, Ar/i-C_4H_{10}.	930	470	7.3
Neutrons $\perp$ to strips, Ar/i-C_4H_{10}.	960	500	7.1
Background[3], Ar/i-C_4H_{10}.	63	31	0.0
Background[4], Ar/i-C_4H_{10}	290	130	0.0
Neutrons || to strips, Ar 50 %/CO_2 50 %.	-	410	3.0
Neutrons $\perp$ to strips, Ar 60 %/CO_2 40 %.	-	66	2.3
Background[3], Ar 50 % /CO_2 50 %.	-	22	0.0
Background[4], Ar 60 %/CO_2 40 %.	-	36	0.03

Table 4.2: Counting rates measured under different MSGC operating conditions (see text).

[3] Before neutron irradiation

[4] After neutron irradiation

4.8 A First Estimation of the Neutron-Induced Count Rate of MSGCs in ATLAS

In ATLAS, the predicted charged particle flux varies from 7 $\times 10^5$ cm^{-2} sec^{-1} at a radius of 40 cm from the beam, to 1.2 $\times 10^5$ cm^{-2} sec^{-1} at a radius of 100 cm [1]. We wish to make a rough estimate of the additional counting rate in MSGCs due to counts induced by the neutron background.

This may be done very crudely by taking the highest count rates recorded in Table 4.2 and multiplying by $\frac{flux_{ATLAS}}{flux_{ISIS}}$ taking the total neutron flux at ISIS to be 8.2 $\times 10^6$ cm^{-2} sec^{-1}, and the largest calculated neutron background flux at ATLAS to be 4 $\times 10^6$ $cm^{-2}sec^{-1}$ [30]. These estimated counting rates are given in Table 4.3 along with the counting rates measured at ISIS for comparison. We also express these figures as a fraction of the charged particle count rate:

Gas mixture	Neutron Count Rate Hz cm^{-2}		Neutron rate as % of Charged Particle Rate in ATLAS	
	ISIS (measured)	ATLAS (estimated)	r = 40 cm	r = 100 cm
Ar/i-C_4H_{10},(δE > 2.0 keV)	950	460	0.07 %	0.4 %
Ar/CO_2,(δE > 5.0 keV)	410	200	0.03 %	0.2 %

Table 4.3: Neutron induced counting rates measured at ISIS and corresponding count rates expected at ATLAS.

Although such small fractional increases in count rate of less than 1 % would be entirely acceptable, these crude values are unfortunately only an underestimate for the following reasons:

- Our MSGCs were read out with 20 strips ganged together whereas in ATLAS, MSGC

strips will be read out singly. The neutron induced count rate in MSGCs in ATLAS may thus be many times higher than our estimate because neutron induced particles may traverse several strips producing a signal on each one.

In order to investigate this problem experimentally we would have had to make measurements at ISIS with a MSGC equipped with single strip read-out, but this was precluded by the high noise levels in the ISIS collector area.

- Using data for the number of ion pairs produced by minimum ionizing particles in a gas [14] we calculate that a mip at normal incidence to the substrate would deposit 2.6 keV in our chamber when filled with 75 % argon/25 % isobutane. Due to the large rf signal, the minimum energy deposition measurable at ISIS was 2 keV (i.e. $\frac{4}{5}$ of a mip). At ATLAS, the discriminator threshold will be set at a lower level than this, say $\frac{1}{3}$ of a mip or less. In view of the very rapidly rising rate at lower energy depositions (see Fig. 4.9), the neutron induced counting rate will be much higher than the estimate in Table 4.3 due to low energy depositions which were unobservable at ISIS.

- MSGCs in ATLAS will be operating in a 2T magnetic field parallel to the drift field. The effect of this field will be to make low energy charged particles, such as those produced by neutron interactions, follow a helical path with the magnetic field as axis. The radius of these helices is comparable to a few MSGC strip widths and hence energy depositions by particles, particularly βs, will take place over many fewer strips at ATLAS than at ISIS. The effect will clearly be to "harden" the spectrum of energy deposited on a given strip, but in a way not easy to quantify.

- The neutron energy spectrum at ATLAS is rather different to that of ISIS; in particular the ratio of fast to thermal neutrons is much higher although the overall neutron flux in ATLAS and ISIS is approximately equal. Most of the counting rate at ISIS is likely to have been produced by thermal neutron interactions, implying that the energy deposition spectra and counting rates produced in ATLAS could be markedly different but in a way which is not easily calculable.

- The occupancy in MSGCs at a given count rate will be increased due to the finite decay time of each amplifier channel which can be several bunch crossings of the LHC. A large energy deposition on a given channel, such as have been observed at ISIS, may produce a significant dead time before the signal decays completely thus increasing the effective occupancy of the detector.

- In any case, MSGCs in ATLAS will have a different geometry from those used at ISIS and will be constructed from different materials and use a different gas filling.

All of these factors will result in different neutron induced counting rates and energy deposition spectra from those observed at ISIS.

4.9 Summary of Results

- A significant fraction of events deposited energies greater than 500 keV in the chamber when the neutron beam was switched on. This is many times more than that deposited by a m.i.p (2.6 keV). (Energy depositions of this magnitude will be shown in Chapter 5 to result from neutron scattering by light nuclei.)

- From observations of background radiation spectra obtained before and after neutron irradiation, we believe that a significant component of low energy depositions is due to photons and β particles. Such particles are emitted by materials activated by the absorption of thermal neutrons and Monte Carlo studies will later show that they can only result in energy depositions of below 100 keV in the drift space of the test chamber.

- Replacing the hydrogenous quencher (isobutane) with carbon dioxide produces a significant reduction in count rate implying that a large proportion of energy depositions are a result of neutron interactions with hydrogen in the gas. However, results obtained from argon/CO_2 operation suggest that large energy depositions may also be

produced as a result of neutron scattering on other light nuclei in the gas or in the Mylar drift cathode.

4.10 Conclusion

We crudely estimate an increase in the counting rate of MSGCs due to neutron induced energy depositions in ATLAS to be around 0.4 % of the charged particle flux. However this must be an underestimate for the reasons described above. The only way open to arrive at improved estimates of this increase is to build a Monte Carlo model. Such a model has to incorporate all of the physical processes by which neutrons can produce signals in MSGCs and to take into account the appropriate geometry and neutron spectrum of the ATLAS environment. Nevertheless, the above results from ISIS, although they do not lead directly to a good estimate of the increase in occupancy caused by neutrons, are of crucial importance to this work because:-

1. they give, as discussed above, a good indication of many of the physical processes responsible for neutron-induced counts in MSGCs.

2. they provide a valuable set of experimental results against which the MC model may be checked by running the model with the ISIS configuration (geometry, gas, beam, etc.) instead of the ATLAS configuration.

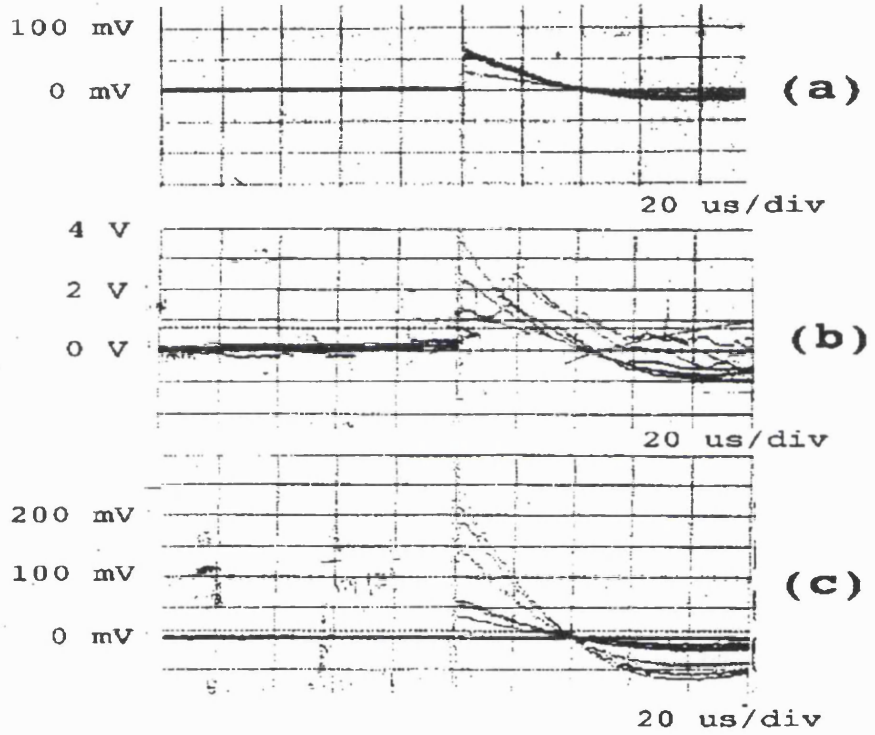

Figure 4.5: Oscilloscope traces showing

a) Fe^{55} pulses recorded before neutron irradiation.

b) Prompt neutron induced pulses observed during irradiation.

c) Pulses produced by active material after irradiation.

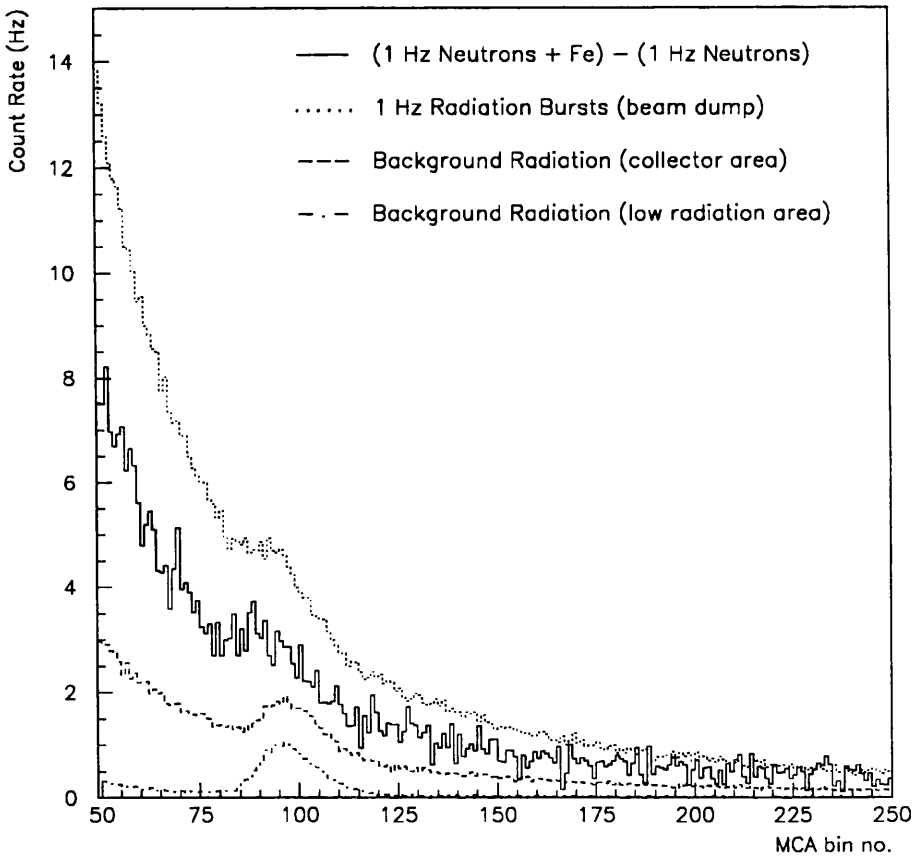

Figure 4.6: Fe^{55} spectra obtained in environments with different levels of radiation, demonstrating gain stability.

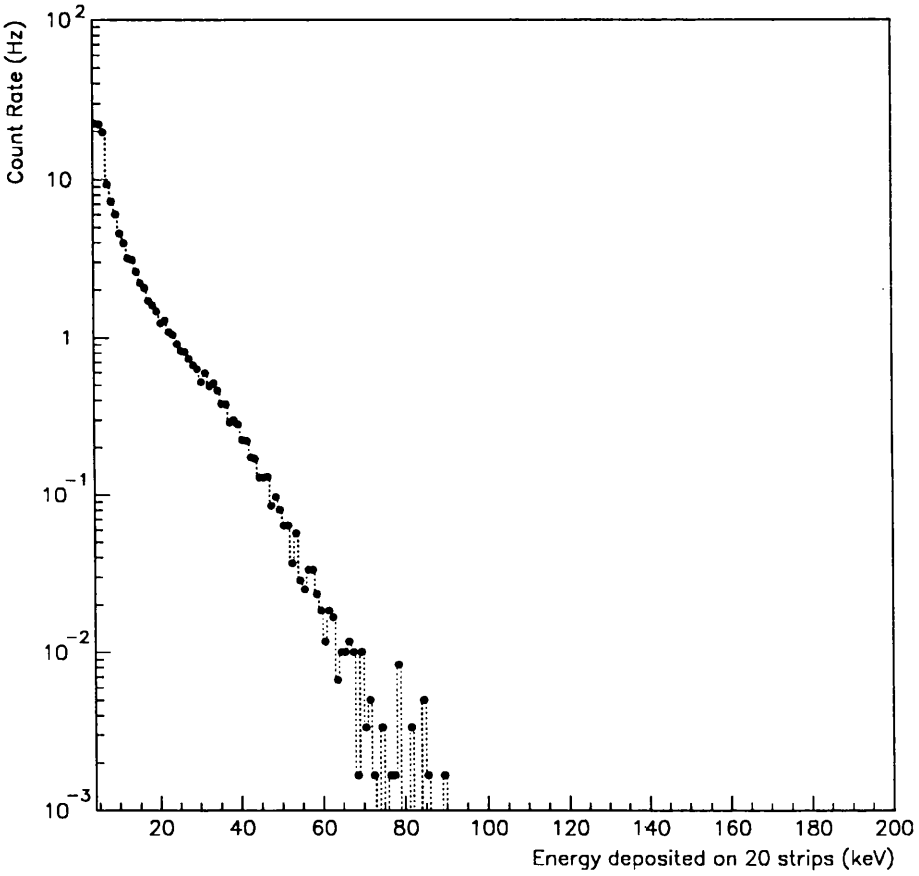

Figure 4.7: Energy spectra obtained from background radiation using MSGC filled with 75 % argon/25 % isobutane. ISIS beam off. (Before irradiation).

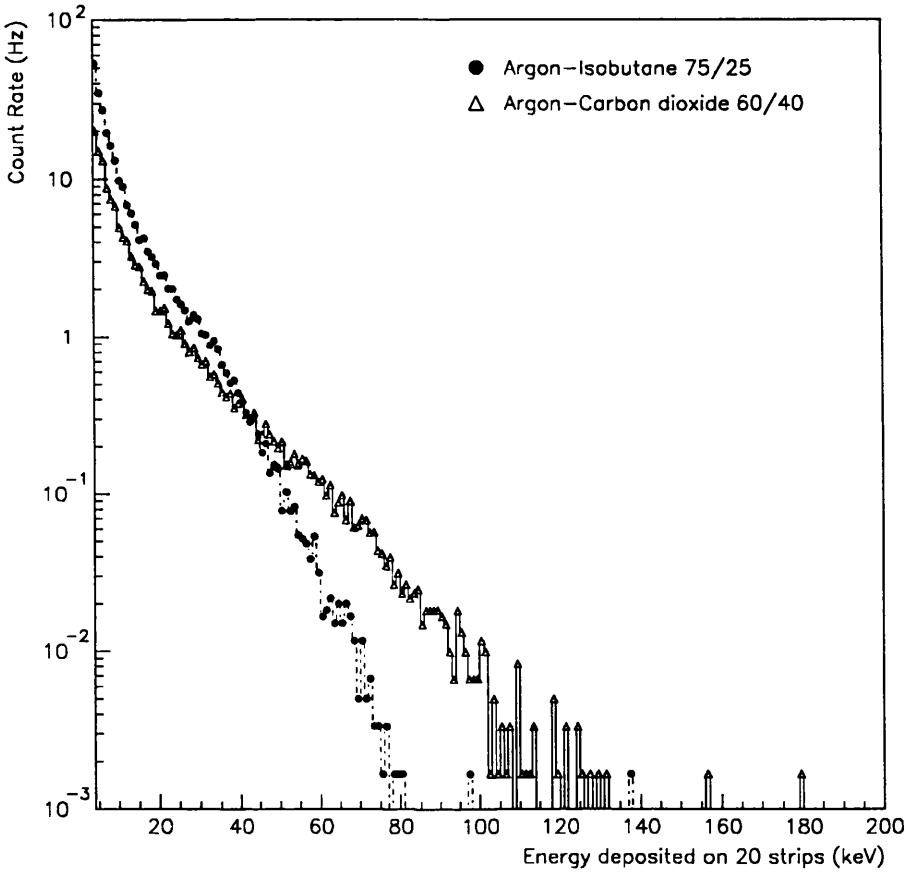

Figure 4.8: Energy spectrum obtained from MSGC immediately after neutron irradiation. ISIS beam off.

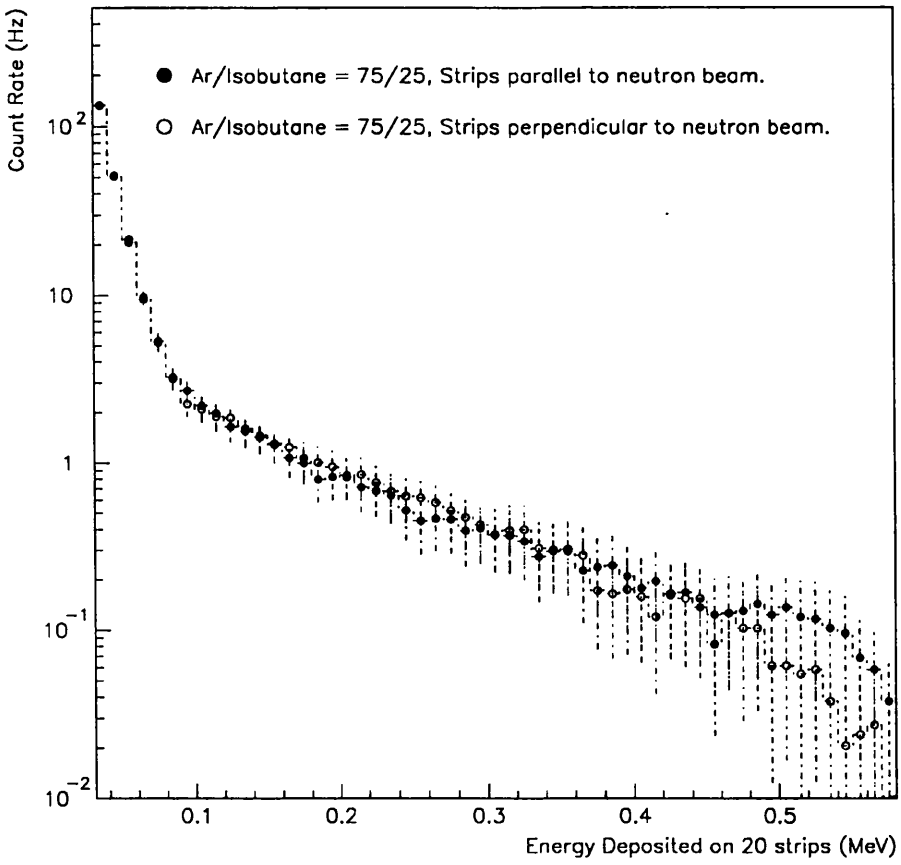

Figure 4.9: Energy spectrum obtained from Neutron irradiation of MSGC filled with 75 % argon/25 % isobutane. ISIS beam on, background (Fig. 4.7) subtracted.

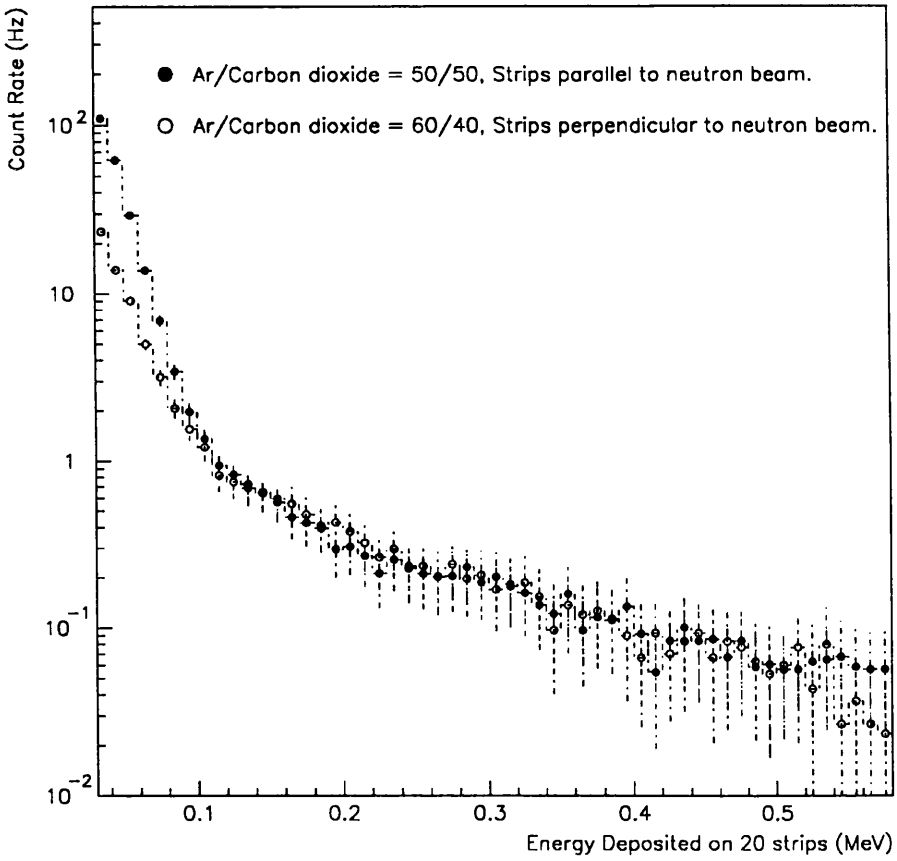

Figure 4.10: Energy spectrum obtained from Neutron irradiation of MSGC filled with argon/CO_2. ISIS beam on, background (Fig. 4.8) subtracted.

Chapter 5

A Monte Carlo Model of Neutron Interactions in MSGCs

This chapter describes a Monte Carlo simulation program which enables us to investigate hypotheses made in the previous chapter concerning the origin of the signals produced by MSGCs when operated in a high flux of low energy neutrons. If the model can reproduce the experimental results obtained at ISIS then we will have confidence that we have incorporated the appropriate physical processes and the simulation can then be exploited reliably to study neutron-induced effects at ATLAS as a function of materials used in chamber construction.

This was successfully done and is reported in this chapter, resulting in predictions for the occupancy and energy deposition spectra for single strip readout in the ATLAS configuration, and which were not accessible to direct measurement at ISIS.

5.1 Neutron Induced Processes

Neutrons cannot ionize directly but they can participate in interactions which result in the production of ionizing particles. To model the behaviour of MSGCs in a neutron flux, we must first identify the significant processes that can produce such ionizing particles.

Guided by the work reported in the previous chapter the following processes were considered likely to be responsible for a significant count rate, and we divide them into two categories:-

- **Prompt interactions** resulting in an almost immediate emission of ionizing particles into the chamber. These were:

  1. Elastic scattering of a fast neutron from a nucleus , (especially hydrogen) resulting in the production of a positive ion, X_Z^A :-

     $n + X_Z^A \Longrightarrow n + X_Z^A$.

  2. Neutron capture resulting in the prompt emission of a charged particle or photon (which may cause ionization of the gas via the photoelectric absorption, Compton scattering or pair production processes). The only process of this type which was modelled was :-

     $np \Longrightarrow d\gamma$

     which has a high cross section (inversely proportional to the velocity) at low energies.

- **Non-prompt interactions**. Neutrons may be absorbed forming radioactive isotopes which then decay emitting ionizing radiation. These processes include:

  1. Beta decay, resulting in the emission of an electron or positron.

     $n + X_Z^A \Longrightarrow X_Z^{A+1} \Longrightarrow X_{Z\pm1}^{A+1} + \beta^{\mp} + \nu$

  2. K shell electron capture $n + X_Z^A \Longrightarrow X_Z^{A+1} \Longrightarrow X_Z^{A+1} + \gamma$

     or isomeric transition $n + X_Z^A \Longrightarrow X_Z^{A+1} \Longrightarrow X_Z^{A+1} + \gamma$,

both of which may lead to the emission of photons which subsequently may cause photoelectric absorption, Compton scattering or pair production.

The following sections (5.2, 5.3) describe the above processes in greater detail.

5.2 Prompt Interactions

5.2.1 Elastic Scattering

This section describes the elastic scattering of neutrons from nuclei. The neutron collides with a nucleus as shown in Fig. 5.1 and is scattered leaving the nucleus in the ground state. The kinetic energy of the incident neutron is shared between the neutron and the recoiling nucleus.

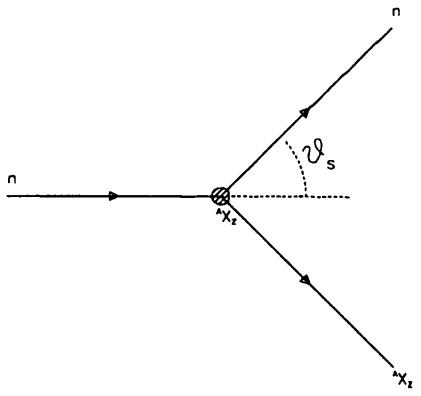

Figure 5.1: Neutron scattering from a nucleus in laboratory system.

At the neutron energies with which we are dealing, we may use simple, non-relativistic kinematics to describe this process. The energy of the scattered nucleus may be obtained

[35, 36] from the equation

$$E^{'}(E,\omega_s) = \frac{1}{(A+1)^2}[\omega_s\sqrt{E} \pm \sqrt{E(\omega_s^2+A^2-1)+A(A+1)Q}]^2 \quad (5.1)$$

where A = $\frac{M_{nucleus}}{m_n}$, $w_s = \cos\theta_s$ and Q is the excitation energy of a given state of the target nucleus. This equation however, describes the energy transfer for both elastic and inelastic scattering as a function of scattering angle.

In the case of elastic scattering, Q = 0, and eq. 5.1 reduces to

$$E^{'}(E,\omega_s) = \frac{E(\omega_s \pm \sqrt{\omega_s^2+A^2-1})^2}{(A+1)^2} \quad (5.2)$$

For neutron-proton scattering, because $m_p < m_n$, a valid solution is only obtained when the second term is positive [35] and eq. 5.2 becomes

$$E^{'}(E,\omega_s) = \frac{E(\omega_s + \sqrt{\omega_s^2-1.37\times10^{-3}})^2}{3.99} \quad (5.3)$$

Elastic scattering of fast neutrons is nearly isotropic in the centre of mass system and therefore the cosine of the scattering angle in the centre of mass system ω_{cm} is equally probable in the range $-1 < w_{cm} < 1$ and is related to ω_s by the equation

$$\omega_s = \frac{\gamma+\omega_{cm}}{\sqrt{1+2\omega_{cm}\gamma+\gamma^2}} \quad (5.4)$$

where $\gamma = \frac{1}{A}$ for elastic scattering. Both the energy and the direction of the scattered neutron and proton may thus be calculated relative to the initial direction of the neutron if ω_{cm} is known.

From these equations we see that the processes likely to produce the largest energy transfers and therefore the largest signals from the MSGC, are collisions with lighter nuclei. In the case of hydrogen for example, a head-on collision ($\theta_s = 0$) would result in all of the kinetic energy of the incident neutron being transferred to the recoiling nucleus. A similar collision with a carbon nucleus however, would result in the recoiling nucleus only taking 28 % of the energy of the incident neutron. Light elements such as hydrogen, carbon and oxygen are all present in materials that are contained either within the gas envelope of an

MSGC (isobutane, carbon dioxide, argon) or in close proximity to it, e.g. the Mylar drift cathode. These processes have a comparatively high cross section (a few barns) [37] and all or most of the energy transferred to the target nucleus will be deposited in a few cm of gas thus giving rise to large pulses.

No. of e^-	Count Rate Hz cm^{-2}			
lost by stripping	δE > 26 eV	δE > 1 keV	δE > 10 keV	δE > 100 keV
0	0.0	0.0	0.0	0.0
1	153.9	95.2	67.7	20.7
2	166.7	116.3	75.9	26.0
3	189.4	129.6	73.5	30.9
4	182.5	125.8	75.9	31.2
5	197.2	128.0	81.2	28.9
6	149.7	108.9	75.4	31.9

Table 5.1: Count rate as a function of the number of electrons stripped from a carbon nucleus during elastic scattering.

A problem that arises when considering scattering from light nuclei other than hydrogen is the need to know how many atomic electrons are lost (stripped) from the nucleus as a result of the scattering process. This varies according to the amount of energy transferred to the target nucleus which may lose any number from zero to its full complement of atomic electrons. At first sight this would appear to be an important consideration because the effective charge of the recoiling ion will affect the rate at which it deposits energy in the gas via the Bethe-Bloch equation, i.e. as z^2. Table 5.1 shows that in this situation, the number of electrons stripped appears to make little difference except in the case where no electrons are lost and hence no ionization is produced in the chamber. This is a surprising result which can be explained by the fact that, for $z = 1 \rightarrow 6$, a carbon nucleus will have a range less than

the pitch of the MSGC, and so the total energy δE deposited on a strip is not affected by $\frac{\delta E}{\delta x}$ of the ion concerned. In the absence of further information, we arbitrarily assumed that scattered ions were singly ionized, i.e. they lose only one electron in the scattering process, and hence believe our results are insensitive to this assumption.

The interaction rates for elastic scattering were calculated using neutron scattering cross sections taken from experimental data [38, 37] for elastic scattering of neutrons on hydrogen, carbon oxygen and argon.

5.2.2 Neutron Capture

Prompt emission of particles causing ionization can result from the capture of neutrons by atomic nuclei.

Such a process is the capture of low energy neutrons by hydrogen nuclei to form deuterons, resulting in the prompt production of a 2.2 MeV photon. This photon can produce ionization in the gas via the processes of Compton scattering or pair production.

$$n + H_1^1 \rightarrow D_1^2 + \gamma \tag{5.5}$$

The cross section for this process is given [39] by

$$\sigma(v) = \frac{6.6 \times 10^4}{v} b \tag{5.6}$$

where v is the velocity of the incident neutron in $cm\ sec^{-1}$. At thermal energies, the cross section is 0.6 b. Considering the high flux of thermal neutrons at ISIS and the amount of hydrogenous material in the MSGC (gas, Mylar etc.), this process could make a large contribution and has thus been included in the model.

Prompt ionizing particles may also be produced by higher energy neutrons penetrating the nucleus to form an unstable 'compound' nucleus. Inside the compound nucleus, the incident neutron undergoes multiple collisions with individual nucleons and the nucleus then decays via one of the processes below, depending on the excitation energy of the compound state:

- elastic scattering - $X_Z^A(n,n)X_Z^A$
- inelastic scattering - $X_Z^A(n,n)X_Z^{A*}$
- radiative capture - $X_Z^A(n,\gamma)X_Z^{A+1}$
- charged particle emission - $X_Z^A(n,p)X_{Z-1}^A$, $X_Z^A(n,\alpha)X_{Z-2}^{A-3}$

The thresholds for such interactions which result in the production of either a photon or a charged particle, are in the region of 1 MeV or more and have a relatively low cross-section[1] and hence are not included in the model.

5.3 Non-Prompt Interactions

5.3.1 Activation of Materials in the MSGC envelope

The capture of thermal neutrons by nuclei contained within the gas and the chamber structure will result in the formation of active isotopes. These isotopes will subsequently decay, emitting α particles, $\beta^{\mp}$s or γs. We need to know the number of active nuclei present in the chamber as a function of exposure time to neutrons in order to compute the rate of production of decay particles, and hence determine the count rate induced in the chamber.

The activity of a material at a particular time may be obtained from the rate of production of the radioactive isotope $Nf\sigma(1-\sigma ft)$ and the radioactive decay formula, dN = -Nλdt. In this situation given a nucleus X which on capture of a neutron forms a radioactive isotope X', the number of X' nuclei per unit volume after t seconds of neutron exposure, $N_{X'}(t)$, is given by

$$\frac{dN_{X'}(t)}{dt} = N_0 f\sigma(1-\sigma ft) - \lambda N_{X'}(t) \tag{5.7}$$

[1] A few mb except where the energy of the incident neutron corresponds to the energy level of an excited state of the compound nucleus. At this energy there is a resonance in the interaction cross section, with a maximum cross section of a few hundred mb. However, performing the integral $\int F(E)\sigma(E)dE$ over the width of the resonance, where F(E) is the flux of neutrons of energy E, shows that the contribution due to the resonance is small.

where N_0 is the number of X nuclei per unit volume at time t = 0, σ is the cross-section for thermal neutron absorption, f is the flux of thermal neutrons and λ the decay constant of isotope X'.

Upon integration this yields

$$N_{X'}(t) = N_0 f\sigma\lambda^{-1}[(1-\sigma ft)+\sigma f\lambda^{-1}+Ce^{-\lambda t}] \tag{5.8}$$

where C is a constant. At time t = 0, assuming no naturally occurring quantities of isotope X', $N_{X'} = 0$. Therefore the number of X' nuclei present after a period of irradiation t is given by

$$N_{X'}(t) = N_0 f\sigma\lambda^{-1}[(1-\sigma ft)+\sigma f\lambda^{-1}-(1+\sigma f\lambda^{-1})e^{-\lambda t}] \tag{5.9}$$

The maximum neutron irradiation period we will be dealing with is approximately 10 years and the neutron absorption cross-section (σ) is extremely small, hence $\sigma f\lambda^{-1}$ and σft are negligible compared to unity in eq. 5.9 and can be ignored, giving us

$$N_{X'}(t) = N_0 f\sigma\lambda^{-1}[(1-e^{-\lambda t}] \tag{5.10}$$

Ar^{40}, which absorbs thermal neutrons forming beta-active Ar^{41}, requires special treatment. Argon forms part of the chamber gas which is pumped through the chamber at a constant rate. As the lifetime of Ar^{41} is relatively long (about 2 hrs), a fraction of the Ar^{41} atoms will flow out of the chamber before they can decay. This can be corrected for roughly by introducing a term $\frac{F}{V}N_{X'}$(t) into eq. 5.7 where F is the flow rate and V is the gas volume inside the chamber. Thus upon integration, eq. 5.7 becomes

$$N_{X'}(t) = \frac{VN_0 f\sigma}{V\lambda+F}(1-e^{-(\frac{F}{V}+\lambda)t}] \tag{5.11}$$

The number of decay particles emitted per second can thus be obtained by substituting the appropriate expression for $N_{X'}$ into the radioactive decay formula.

5.3.2 Beta decay

The basic β decay process is n $\rightarrow$ p + e^- + $\bar{\nu}$ and hence, being a 3-body final state, β's are emitted from a particular radionuclide with a spectrum of energies. Therefore we need to select the energy of a particular β particle when it is emitted from the nucleus before we can calculate the energy which it deposits in its passage through the detection volume. The probability that the β receives an energy E [40] is given by

$$P(\epsilon) = \frac{G_\beta^2 F(Z,E) m_e^5 c^4}{2\pi^3 \hbar^7} \mid M_\beta \mid^2 \sqrt{(\epsilon^2-1)}\epsilon(\epsilon_{max}-\epsilon)^2 \qquad (5.12)$$

where

$$\epsilon = \frac{E}{m_e c^2},$$

G_β is the coupling constant and M_β is the nuclear matrix element. M_β is assumed to be energy independent. F(Z,E) is the Fermi factor which represents the effects of the Coulomb interactions on the energy of the outgoing β particle. These effects of the nuclear electric field may be approximated [41] using

$$F(Z,E) = \frac{2\pi\eta}{1-e^{-2\pi\eta}} \qquad (5.13)$$

where $\eta = \mp Ze^2/\hbar v_e$ for $\beta^\pm$ decays.

In the Monte Carlo model, we select the energy of a β particle using the following method:

- When the program is initialized, we use the CERN library routine FUNPRE to calculate the Cumulative Distribution Function (CDF) of eq. 5.12 for each β decay process in the model, obtaining a distribution for each radioisotope.
- Each time a β decay is generated, CERN library routine FUNRAN is used to map a uniform random number onto the appropriate CDF for the process and hence select an energy for the β.

Table 5.2 lists the isotopes formed by the absorption of thermal neutrons by materials within the MSGC chamber at ISIS. Aluminium (in the anode/cathode strips and the surface of the

Isotope	Production Cross-Section σ(barn)	Decay type	Half Life	Max. β energy (MeV)
Al^{28}	0.21	β	2.3 min	2.9
Si^{31}	0.11	β	157.0 min	1.5
Ar^{41}	0.64	β	110.0 min	1.2
Cr^{51}	16.0	K	28 days	-
Cr^{55}	0.36	β	3.5 min	2.8
Fe^{55}	2.7	K	2.7 yrs	-
Ni^{65}	1.5	β	2.6 hrs	2.1
Cu^{64}	4.5	β	12.8 hrs	0.57
Cu^{66}	2.2	β	5.1 min	2.6
Au^{198}	98.0	β	2.7 days	0.96

Table 5.2: Beta-active nuclei and β energies formed by neutron capture from materials used in the construction and operation of the MSGC

drift cathode) and silicon (in the glass substrate) are important β sources because of their proximity to the active detection volume. Iron, chromium and nickel, although further away from the drift volume, are present in large quantities in the chamber casing.

5.4 Energy Deposition by Charged Particles

Charged particles lose energy as they travel through matter via ionization or excitation of the atoms of the medium. The energy loss determines the number of ion pairs created in the drift space of an MSGC by any charged particle which passes through it.

In this section we summarize the energy loss mechanisms of charged particles and show how they permit energy deposition in the gas to be calculated in the Monte Carlo program.

5.4.1 Charged Particle Energy Losses

Charged particles may lose energy when traversing a medium by the following mechanisms:

1. **Electromagnetic (Coulomb) Interactions** in the medium result in the particle transferring energy to atomic electrons. Close collisions result in large energy transfers and the ionization of atoms. Distant collisions produce smaller energy transfers resulting in either ionization or excitation. The average energy loss by Coulomb collisions is calculated using the Bethe-Bloch equation from Chapter 2:

$$\frac{dE}{ds} = \frac{-KZ\rho}{A\beta^2}\left(\frac{1}{2}\ln\frac{2m(\gamma\beta c)^2}{I} - \beta^2 - \frac{\delta}{2}\right) \tag{5.14}$$

which is valid for relativistic, heavy, charged particles. The expression for non-relativistic particles reduces [36] to

$$\frac{dE}{ds} = \frac{-KZ\rho}{A\beta^2}\left(\frac{1}{2}\ln\frac{4MT}{m_e I}\right) \tag{5.15}$$

where T is the kinetic energy of the incident particle.

These equations must be modified for electron energy loss to account for the difference in reduced mass between the electron-electron and heavy particle-electron collision systems [35]. Eq. 5.14 then becomes, for electrons

$$\frac{dE}{ds} = \frac{-KZ\rho}{2A\beta^2}\left(\ln\left(\frac{(\gamma\beta m)^2 c^4}{I^2}[\gamma - 1]\right) - \beta^2\right) \tag{5.16}$$

and for non-relativistic electrons we have

$$\frac{dE}{ds} = \frac{-KZ\rho}{A\beta^2}\left(\ln\frac{1.16T}{I}\right) \tag{5.17}$$

The heavy particles produced by neutron interactions at ISIS energies are comparatively slow, producing a large number of primary electrons which reduce statistical fluctuations in the amount of energy deposited in the gas. Therefore the use of the mean energy loss is sufficiently accurate for our purposes without the need to take

statistical fluctuations of energy loss into account. Values such as I, the mean ionization potential, were taken from data tables [14] or calculated [15] for the material in question.

In the Monte Carlo model, we only use the Bethe Bloch equation to calculate energy losses in the drift space above the active strips. In the interests of computational speed, energy losses of particles in other regions of the chamber were calculated using the practical range approximation described below.

2. **Radiative energy losses (Bremsstrahlung)** occur when a charged particle is deccelerated in the electric field of a nucleus, the change in energy appearing in the form of a photon. Bremsstrahlung losses for heavy particles such as protons are much less than that for light particles such as electrons.

   Expressed as a fraction of the Coulomb energy loss for a particle of mass M and energy E, the Bremsstrahlung correction [35] is given by

$$\Delta E_{brem} \approx \frac{EZm_e^2}{700M^2}\Delta E_{coll} \tag{5.18}$$

   where ΔE_{coll} is the energy lost by the particle via Coulomb collisions and Z is the atomic number of the medium traversed by the electron.

   However, Bremsstrahlung losses are already included in the practical range approximation given below and which we use for all regions of the chamber except the drift space. This Bremsttrahlung correction is only used therefore in the drift space where we calculate energy loss from the Bethe Bloch equation.

5.4.2 The Range of Charged Particles.

Before we can calculate the amount of energy a charged particle deposits in a drift cell of an MSGC we need to determine whether it is stopped before it reaches the cell. If the particle originates in the drift cell itself, there is no problem. Particles originating outside this region may stop in the intervening material before reaching it. To determine whether or not the

particle is stopped in a material, we use the practical range approximation [14, 36, 35] for charged particles in a medium of density ρ:

$$r_p = \frac{\delta T^n}{\rho} \tag{5.19}$$

where δ and n are constants which depend on the medium and the type of particle (electron, proton etc.), and T is the kinetic energy of the particle. The kinetic energy T' of a particle after passing through a thickness of material, r $< r_p$ is thus given by

$$E' = (E_n - \frac{\rho r_p}{\delta})^{\frac{1}{n}} \tag{5.20}$$

This approximation can equally be applied to electrons and protons travelling through a variety of media, and values of n and δ for electrons and protons in several materials can be found in the sources cited above.

5.5 Effects of Electric and Magnetic Fields

The drift field of an MSGC can be up to 10 kV cm^{-1}. There will be a small effect due to this field which accelerates negatively charged particles towards the MSGC tile, and positively charged particles towards the drift cathode.

In ATLAS, MSGCs will also be operating in a 2T magnetic field parallel to the direction of the drift field. The force exerted on the particle when both electric and magnetic fields are present is given by the Lorentz equation:

$$m\dot{\mathbf{v}} = q(\mathbf{E} + \mathbf{v} \times \mathbf{B}) \tag{5.21}$$

where q and m are the charge and mass of the particle, **E** is the electric field, **B** is the magnetic field and **v** is the velocity. In MSGCs in ATLAS, both **E** and **B** will be perpendicular to the substrate which we define as the z direction.

In the Monte Carlo model, we calculate the change in direction of a particle due to electric and magnetic fields using the following method. For a particle of initial kinetic energy T,

momentum p and speed v = | **v** |, we calculate the energy loss over a small distance δs using the Bethe Bloch equation. Note that v is the instantaneous velocity of an individual electron and not the velocity of the drifting electron cloud. Using the Lorentz equation, the change in momentum due to the effects of magnetic and electric fields in each of the 3 Cartesian coordinates over δs is given by

$$\delta p_x = q v_y B \delta t, \quad \delta p_y = -q v_x B \delta t, \quad \delta p_z = q E \delta t$$

where $\delta t = \frac{\delta s}{v}$. This gives us three equations for the momentum of the particle in each direction

$$p_x = p_x + q v_y B \delta t \tag{5.22}$$

$$p_y = p_y - q v_x B \delta t \tag{5.23}$$

$$p_z = p_z + q E \delta t \tag{5.24}$$

The kinetic energy $T^{'}$ of the particle after travelling a distance δs is

$$T^{'} = T - \frac{\delta E}{\delta s} \delta s \tag{5.25}$$

We use this to calculate the momentum $p^{'}$ and speed $v^{'}$ of the particle after it has travelled a distance δs in the non-relativistic limit, i.e. $p^2 = 2$mT and p = mv. These are used to recalculate the velocity components of the particle and hence its direction of travel at the end of the step interval δs. Finally we multiply each momentum component by $\frac{v^{'}}{v}$ to correct for the energy loss over δs. δs was kept small in comparison with the strip width.

5.6 Ionization Generated Indirectly by Photons

Photons may produce charged particles in a medium by one of four processes:

1. **Photoelectric absorption** is the dominant energy loss mechanism at low photon energies ($E_\gamma < 1$ MeV) in which the incident photon is completely absorbed in one of

the atomic electron shells ejecting a photoelectron. The photoelectric absorption cross-section can be very high (e.g. $\sim 10^5$b for a 6.0 keV photon in argon) but this decreases rapidly with increasing energy. The short range of the low energy photoelectrons so produced (a few mm in argon) means that for the most part only photoelectrons created within the drift space will produce a signal.

In our experiment, the only photons in the energy range where photoelectric absorption is significant, are produced when Fe^{54}, present in the casing of the test chamber, captures thermal neutrons forming Fe^{55}. Fe^{55} decays emitting a 5.89 keV photon which will be reabsorbed in the chamber casing or the intervening gas before it reaches the drift space and are therefore unimportant to us. Neutrons may be absorbed by hydrogen producing 2.2 MeV photons via the np $\rightarrow$ Dγ process. These photons are well above the energy range where photoelectric absoption is a significant process. For these reasons, photoelectric absorption processes have been left out of this simulation.

2. **Compton scattering**. As the photon energy increases to 1 MeV and beyond, Compton scattering, in which a photon scatters from an atomic electron which may be regarded as free, becomes the most probable photon process in the gas.

   When a photon is scattered at an angle θ_s from the electron (see Fig. 5.2), it transfers energy to the electron which recoils at an angle θ_e and kinetic energy T, which may be calculated [14, 35] from

$$T = E_\gamma \lambda \frac{1-\cos\theta_s}{\lambda(1-\cos\theta_s)+1} \tag{5.26}$$

   where $\lambda = E_\gamma/m_e c^2$ and E_γ is the energy of the incident photon. The angle of the recoil electron θ_e is related to the scattering angle, θ_s by

$$\cot\theta_e = (1+\lambda^{-1})\tan\frac{\theta_s}{2} \tag{5.27}$$

   The scattering cross-section as a function of photon energy E_γ and scattering angle θ_s is given by [35]

$$\sigma(E_\gamma,\theta_s) = 0.5 r_e^2 p^2[1+p^2-p(1-\cos^2\theta_s)] \tag{5.28}$$

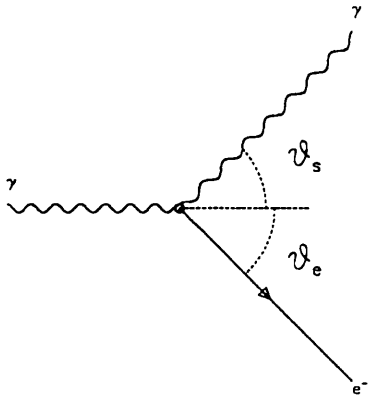

Figure 5.2: Compton scattering of a photon from an atomic electron.

where

$$p = \frac{\lambda}{1+\lambda-\cos\theta_s} \tag{5.29}$$

In the Monte Carlo model, we first calculate the total Compton cross section per atom for a given photon energy by computing the integral of eq. 5.28 over all angles, and multiplying by the atomic number, Z, of the medium the photon is travelling through. To select a scattering angle we use the following method.

- When the program is initialized, we use the CERN library routine FUNPRE to calculate the CDF of eq. 5.28 using a constant value for E_γ. E_γ was taken from data tables listing the energies of photons emitted during decay processes [39, 42].
- Each time a Compton scatter is generated we use the CERN library routine FUNRAN to map a uniform random number onto the appropriate distribution (which depends on the photon energy) and hence select a scattering angle for the photon.

- We then compute the energy and direction of the recoiling electron using eqs 5.27 and 5.26.

3. **Pair production** becomes important when the incident photon energy exceeds a few MeV. In this process, which has a threshold at $2m_e$ (1.022 MeV), the photon annihilates in the electric field of a nucleus or atomic electron, producing an e^+e^- pair. The cross section for pair production [16] is given by

$$\sigma(\lambda) = 4r_e^2\alpha Z^2(\frac{7}{9}\ln 2\lambda - \frac{109}{54}), \qquad 1 < \lambda < \frac{1}{\alpha Z^{\frac{1}{3}}} \tag{5.30}$$

$$\sigma = \frac{7A}{N_A X_0}, \qquad \lambda > \frac{1}{\alpha Z^{\frac{1}{3}}} \tag{5.31}$$

where X_0 is the radiation length of the material being traversed by the photon in g cm^{-2} and $\lambda = E_\gamma/m_e c^2$. At the photon energies we are dealing with, we predict that pair production will have only a small effect but this process has been included in the model.

4. **Photonuclear absorption** becomes energetically possible above energies of a few MeV. However this has been omitted from the simulation as few photons in this energy range are expected.

For photons originating outside the gas volume, the effects of attenuation in the intervening material were calculated using the formula

$$I(x) = I_0 e^{-\frac{\rho N_A \sigma_T}{A} x} \tag{5.32}$$

where I_0 is the original photon intensity, N_A is the Avogadro constant, σ_T is the total photon interaction cross section, ρ is the density of the material, x is its thickness and A is its atomic weight. In the Monte Carlo model, we force all photons to interact in the gas of the sensitive volume, and calculate the distance they must travel through the intervening material in order to get there. We then apply a weight to the photon using eq. 5.32 with I_0 = 1.

5.7 Neutron Spectra

5.7.1 The ISIS Spectrum

Measured data for the neutron energy spectrum at ISIS was only available for a maximum distance of 68cm from the collector (see Fig. 4.2). Our detector had to be positioned at a distance of 475cm from the collector in order to obtain a suitable neutron flux and the neutron energy spectrum at this distance had to be estimated.

To do this, we used the neutron data at 68cm and applied empirical scaling factors [32] using the following relations:

$$flux = \frac{5.26 \times 10^{15}}{3600(H+475.0)^2} ncm^{-2}\mu A^{-1}sec^{-1} \qquad T_n < 10keV \tag{5.33}$$

$$flux = \frac{1.66 \times 10^{13}}{3600(H+16.39)^2} ncm^{-2}\mu A^{-1}sec^{-1} \qquad T_n > 10keV \tag{5.34}$$

where H is the distance from the collector in cm.

Use of these relations produced a discontinuity in the spectrum at 10 keV which was removed by smoothing between the 1 keV and 100 keV points. These calculations resulted in the spectrum shown in Fig. 5.3, valid at 475 cm from the collector.

Neutron energies were selected using the following method:

- When the program was initialized, the CERN library routine HISPRE was used to calculate the CDF of the distribution shown in Fig. 5.3.
- Whenever a new neutron energy was required, the CERN library routine HISRAN was used to map a uniform random number onto the CDF and hence select the energy.

We made the definition that a thermal neutron was any neutron with an energy below 100 eV and a fast neutron was a neutron with energy above 100 eV. The direction of fast neutrons was generated by selecting a random point of incidence in the region of interest, then calculating the angle subtended at this point by the collector. The direction was

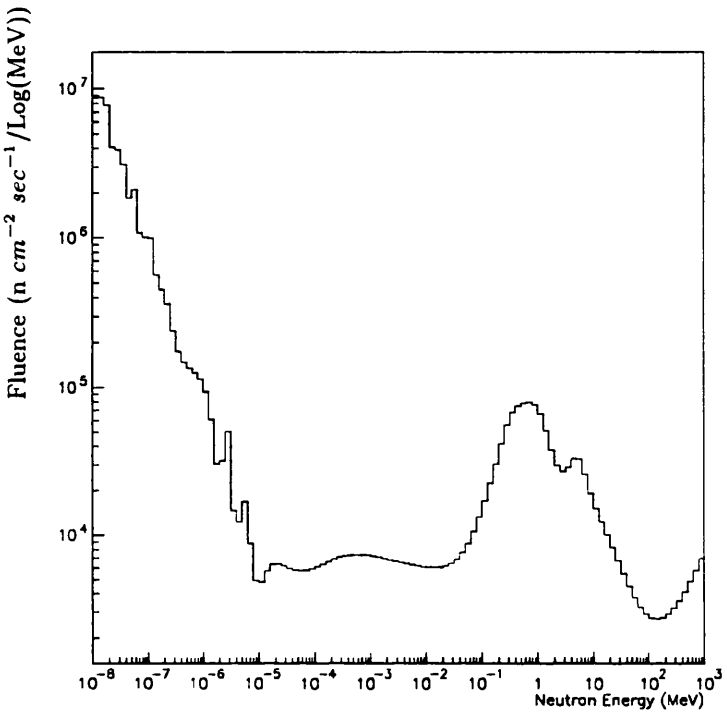

Figure 5.3: Calculated neutron energy spectrum at ISIS, 475 cm from collector.

randomized about this angle according to a Gaussian distribution of width 0.01 radians to account for the solid angle subtended by the collector at the detector.

Thermal neutrons are regarded as isotropic in this model because the only thermal neutron processes we modelled were the np$\rightarrow$dγ process and decay processes, both of which are independent of the direction of the incident neutron. Their incident position was selected randomly over volume of the detector.

5.7.2 The ATLAS Spectrum

The Monte Carlo program took the neutron spectrum predicted in the ATLAS inner cavity [29] (Fig. 4.1) when polyethylene is placed between the calorimeter and the inner detector.

The energy of individual neutrons was sampled using the same method as for the ISIS spectrum.

The direction of neutrons incident on the chamber was selected using an isotropic angular distribution, irrespective of their energy.

5.8 Gas Amplification

5.8.1 Gain

The gain due to the avalanche at the MSGC anodes was treated very simply in this model. Firstly the number of ion pairs deposited in the gas was determined using

$$n_T = \frac{\Delta E}{W_i} \tag{5.35}$$

where n_T is the total number of ion pairs produced, ΔE is the energy deposited in the drift cell and W_i is the average energy required to produce an ion pair, the data being obtained from [14]. The value for n_T was rounded to the nearest integer and multiplied by the gas gain A to give the mean number of electrons collected by the anode strips in the drift cell concerned.

5.8.2 Energy Resolution

The number of electrons produced during the gas amplification process is not a constant multiple of the average number of electrons incident on the avalanche region but instead varies about the mean due to statistical effects. The simulated number of electrons collected by the anodes was randomized by sampling under the energy resolution curve measured for the ISIS MSGC test chamber in Chapter 3. The energy resolution of the chamber is

obtained from the resulting (nearly Gaussian) energy deposition spectrum and was found to be 9 %.

5.9 Implementation of the Model

5.9.1 Neutron-Induced Processes

From the above discussion, the following processes were modelled on the grounds that they were most likely to produce a significant count rate.

1. **ISIS operation**

   (a) Prompt Processes:

   - Elastic scattering of fast neutrons on hydrogen. We modelled this process in the gas volume (isobutane) and in the Mylar drift cathode.
   - Elastic scattering of fast neutrons on other light nuclei (n + C, n + O, n + Ar). We modelled this process in the gas volume (argon, isobutane, CO_2).
   - Thermal neutron absorption, giving rise to photons via the np $\rightarrow$ dγ interaction. We modelled this process in the gas (isobutane), the mylar drift cathode and the epoxy motherboard board which supports the substrate, and in the drift cathode frame.

   (b) Non-prompt Processes:

   - Thermal neutron absorption resulting in beta decay. We modelled this process in the electrodes (aluminium), the stainless steel casing (chromium, nickel and iron), the phosphor bronze contacts (copper), the substrate (silicon), and in the gas (argon).
   - Thermal neutron absorption resulting in the production of photons by decay processes (see section 5.1). We modelled this process in the stainless steel casing (chromium) only.

2. **ATLAS operation**

(a) Prompt Processes:

- Elastic scattering of fast neutrons on hydrogen. We modelled this process in the gas volume (DME) and in the chamber casing which was to be constucted from PolyEtherEtherKetone (PEEK).
- Elastic scattering of fast neutrons on other light nuclei (n + C, n + O, n + Ar). We modelled this process in the gas volume (argon, DME).
- Thermal neutron absorption resulting in photon production ($np \rightarrow d\gamma$). We modelled this process in the gas (DME) and in the chamber casing (hydrogen in PEEK).

(b) Non-prompt Processes:

- Thermal neutron absorption resulting in beta decay. We modelled this process in the electrodes (gold/aluminium), the substrate (silicon) and in the gas (argon).
- In the ATLAS MSGC, we modelled no non-prompt processes resulting in photon emission.

5.9.2 Chamber Geometries

The geometry of the ISIS test chamber differs greatly from that proposed for ATLAS [43]. We describe the geometries of both situations and how they were modelled in the next chapter in which we present the results obtained using the Monte Carlo program.

5.9.3 Logical Flow of the Model

This section deals with the way in which the above mechanisms were implemented in the simulation program.

The program was constructed so that any of the neutron-induced processes could be switched off thereby allowing simulation of specific contributions to the energy spectrum and count rate.

MSGCs operating in both ISIS and ATLAS were modelled using the same program by switching the data describing the beam characteristics and chamber geometries between the two situations.

The program is executed in the following sequence, a diagram of which is shown in Fig. 5.4:-

- The initial energy and direction of the incident neutron is selected according to the required beam type (ATLAS or ISIS) as described in section 5.7.

- Neutrons with kinetic energy greater than 100 eV are considered 'fast' , whereas neutrons with kinetic energy less than 100 eV are considered 'thermal'. Depending on the category of neutron as defined above, one of the two subsequent procedures is executed:

    1. **Fast neutrons** participate in elastic scattering processes only. Of these, only scatters occurring in the Mylar drift cathode or in the counting gas are considered because the range of recoiling ions is short. Elastic scatters by fast neutrons in the chamber casing, in the substrate, and in the motherboard are not modelled.

    We selected a detector component (either the gas or the Mylar window). The program itself was constructed to select each detector component in turn but we also had the option of switching off components so we could look at each process individually. We then found the ratio R = $\frac{M_m}{M_g}$ where M_m is the mass of the component and M_g is the mass of the gas in the active region of the detector. This quantity was rounded to the nearest integer. We define the active detection region as the volume of gas contained between the number of strips modelled and the drift plane. When we consider scattering interactions in the gas, however, we

use the whole gas volume between the drift plane and the substrate and not just the active region.

In order to normalize the count rate induced by interactions in the selected material to the count rate produced by interactions in the active region, we repeat the following sequence R times:-

- We select the initial incident position of the neutron on the detector component as described in section 5.7, and hence calculate the direction according to the appropriate beam profile (ISIS or ATLAS).
- The path of the neutron through the detector component is computed and it is forced to scatter at a random point along this path. All scattering processes (np, nC, nO and nAr) are treated equally in this respect because the mean free path for neutron scattering in each of these cases is greater than 10^4 mm which is much larger than the dimensions of the apparatus.
- The scattering angles, θ, ϕ, of the recoiling nucleus w.r.t the incident neutron are selected isotropically in the CM frame (see section 5.2.1) and used to compute the recoil energy of the scattered nucleus via eq. 5.2 (or 5.3 for protons).
- When simulating neutron induced counting rates in a magnetic field, we need to determine whether charged particles produced by a neutron process outside the active region becomes 'trapped' by the magnetic field and thus do not enter this region. This should be modelled by tracking from the point of origin using the method described in section 5.5. However, this would require large amounts of processor time and hence we make the following crude approximation.

  If the distance to the active region is greater than the radius of curvature induced by motion in the magnetic field, the event is discarded. The radius of curvature is given by r = $\frac{p \cos \lambda}{cBq}$, where p and q are the momentum and charge of the particle, B is the magnetic field, and λ is the initial angle of

the track to a plane perpendicular to the magnetic field.

- Using the practical range formula (see section 5.4.2) we calculate whether the recoiling nucleus can reach the active region. If it can then we calculate the energy lost in passing through the intervening material and hence the energy with which it enters the active region. If it cannot reach the active region, the event is discarded.
- We then calculate the trajectory of the particle through the active region, taking into account the effects due to electric and magnetic fields.

  The particle is allowed to travel a small distance δs, where δs is much less than the width of a strip (or group of strips). The energy loss δE over this distance and the change in direction to allow for the effects of electric and magnetic fields are calculated using the method described in section 5.5. δE is subtracted from the particle energy and allocated to an MSGC detection cell according to its position in the chamber. Each anode or group of anodes thus receives an energy A.ΔE where A is the gain and $\Delta \mathrm{E} = \sum_{i=1}^{n} \delta E_i$ and n is the number of energy depositions in a particular cell.

  This process is repeated until the particle either loses all of its energy or leaves the active area.
- We use the measured energy resolution of an MSGC to randomize the energy deposited in each cell about the value calculated in the above process (see section 5.8.2).
- A weighting factor is applied to the energy deposited in each cell. This depends on the probability of one neutron interacting in the selected detector component and is given by

$$W = \frac{M_m N_n N_A \sigma}{A} \tag{5.36}$$

where N_n is the number of scattering centres present in a molecule of material,

N_A is Avogadro's number and A is the atomic mass. Because we repeat this sequence R times for each material, the weighting factor we apply is thus $\frac{W}{R} = \frac{M_g N_n N_A \sigma}{A}$.

- If this is not the final iteration, we generate another **fast** neutron (selecting its energy and direction as described above) and continue until R neutrons have been examined.

2. **Thermal neutrons** as defined above, participate in absorption processes only. These may result in prompt emission of photons (via np $\rightarrow$ dγ) or the non-prompt emission of β particles or photons via subsequent radioactive decay.

   For each process in a detector component (chamber casing, electrodes, gas etc) we find the ratio R = $\frac{M_m}{M_g}$ where M_m is the mass of our chosen material and M_g is the mass of the gas in the active region of the detector and, using the same treatment as for 'fast' neutrons, repeat the following sequence R times:

   - Select the initial incident position of the neutron on the detector component. We do not need the trajectory of the neutron for these interactions as the final state particles are emitted isotropically irrespective of incident direction.
   - Although the βs and γs are emitted isotropically, in order to reduce the number of events discarded due to their missing the active region, we force them to be emitted in a direction such that they will pass through the active volume. (This introduces a factor of $\frac{\Omega}{4\pi}$ into our weighting factor when we calculate count rates, where Ω is the solid angle subtended by the active region at the interaction point.)
   - The next step depends on whether we are dealing with a β particle or a γ:

     (a) For a β particle, we select its energy using the procedure outlined in section 5.3.2.

     We determine whether the particle is trapped by any magnetic field using the same method as used for scattered ions.

We use the practical range formula to calculate whether the electron can reach the active area and if so, calculate its energy after passing through the intervening material; otherwise this event is discarded.

(b) When simulating energy depositions from photons, an event is generated for each modelled photon interaction. If the energy of the photon is less than 1.022 MeV (the pair production threshold), we generate a single Compton event only. If however the energy of the photon exceeds 1.022 MeV, we also generate an e^-e^+ pair. We force photons to interact in the active region only, thus Compton scattering and pair production processes both receive a weighting factor based on the probability of these processes occurring in the active gas volume.

When a Compton electron is generated, we select a photon scattering angle θ_s by sampling under the Compton scattering distribution (eq. 5.28). Eq.s 5.27 and 5.26 are then used to generate the direction and energy of the recoiling electron.

In the case of pair production, for initial photon energies of a few electron masses, the relative energy sharing between the electron and positron is approximately flat [14]. We thus use this approximation because we are only dealing with photon energies of a few MeV. The positron energy is selected randomly between 0 and E_γ-1.022 MeV (using a flat distribution) and the electron is assigned the remaining energy (E_γ - 1.022 - E_{e+}). The electron and positron directions are assumed to be identical.

- The path of the electron through the active area and the energy deposited are calculated using the same method as for scattered ions.
- As before, the energy deposited on each strip is smeared using the measured energy resolution of an MSGC.
- A weighting factor is applied to the energy deposition rate for each strip. This depends on the probability of one neutron interacting in the selected

detector component which is given by

$$W = \frac{M_m N_A \sigma}{A} \tag{5.37}$$

where A is the atomic mass of the material. This reduces to $\frac{W}{R}$ as described above for fast neutrons.

This weight is multiplied by $\frac{\Omega}{4\pi}$ to compensate for the fact that the β or photon is forced to pass through the drift space. In addition the following multpliers must also be applied to weight each energy deposition:-

(a) For particles produced by decay processes, the weight of the event is multiplied by $\frac{\lambda N_{X'}(t)}{r_{X'}}$ where λ is the decay constant of the radionuclide, $N_{X'}(t)$ is the number of active nuclei present per unit mass after t seconds of neutron irradiation and $r_{X'}$ is the rate of production of the radioisotope per unit mass.[2]

(b) For Compton electrons we multiply the weight by $\frac{N_A \sigma_c m_g Z}{A}$, the probability that the photon will interact in the active region. Here σ_c is the Compton cross section, A is the atomic mass of the gas and Z is the atomic number of the gas.

(c) For energy depositions that are a result of pair production, we multiply the weight by $\frac{N_A \sigma_p m_g}{A}$, where σ_p is the cross section for pair production and A is the atomic mass of the gas.

– If this is not the final iteration, we generate another **slow** neutron and continue until R iterations have been performed.

The model was tested by using a debug mode to keep track of the values of certain quantities such as the neutron energy and rate of energy loss at each stage of processing. These quantities could then be calculated by hand and the two results compared. A number

[2] When t >> τ, the half life of the radioisotope, $\frac{\lambda N_{X'}(t)}{r_{X'}} \approx 1$.
This is the case in ATLAS but not in ISIS .

of debug histograms (such as a histogram of the selected neutron energies) were also produced which acted as a further check.

5.9.4 Summary

We have described in detail the physical processes we believe will produce the largest contributions to the count rate observed when irradiating MSGCs with a high flux of low energy neutrons. We have also described the construction of a Monte Carlo model designed to simulate these processes. The next chapter will describe how we applied the model to the two different situations of MSGCs in an ISIS environment and MSGCs in an ATLAS environment. We then present the results obtained from running the Monte Carlo using these two sets of conditions.

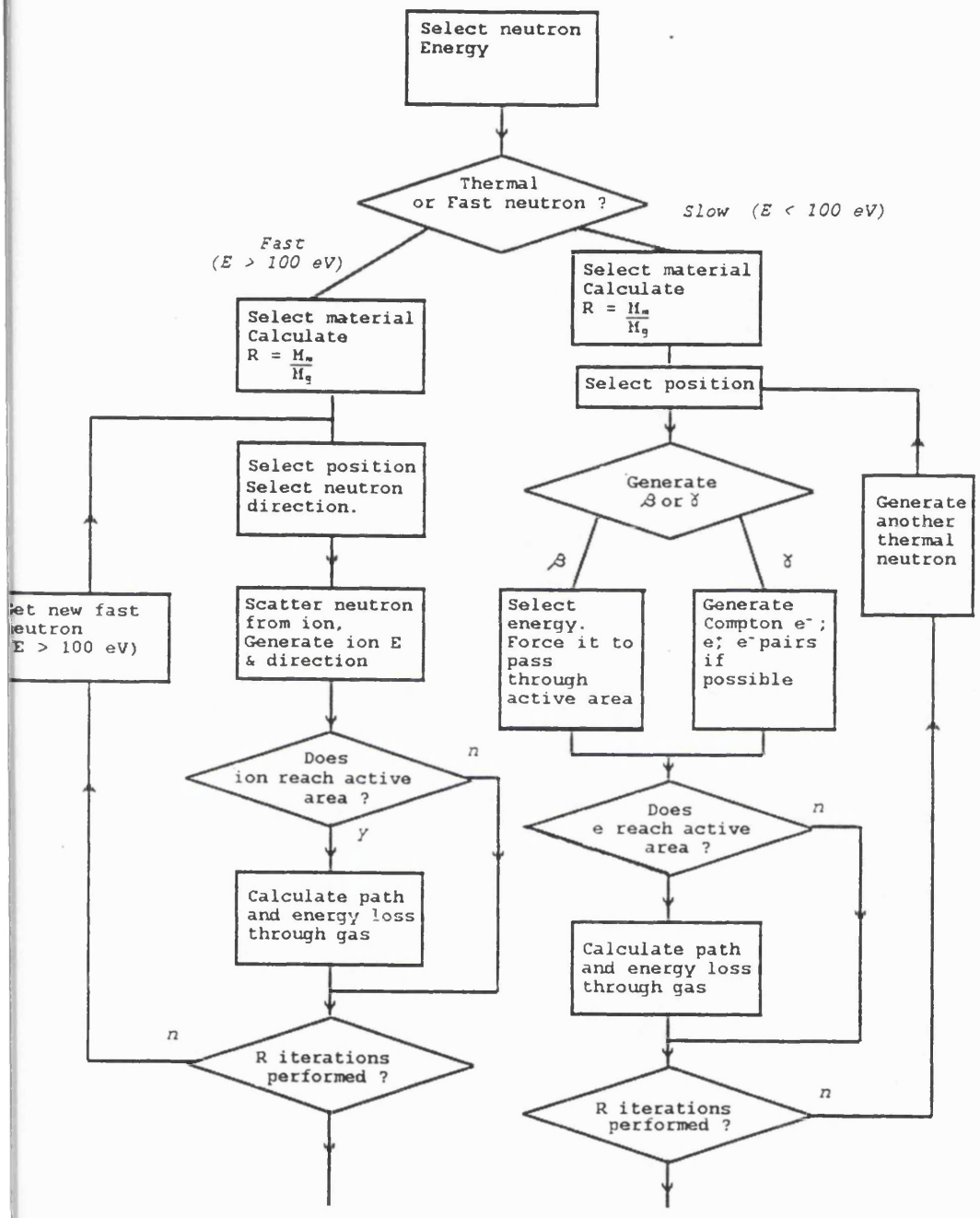

Figure 5.4: Diagram showing the logical flow of the neutron Monte Carlo program.

Chapter 6

Results from Simulation of MSGC Response to Neutrons

6.1 Comparison of Model with Experimental Data

6.1.1 Simulation of ISIS Experiment

In order to validate the use of our Monte Carlo model for predicting neutron induced background in MSGCs at ATLAS, we first compare its predictions to the experimental data obtained from the neutron irradiation studies at ISIS (Chapter 4). The ISIS MSGC test chamber materials and dimensions together with the measured ISIS neutron energy spectrum were entered into the Monte Carlo model in order to simulate the count rates induced by each component of the detector. We summarize the chamber parameters below and indicate how they were modelled in the simulation:

- The ISIS MSGC was equipped with a s8900 tile with aluminium electrodes ganged together in a group of 20. The strip geometry was rectilinear with anode pitch of 300 μm. In the simulation, the strips were treated as a 50 $\times$ 50 mm layer of aluminium

1 μm thick and energy depositions as a result of beta emissions from the strips were weighted by a factor of 0.5 to account for the spaces between them. When modelling beta emissions from the substrate, the s8900 was treated as pure SiO_2.

- The drift electrode was made from a sheet of aluminized mylar stretched over a frame of G10 and the drift distance was 8.5 mm. The Mylar ($C_5H_4O_2$) backing was treated as a flat layer 50 μm thick when simulating neutron scattering and thermal neutron absorption (resulting in photon emission via np $\rightarrow$ dγ). A molecule of Mylar was treated as hydrogen and scatters from Mylar were weighted by a factor of 4. The aluminium coating was treated as a 1 μm thick layer. The coating has a twofold effect because the thickness of the aluminium not only affects the number of β particles emitted into the chamber but may also stop scattered protons from the Mylar.

- The G10 motherboard was treated as Mylar for the purposes of the simulation. We only consider photons from the np $\rightarrow$ dγ process in this component because it sits beneath the substrate which will stop any scattered nuclei from reaching the gas. The frame supporting the drift cathode was sufficiently far away from the drift cell for the effects of scattered nuclei to be ignored.

- The anode/cathode electrode contacts were made from thin strips of phosphor bronze, two for each group of strips. These were modelled as copper plates with dimensions 4 mm $\times$ 3 mm $\times$ 150 μm tilted at 45^o to the plane of the substrate.

- The chamber casing was made from stainless steel (containing iron, nickel and chromium) and had dimensions of 300 $\times$ 270 $\times$ 150 mm $\times$ 3 mm thick. The casing had a 75 $\times$ 75 mm Mylar window which was modelled as above.

- The gas mixture was treated as if it comprised single 'molecules' with parameters such as atomic number taken as a weighted average of its components. All of the nuclei comprising a 'molecule' of this composite gas could scatter fast neutrons. Hence each scatter generated was weighted by the number of nuclei in a molecule of each

component, multiplied by the proportion of the component in the gas mixture. For example, in scattering from hydrogen in a 75 % argon, 25 % C_4H_{10} mixture, the weight would be $10 \times 0.25 = 2.5$. The gas was treated as a layer 8.5 mm thick. The ISIS flow rate of 300 $cm^3\ min^{-1}$ was used to correct for the loss of radioactive argon due to the flow of gas.

- The calculated ISIS energy spectrum (Fig. 5.3) was used.

- The rods and spacers supporting the substrate and drift cathode within the box were ignored, as were the electrical connections.

Each experimental configuration used in the ISIS test run was modelled to generate spectra and count rates for both argon/isobutane and argon/CO_2 operation, with neutrons at both parallel and perpendicular incidence to the strips.

The program was executed separately for each suspected component of the neutron induced signal in order to identify the relative contribution of each one. In addition, it was executed separately using either thermal or fast neutrons only, depending on the process being modelled. Each component studied in this way then had to be normalized when calculating the spectra and count rates.

For each run of the program we generated a fluence ($flux_{MC}$) of 10^3 n cm^{-2} (or more if processor time allowed) to reduce statistical errors. The resulting data were multiplied by $\frac{flux_{ISIS}}{flux_{MC}}$ to give results for ISIS neutron fluxes for 20 ganged strips. We calculated count rates in Hz cm^{-2}, where the area is measured parallel to the tile, by dividing the total number of counts by the active area (i.e. 20×300 μm $\times$ 50 mm).

To compare between simulated and experimental data, we look at the count rates for energy depositions above 2 keV, 5 keV and 100 keV on 20 strips, these boundaries having been selected for the reasons given in Chapter 4.

6.1.2 Discussion and Results

We expect electrons to deposit relatively small amounts of energy over 20 strips in comparison to heavier particles. Applying eq. 5.19 to electrons in the gas[1] we calculate that an electron travelling parallel to the strips can deposit a maximum energy of 80 keV along their 5 cm length. Very few electrons will travel exactly parallel to the strips and hence most energy deposits will be considerably smaller than this.

Energy deposits from photon interactions are expected to be of the same order because Compton scattering and pair production both result in energy deposition via electrons.

We expect a large number of electrons from β-decays in the chamber because of the high thermal neutron flux at ISIS and the large quantity of potentially β-active material used in the construction of the MSGC chamber. Electrons have a long range in gas but can be stopped by small thicknesses of solid material, therefore we expect the largest contribution to the beta signal to come from materials close to the active detection region.

We also expect to see a sizeable photon component from the process $np \rightarrow d\gamma$ due to the large quantity of hydrogenous material in the chamber and the high penetrating power of photons. These photons of energy 2.2 MeV were only slightly above the pair production threshold and thus we would expect them to be detected primarily via the Compton scattering process.

The signal produced in the detector by scattered ions would be expected to be characterized by a wide range of energy deposits which depend on the energy of the incident neutron and the energy transferred to the scattered ion. Ions have a relatively short range so we would expect any entering the drift space to deposit all or most of their energy there. The largest energy deposits are expected to come from heavier nuclei because, although they receive less energy in the scattering process, their range is shorter and hence they deposit their energy over a shorter distance. Thus relatively few counts are expected to arise from scattered ions unless they originate in the active volume of the gas. Higher energy ions have

[1] where n and δ are 1.72 and 0.71 respectively

a longer range but comparatively few of these are to be expected because of the relatively small component of fast neutrons at ISIS.

		Count Rate (Hz cm^{-2})		
Component	Process	$\Delta E > 2$ keV	$\Delta E > 5$ keV	$\Delta E > 100$ keV
Cu (contacts)	β	530	370	0.0
Al (electrodes)	β	16	6.7	0.0
Ar (gas)	β	120	48	0.0
Steel - Cr,Ni (case)	β	0.15	< 0.1	0.0
Steel - Cr (case)	γ	< 0.1	< 0.1	0.0
Si (substrate)	β	0.47	0.24	0.0
H (C_4H_{10}, G10)	np $\rightarrow$ dγ	130	60	0.0
H (Mylar)	n+p $\rightarrow$ n+p	17	16	11
H (C_4H_{10} gas)	n+p $\rightarrow$ n+p	23	21	14
C (C_4H_{10} gas)	n+C $\rightarrow$ n+C	3.1	2.9	1.0
Ar (gas)	n+Ar $\rightarrow$ n+Ar	0.60	0.56	0.20
All Processes		840	520	26

Table 6.1: Monte Carlo predictions for count rates induced by individual processes at ISIS for argon/isobutane operation with neutrons parallel to the strips.

The results obtained from the Monte Carlo model for argon/isobutane operation are presented in Figs. 6.2, 6.3 and Table 6.1. We see that it predicts, for energies below 100 keV, that the signal arises mostly from electrons and photons. This supports our previous reasoning that photons and β particles may only deposit a maximum of 100 keV in the ISIS chamber when filled with argon/isobutane.

Beta decay of Cu^{66} in the phosphor bronze contacts produces the largest contribution to the low energy signal, presumably due to the high formation cross-section (see Table 5.2),

short decay time and the proximity of the contacts to the active region.

Beta decays from Ar^{41} make a sizeable contribution, despite the flow of gas through the chamber which transports some active argon nuclei out of the chamber before they can decay.

		Count Rate (Hz cm^{-2})		
Component	Process	$\Delta E > 2$ keV	$\Delta E > 5$ keV	$\Delta E > 100$ keV
Cu (contacts)	β	430	200	0.0
Al (electrodes)	β	5.6	0.87	0.0
Ar (gas)	β	24	8.6	0.0
Steel - Cr,Ni (case)	β	< 0.1	< 0.1	0.0
Steel - Cr (case)	γ	< 0.1	< 0.1	0.0
Si (substrate)	β	0.19	< 0.1	0.0
H (C_4H_{10},G10)	np $\rightarrow$ dγ	21.2	5.1	0.0
H (Mylar)	n+p $\rightarrow$ n+p	16	16	9.4
C (CO_2 gas)	n+C $\rightarrow$ n+C	1.5	1.4	0.5
O (CO_2 gas)	n+O $\rightarrow$ n+O	3.1	3.0	1.0
Ar (gas)	n+Ar $\rightarrow$ n+Ar	0.4	0.38	0.13
All Processes		500	230	11

Table 6.2: Monte Carlo predictions for count rates induced by individual processes at ISIS for argon/CO_2 operation with neutrons parallel to the strips.

For "fast" neutrons (i.e. E > 100 eV), energy depositions in the chamber are predicted to arise solely from ions produced in elastic scattering processes, with the n+p $\rightarrow$ n+p interaction dominating the high end of the spectrum.

Results for argon/CO_2 operation are presented in Figs. 6.4, 6.5 and Table 6.2. It will be noted that the Monte Carlo model predicts generally smaller energy depositions than for

argon/isobutane due to the smaller energy deposition rate of particles travelling through carbon dioxide compared to isobutane.

The Monte Carlo model also predicts a lower rate of energy deposits as a result of neutron scatters in argon/CO_2 due to the absence of hydrogen in the quencher, and a significant reduction in photon production via the np $\rightarrow$ dγ process.

Fig. 6.6 and Table 6.3 compare the Monte Carlo data with the experimental data obtained at ISIS. The agreement we achieve is reasonable for argon/isobutane but not so good for argon/CO_2. This difference may lie with the CO_2 experimental data due to the problems with discharges we experienced when operating with CO_2 mixtures (section 4.4).

Above 100 keV, we find that the count rates predicted by the Monte Carlo model and those obtained from experiment only agree to within a factor of 4. This agreement is not unreasonable given the uncertainties in the energy spectrum and neutron fluxes at 475 cm from the collector in ISIS. Such uncertainties are particularly likely to have a large effect on the scattering of fast neutrons on hydrogen because the cross section for this process varies rapidly with the energy of the incident neutron.

Configuration	Count Rate (Hz cm^{-2})					
	$\Delta E > 2$ keV		$\Delta E > 5$ keV		$\Delta E > 100$ keV	
	MC	Expt	MC	Expt	MC	Expt
Ar/C_4H_{10}, n $\parallel$	840	930	520	470	26	7.3
Ar/C_4H_{10}, n $\perp$	850	960	540	500	34	7.1
Ar/CO_2, n $\parallel$	-	-	230	410	11	3.0
Ar/CO_2, n $\perp$	-	-	230	66	7.3	2.3

Table 6.3: Comparison of counting rates predicted by Monte Carlo with experimental data obtained from ISIS.

6.2 Predictions for ATLAS

The agreement between the results obtained from the Monte Carlo model and the experimental data from ISIS gives us confidence that the model is simulating the important physical processes involved when low energy neutrons, with an energy spectrum not too dissimilar to that expected in ATLAS, produce signals in an MSGC. Therefore in this section, we use the same model to study these signals, and hence any operational problems which they might produce, in an ATLAS environment.

We calculate the count rates produced by neutron interactions in the same way as was done for the ISIS experiments and study the relative contributions from each process.

However we note that in the case of ATLAS, a significant rate of large energy depositions may produce significant amplifier dead times leading to a large increase in apparent occupancy. Hence we will also study the neutron-induced increase in occupancy which includes the finite decay time of MSGC preamplifiers in ATLAS, as well as the neutron-induced counting rate.

Such large energy depositions may also result in a significant increase in current drawn by the chamber. Hence we will also study how neutron-induced energy depositions affect the charge loading on MSGCs, noting that this could have an impact upon aging properties of chambers.

6.2.1 ATLAS Operating Conditions

The operating conditions in ATLAS will differ from those at ISIS in a number of important respects:

1. The neutron spectrum expected at ATLAS will differ from the ISIS spectrum (Chapter 4). In particular, the fast neutron component will be an order of magnitude larger at ATLAS.

2. ATLAS chambers will operate in a 2T magnetic field approximately parallel to the drift field.

3. The probable design [43] of the MSGC for ATLAS is radically different to that used at ISIS. We list the differences in construction as follows:

   - ATLAS MSGCs will be equipped with a s8900 coated tile with gold electrodes instead of aluminium, and single strip read-out instead of the 20 ganged strips used at ISIS.
   - MSGCs in ATLAS will have keystone instead of rectilinear geometry with a mean anode pitch of 200 μm. The chamber will have a length of 168.7 mm and a width which varies between 122.3mm and 146mm due to the keystone geometry.
   - The drift electrode in the ATLAS chambers will be constructed from a 200 μm thick plate of D263 glass with a gold coating on one side instead of the aluminised Mylar used in the ISIS studies.
   - MSGCs in ATLAS will have a drift space of 2.5 mm (instead of 8.5mm).
   - The drift plane and substrate plane will be separated by the surround for the gas envelope which will be made from PEEK (PolyEtherEtherKetone).
   - The gas mixture currently favoured for ATLAS operation is argon 50 %, DME 50 % [1] as opposed to the argon/isobutane mixture used at ISIS.

The simulation took Ferrari's neutron energy spectra [30] and a total flux of 4 $\times 10^6$ neutrons $cm^{-2}sec^{-1}$, the highest predicted neutron flux in the inner cavity. Neutrons were allowed to enter the chamber from any direction. When applying eq. 5.10 in order to obtain decay particle fluxes, the irradiation time, t, was set at 2 years. This effectively makes the flux of decay particles from materials in the chamber solely dependent on the thermal neutron flux and the absorption cross-section, and independent of the decay rate.

We made a number of approximations to the chamber design which we list below:

- Rectilinear geometry was used in place of keystone geometry. A rectangular chamber measuring 168.7 mm × 122.3 mm was used in place of the structure described above.

- The chemical formula for Mylar was used for the surround of the gas envelope because we were unable to obtain the chemical formula for PEEK and like PEEK, Mylar is rich in hydrogen. The densities of the two materials are also similar; PEEK has a density between 1.26 and 1.32 g cm^{-3} and Mylar has a density of 1.39 g cm^{-3}.

- In order to save processing time and memory, the simulation used an active detection area of 20 × 300 μm × 160 mm as opposed to the full instrumented region of a complete MSGC module. Our initial configuration was an MSGC equipped with gold strips of 300 μm pitch and the active detection area of 20 strips was positioned in the centre of the chamber. The Monte Carlo model simulated the energies deposited on each strip in the group. Later the pitch was changed to 200 μm and the sample region positioned at both the centre and at the edge of the chamber in order to study any differences in energy deposition spectra as a function of strip position.

- We assumed that the gas flow rate would be about 10 $cm^3 min^{-1}$ per module.

The same procedure was followed as was used to calculate the ISIS results. Each component was studied separately, running with a fluence of 1000 n cm^{-2} and multiplying by $\frac{flux_{ATLAS}}{1000}$ to give the counting rate at ATLAS fluxes. We studied energy depositions for each strip as opposed to the total energy deposited over the whole group of strips. In order to find the count rate in Hz cm^{-2}, we divide the count rate per strip by the area of a detection cell.

6.2.2 Energy Cuts

An important consideration for ATLAS is how the energy depositions due to the neutron background compare with the energy deposited by a mip. A mip will deposit, on average,

750 eV in a 2.5 mm gas gap filled with 50 % argon/ 50 % DME, and it is this that we use as a guide to define our energy cuts.

To calculate the increased occupancy of the detector due to neutron-induced processes, we define the following thresholds for the energy deposited in the drift space:

1. **26 eV (1 electron)**. The average energy required for the creation of a single ion pair.

2. **130 eV (5 electrons)**. This figure is expected to approximate to the detection threshold of the read-out electronics [44] and is the minimum value which will be seen above noise.

3. **260 eV (10 electrons)**. We take this to be the discriminator setting that will be used at ATLAS and is approximately one third of the energy deposited by a mip. Thus counts with less than 10 electrons deposited in the drift space are assumed not to be recorded by the DAQ. They will however still contribute to the ion loading of the chamber (see later).

6.2.3 Comparison of Gold and Aluminium Electrodes

The studies at ISIS used MSGCs with aluminium electrodes whereas MSGCs in ATLAS will use gold electrodes. Both of these materials absorb thermal neutrons forming unstable isotopes which subsequently emit β particles.

In order to compare the effects of using gold electrodes instead of aluminium, we ran the Monte Carlo model for both materials using the ATLAS neutron spectrum and the highest neutron flux in the inner cavity ($4 \times 10^6\ cm^{-2}sec^{-1}$), and studied only the energy deposited by β particles from radioactive gold and aluminium. The results are given in Table 6.4 for the case when there is no magnetic field.

Table 6.4 shows that a much larger count rate is obtained from MSGCs equipped with gold electrodes than with aluminium electrodes. Au^{198} and Al^{28} both have very short half lives (2.7 days and 2.3 minutes respectively) compared to the running time of ATLAS and

Energy Deposited	Count Rate (Hz cm^{-2})	
δE	Al strips	Au strips
> 26 eV	77	25000
> 130 eV	29	11000
> 260 eV	17	6400
> 1 keV	4.2	1800
> 5 keV	0.2	120
> 10 keV	0.0	30

Table 6.4: Counting rates in ATLAS due to neutron induced β emission from Al and Au electrodes (pitch 300 μm, E = 0, B = 0).

so the rate of emission of β particles depends solely on the rate of absorption of thermal neutrons. Very many more β particles are produced by gold because, at 98 b, its cross-section for thermal neutron absorption greatly exceeds that for aluminium (0.21 b) and in addition the density (19.3 g cm^{-3}) of gold is greater than that of aluminium (2.7 g cm^{-3}).

6.2.4 Magnetic Field Effects

MSGCs in ATLAS will operate in a 2T magnetic field parallel to the drift field. The field will have a significant effect on β particles travelling in a direction which is not parallel to the field, but a much smaller effect on a proton with a similar kinetic energy and direction.

We illustrate this with the example of a proton with kinetic energy of 1 MeV, and an electron with kinetic energy of 1 MeV both moving in a direction perpendicular to a 2T magnetic field. The particles will move in a circle with a radius (in mm) given by $R = \frac{p}{0.3qB}$ where p is the momentum (in MeV/c) and q is the charge of the particle. From this we see that a 1 MeV electron describes a circle of radius 1.7 mm whereas a 1 MeV proton describes a circle of radius 72 mm.

We would thus expect β particles travelling in a direction perpendicular to the field to deposit all of their energy over a small number of strips. However any component of the electron velocity parallel to the magnetic field plus the presence of an acceleration due to the electric field could result in the β particle leaving the active region before it lost all of its energy. Hence the presence of a magnetic field will cause a large reduction in β count rate because the electrons may no longer cross a large number of strips but are constrained by the magnetic field. We would, however, expect to see a smaller effect of the magnetic field on the spectra or count rates of scattered ions because their radius in the magnetic field will be typically large compared to the pitch of the strips.

δ E	Count Rate Hz cm^{-2}							
	Au	Si,Ar,PEEK	DME			Argon	PEEK	
	β	β,γ	n+p	n+C	n+O	n+Ar	n+p	Total
> 26 eV	25000	5.2	2900	190	97	35	270	28000
> 130 eV	11000	1.6	2700	165	86	33	260	14000
> 260 eV	6400	0.9	2500	150	79	31	260	9500
> 1 keV	1800	0.2	2100	130	71	30	230	4400
> 5 keV	120	< 0.1	1700	100	60	27	100	2100
> 10 keV	30	< 0.1	1500	88	54	26	49	1700
> 100 keV	0.0	0.0	320	35	24	15	2.7	390
> 1 MeV	0.0	0.0	< 0.1	0.52	1.0	2.4	0.0	3.9

Table 6.5: Predicted counting rates in ATLAS for MSGC with Au electrodes, pitch 300 μm. (E = 0, B = 0)

The results obtained from the Monte Carlo model confirm this general picture. Tables 6.5 and 6.6 show that the count rates from β particles emitted by gold are much reduced in the presence of a magnetic field. We also observe a change in the energy deposition spectrum

due to the magnetic field with the largest number of depositions occurring in the 260 eV to 1.0 keV band when fields are applied, compared to the no field case when most of the energy depositions occur in the 26 eV to 130 eV band.

The Monte Carlo results also confirm the expectation that electric and magnetic fields will make little difference to the count rates and spectra due to scattered ions.

Figs. 6.7 and 6.8 show the energy deposition spectrum predicted for MSGCs in ATLAS (including the effects of the magnetic field). We see that scattered ions make a much larger contribution to the overall signal at ATLAS than at ISIS (Figs. 6.2, 6.3) due to the much larger flux of fast neutrons.

δ E	Count Rate (Hz cm^{-2})							
	Au	Si,Ar,PEEK	DME			Argon	PEEK	
	β	β,γ	n+p	n+C	n+O	n+Ar	n+p	Total
> 26 eV	4100	0.5	2800	190	97	34	250	7500
> 130 eV	3400	0.3	2600	170	86	32	245	6600
> 260 eV	2800	0.2	2500	150	79	31	240	5800
> 1 keV	1100	0.1	2100	130	72	30	210	3600
> 5 keV	150	< 0.1	1600	100	60	27	84	2000
> 10 keV	53	< 0.1	1400	87	54	26	47	1700
> 100 keV	0.0	0.0	330	35	25	15	3.4	410
> 1 MeV	0.0	0.0	0.0	0.52	0.95	2.4	0.0	3.9

Table 6.6: Predicted total counting rates in ATLAS for MSGC with Au electrodes, pitch 300 μm. E = 10 kV cm^{-1}, B = 2T

6.2.5 Variation of Pitch and Strip Position

So far we have studied the neutron induced count rates for strips with 300 μm pitch in the centre of the chamber.

If we study strips close to the casing, we expect to see an increase in the counting rate from the elastic scattering of fast neutrons on hydrogen in the PEEK material used in its construction. Fig. 6.9 shows the distribution of energy depositions per strip arising from n-p scattering in PEEK only, with strips positioned in the centre (far from the casing) and at the edge of the chamber (close to the casing). We see that the model does predict a larger signal due to n-p scattering close to the edges of the chamber. The total counting rates from all processes obtained in these two cases are presented in Table 6.7.

If we change the pitch from 300 μm to 200 μm, we expect an increase in the overall count rate due to particles crossing a greater number of strips, but a decrease in the size of energy depositions because of the smaller strip width. These results are given in Table 6.7 and support the above expectation.

6.2.6 Calculation of Neutron-Induced Occupancies in ATLAS

The occupancy of a detector module is the percentage of detection channels that are registering a hit (i.e. have signals on them that are above threshold) in a given bunch crossing. The increase in occupancy due to neutron background in ATLAS depends on both the count rate per strip for neutron induced particles and their energy spectrum because the duration of the pulse produced by the pre-amplifier will be a function of the energy deposited. We have already seen that the size of a significant number of neutron-induced counts will be many times larger than that produced by a mip and are bound to saturate the pre-amplifier thus keeping it above threshold for far longer than would a mip. This will cause an increase in occupancy dependent upon the amplifier response. For example, if the duration of the amplifier output pulse is above threshold for say 50 ns (i.e. two LHC bunch crossings), then the occupancy due to this process will be double that derived simply from the rate alone.

δ E	Count Rate (Hz cm^{-2})			
	Pitch = 200 μ		Pitch = 300 μ	
	Centre	Edge	Centre	Edge
> 26 eV	9000	11000	7500	8800
> 130 eV	7300	7800	6500	6400
> 260 eV	6000	6800	5800	5600
> 1 keV	3300	4600	3600	4000
> 5 keV	1900	2400	2000	2200
> 10 keV	1500	1800	1700	1600
> 100 keV	320	300	410	330
> 1 MeV	2.6	2.2	3.9	2.8

Table 6.7: Counting rates in ATLAS for MSGCs with pitches 200 μm and 300 μm, at the centre, and on edge of chamber. Au electrodes. (E = 10 kV cm^{-1}, B = 2T)

The increased occupancy of a MSGC in ATLAS as a fraction of charged particle occupancy can be calculated by summing the dead time for all neutron-induced counts, and dividing by the total dead time for the signal produced by the ATLAS charged particle flux. The fractional increase in the charged particle occupancy caused by neutrons, is thus:-

$$\text{Fractional Occupancy Increase} = \frac{\sum_{n\ counts\ cm^{-2}} \delta t_n}{\sum_{mip\ counts\ cm^{-2}} \delta t_{mip}} \tag{6.1}$$

where δt_n and δt_{mip} are the times for which the pre-amplifier is above threshold for each neutron-induced and mip energy deposition respectively.

In ATLAS, the current design of the pre-amplifier planned to read out the anode strips will have a rise time of 15 ns and fall time of 500 ns [1]. Fig. 6.1 shows its response as a

function of the number of input electrons obtained using the SPICE simulation program [45]. A mip will deposit approximately 750 eV (29 electrons) in the chamber which for this calculation we assume will be deposited on a single strip by all charged particles. Thus eq. 6.1 becomes

$$\text{Fractional Occupancy Increase} = \frac{\sum_{n\ counts\ cm^{-2}} \delta t_n}{Flux_{mip} \times \delta t_{mip}} \tag{6.2}$$

where $Flux_{mip}$ is the charged particle flux. Assuming a MSGC gain of 3000, Fig. 6.1 shows that we expect the dead time for a mip to be 260 ns. For each neutron-induced event generated by the model, Fig 6.1 is used to find δt_n for that event. MSGCs are situated between 40 and 100 cm from the beam pipe, hence we use the charged particle fluxes at these points to compute the increased occupancy. A discriminator setting of 10 electrons (260 eV) is assumed and so only neutron-induced events resulting in the deposition of 260 eV or more on a single strip are considered.

Results so obtained for the neutron-induced occupancy are given in Table 6.8. We see that the neutrons only produce a small increase in the overall occupancy of the detector, even when allowing for effects due to the amplifier.

6.2.7 Calculation of Neutron-Induced Charge Loading in ATLAS

The deposition of large amounts of energy in MSGCs by neutron-induced particles may result in a significant increase in charge loading, i.e. the current drawn by the chamber. The current drawn is determined by the number of electrons collected by the anodes after avalanche multiplication has occurred. This depends on the rate of particles incident on the cell, the number of ion pairs created in the drift space by each individual particle, and the gain of the chamber. The current drawn by a single anode strip is thus given by

$$I = Ae \sum_{counts} \frac{\delta E_i}{W} \tag{6.3}$$

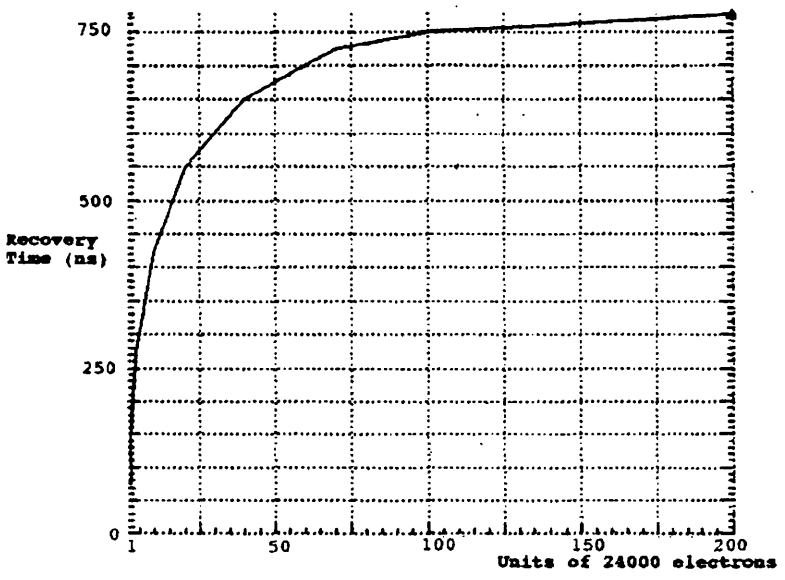

Figure 6.1: Dead time of proposed MSGC pre-amplifier as a function of number of input electrons. [45]

where δE_i is the energy deposited by each event on a single strip, A is the gain, e is the electronic charge and W is the energy required to create a single ion pair. The summation in eq. 6.3 is now taken over all events having one or more electrons deposited in the drift space and not only those above a certain discriminator setting. The gain of the chamber is assumed to be 3000 and the energy required to create a single ion pair is 26 eV. A mip is assumed to deposit 750 eV in a single strip.

The results from these calculations are presented in Table 6.9. We see that neutron-induced energy depositions result in a large increase in the current drawn by the chamber. This increase is due to the very large energy depositions arising from scattered ions. The Monte Carlo model predicts that such ions may deposit more than 1 MeV on a single strip, i.e. over three orders of magnitude greater than that deposited by a mip. Such large energy

	r = 40 cm		r = 100 cm	
	200 μm	300 μm	200 μm	300 μm
Mip rate (Hz cm^{-2})	7 $\times 10^5$	7 $\times 10^5$	1.2 $\times 10^5$	1.2 $\times 10^5$
Mip occupancy %	5.8	8.8	1.0	1.5
Neutron-induced rate Hz cm^{-2}	6000	5800	6000	5800
Neutron rate/ mip rate %	0.8	0.8	4.9	4.8
Neutron-induced occupancy %	0.07	0.09	0.07	0.09
% Increase in occupancy due to neutrons	1.2	1.0	7.0	6.0

Table 6.8: Increased occupancy of MSGCs due to neutron induced interactions in the chamber.(Au electrodes, pitches 200 μm, 300 μm, centre of chamber)

depositions produce very large numbers of electrons in the drift space resulting in the large ion loading predicted by the model.

Increased ion loading may lead to operational problems. Erosion of the strips may become more serious due to the larger numbers of charged particles incident on them. The formation of deposits on the electrodes may also become more of a problem because quenching of the large number of photons generated by large energy depositions will produce many more dissociated quencher molecules which may polymerize on the surface of the electrodes.

	r = 40 cm		r = 100 cm	
	200 μm	300 μm	200 μm	300 μm
Mip-induced current (nA $strip^{-1}$)	3.0	4.6	0.5	0.8
Neutron-induced current (nA $strip^{-1}$)	0.8	1.4	0.8	1.4
Increase in current %	27	30	160	175

Table 6.9: Increased ion loading of MSGCs due to neutron induced interactions in the chamber.(Au electrodes, pitches 200 μm, 300 μm)

6.3 Summary

We have produced a Monte Carlo program to simulate the effects of neutron-induced processes in MSGCs. We have demonstrated that the model gives good agreement with experimental results obtained from neutron irradiation studies of a MSGC test chamber at ISIS and thus have confidence that we have correctly identified and modelled the important neutron-induced processes. We have used the model to simulate the effects of neutron-induced processes at ATLAS using the proposed MSGC design [43] and make the following predictions:

1. Gold electrodes used in the proposed MSGC will produce a much higher count rate due to the absorption of thermal neutrons and subsequent β emission. The count rate produced by β's from gold is over three orders of magnitude greater than the count rate that would be produced by aluminium electrodes.

2. The 2T magnetic field present in ATLAS will substantially reduce the count rate resulting from β and photon processes by constraining β's and electrons produced by Compton scattering and pair production to follow tight helical paths. The presence of

the magnetic field will little effect on the count rate due to scattered ions.

3. A larger count rate is predicted closer to the PEEK casing of the proposed MSGC modules due to scattering of light ions.

4. The count rate is expected to increase as the MSGC anode pitch decreases. In addition, the energy deposited on each strip will decrease as the anode pitch decreases.

5. The neutron-induced count rate will be between 0.8 and 4.9 % of the charged particle rate for MSGCs with anode pitch of 200 μm, the mean pitch proposed for ATLAS.

6. The occupancy of such MSGCs as a fraction of charged particle occupancy will vary from 1.2 % to 7 %.

7. The ion loading may present a problem for MSGCs in ATLAS as a result of large energy depositions by scattered ions. The increase in current drawn per strip as a fraction of that due to charged particles will be as much as 160 % for MSGCs with anode pitch of 200 μm.

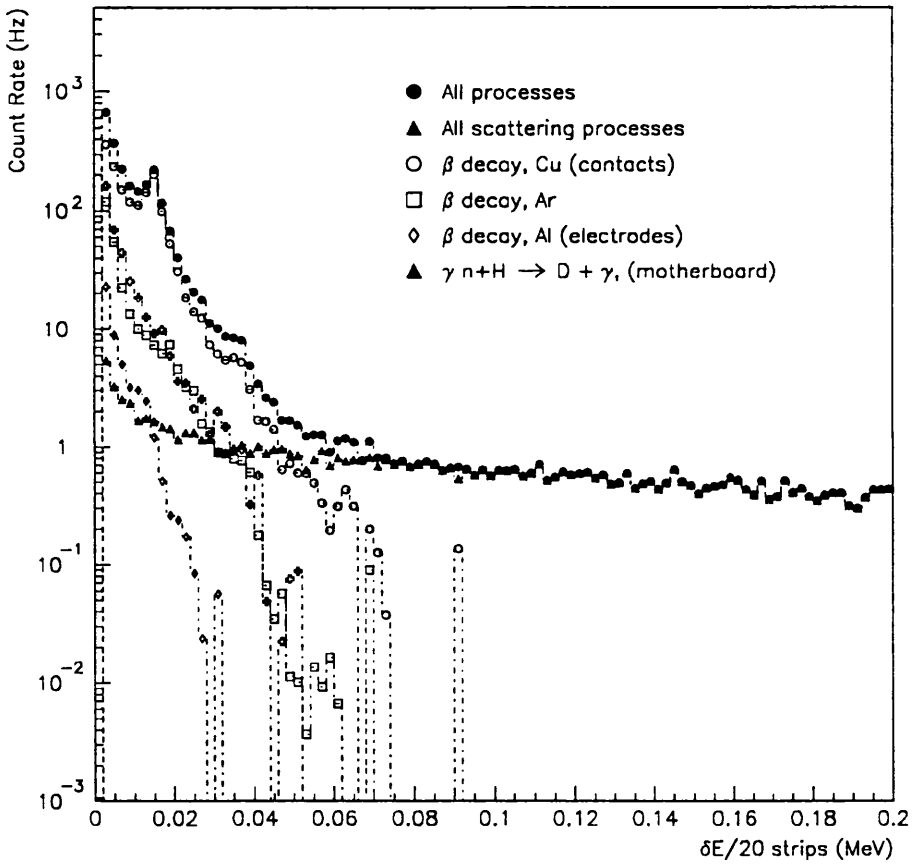

Figure 6.2: Monte Carlo simulation of neutron-induced energy depositions in MSGC filled with 75 % argon/25 % isobutane at ISIS. Neutrons || strips.

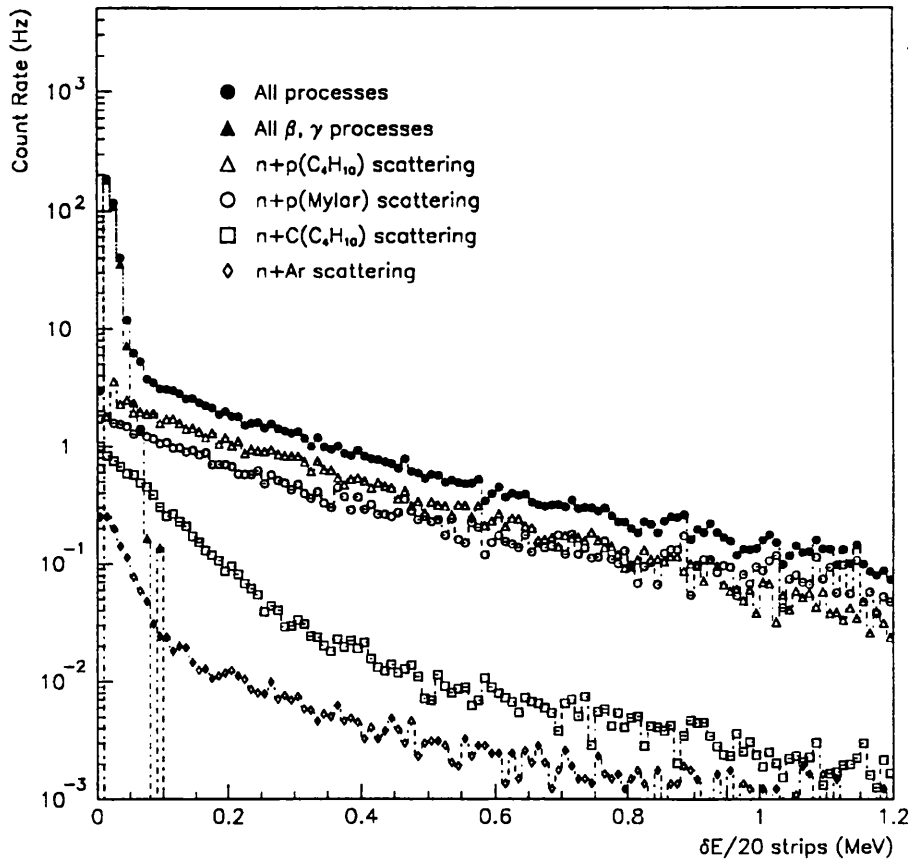

Figure 6.3: Monte Carlo simulation of neutron-induced energy depositions in MSGC filled with 75 % argon/25 % isobutane at ISIS. Neutrons || strips.

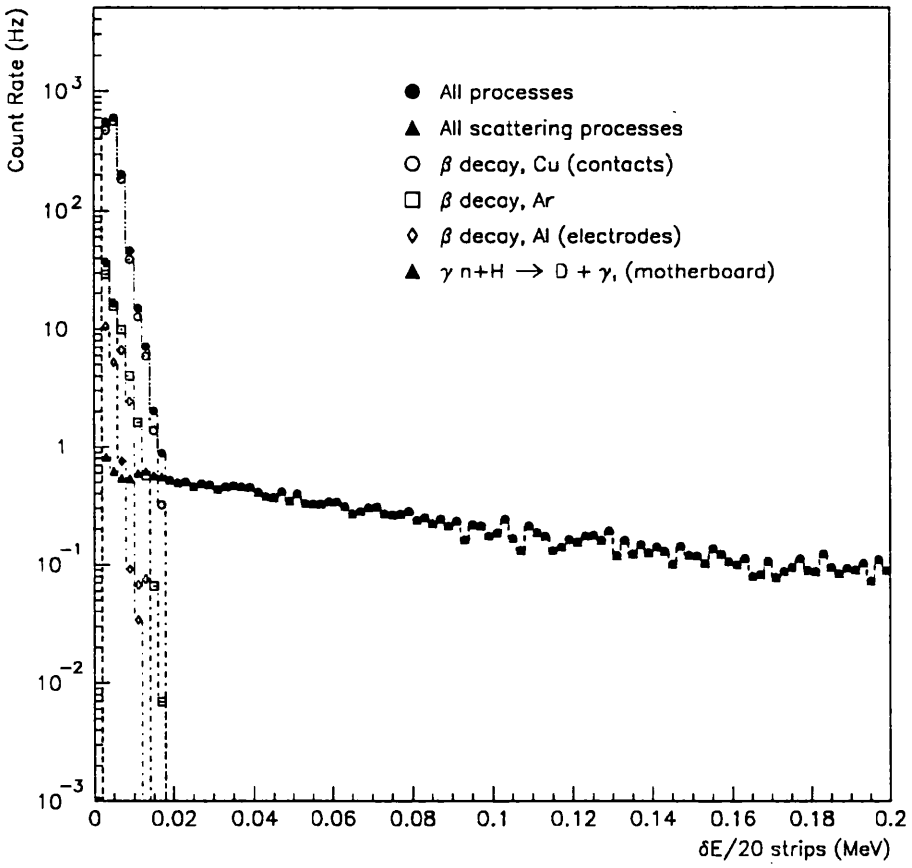

Figure 6.4: Monte Carlo simulation of neutron-induced energy depositions in MSGC filled with 50 % argon, 50 % CO_2 at ISIS. Neutrons || strips.

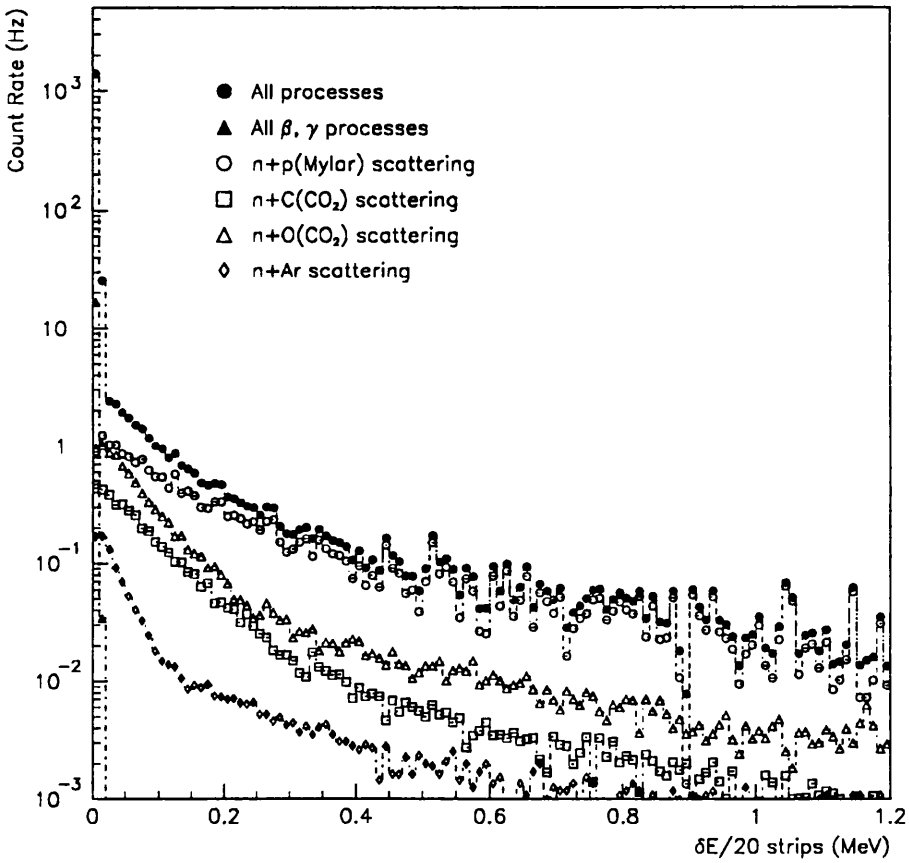

Figure 6.5: Monte Carlo simulation of neutron-induced energy depositions in MSGC filled with 50 % argon, 50 % CO_2 at ISIS. Neutrons || strips.

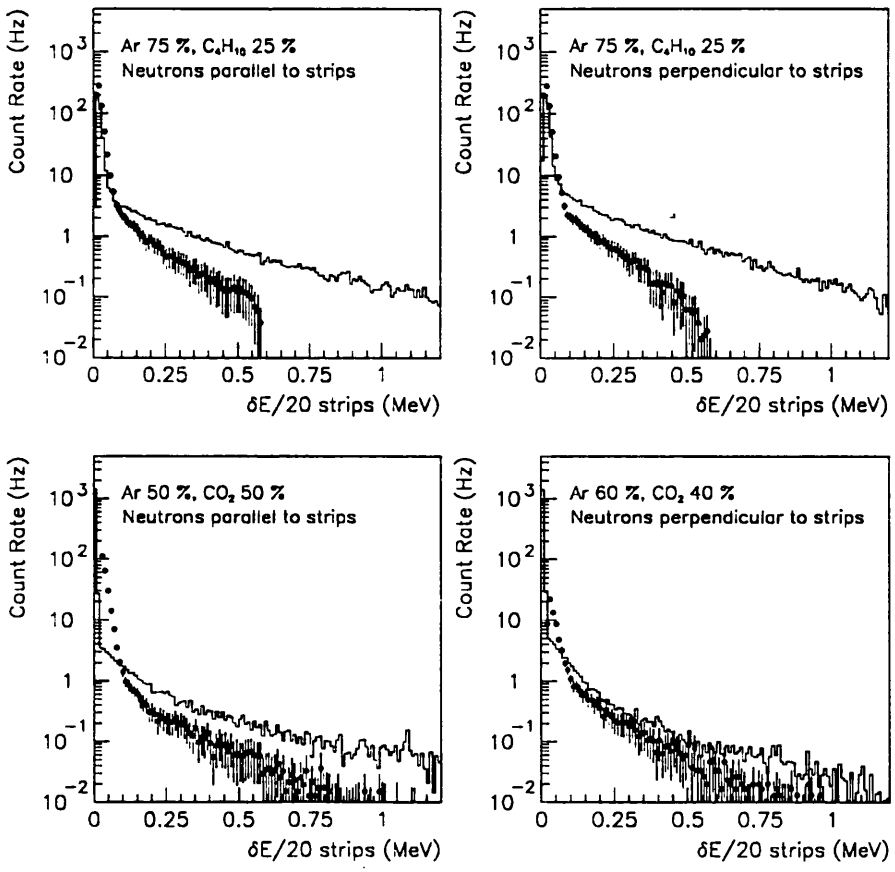

Figure 6.6: Comparison between Monte Carlo results (solid line) and ISIS experimental data for 4 different conditions.

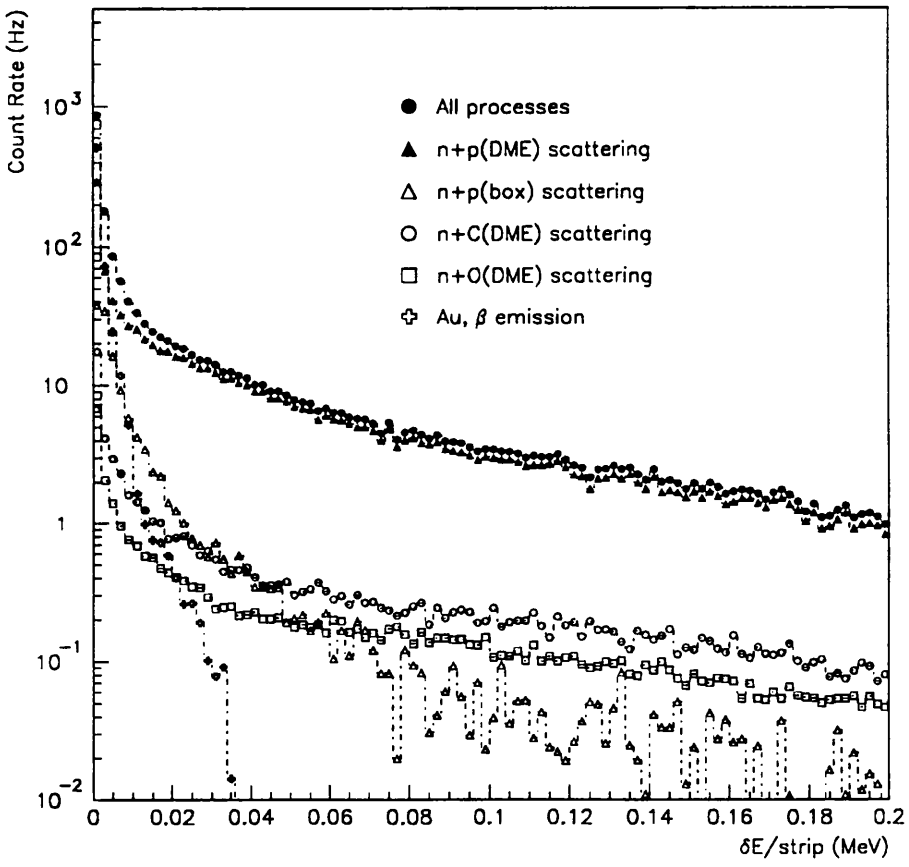

Figure 6.7: Monte Carlo simulation of neutron-induced energy depositions in MSGC filled with 50 % Argon/50 % DME at ATLAS. Au electrodes with 300 μm pitch.(E = 10 kV cm^{-1}, B = 2T).

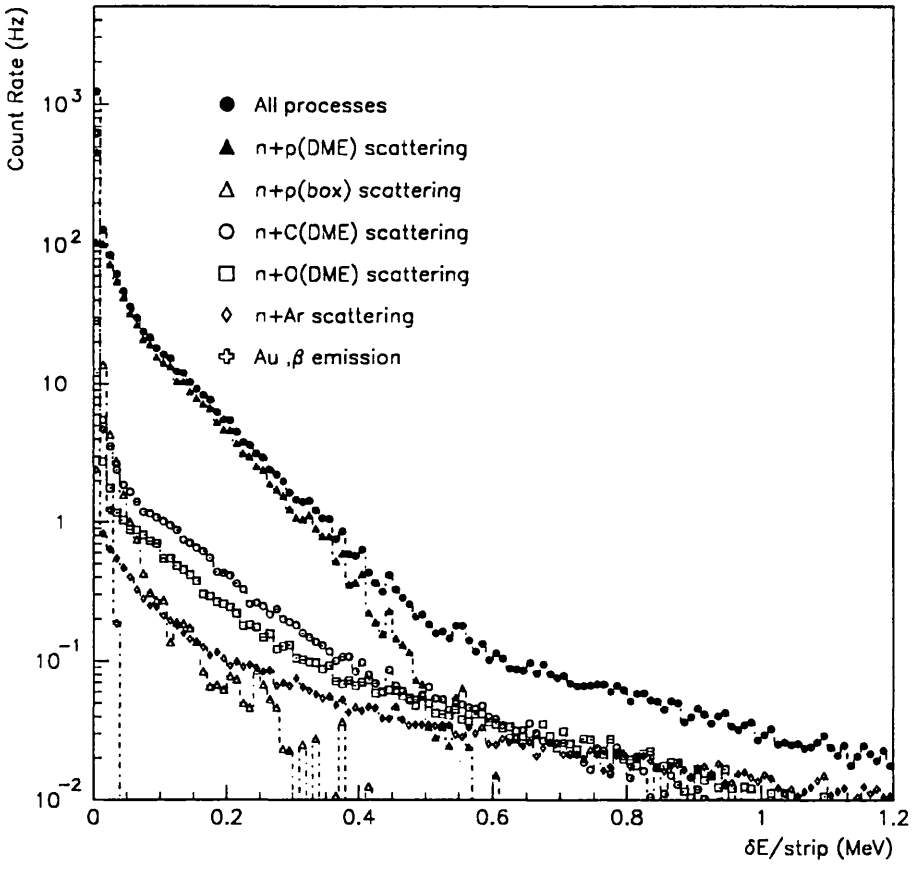

Figure 6.8: Monte Carlo simulation of neutron-induced energy depositions in MSGC filled with 50 % Argon/50 % DME at ATLAS. Au electrodes with 300 μm pitch.(E = 10 kV cm^{-1}, B = 2T).

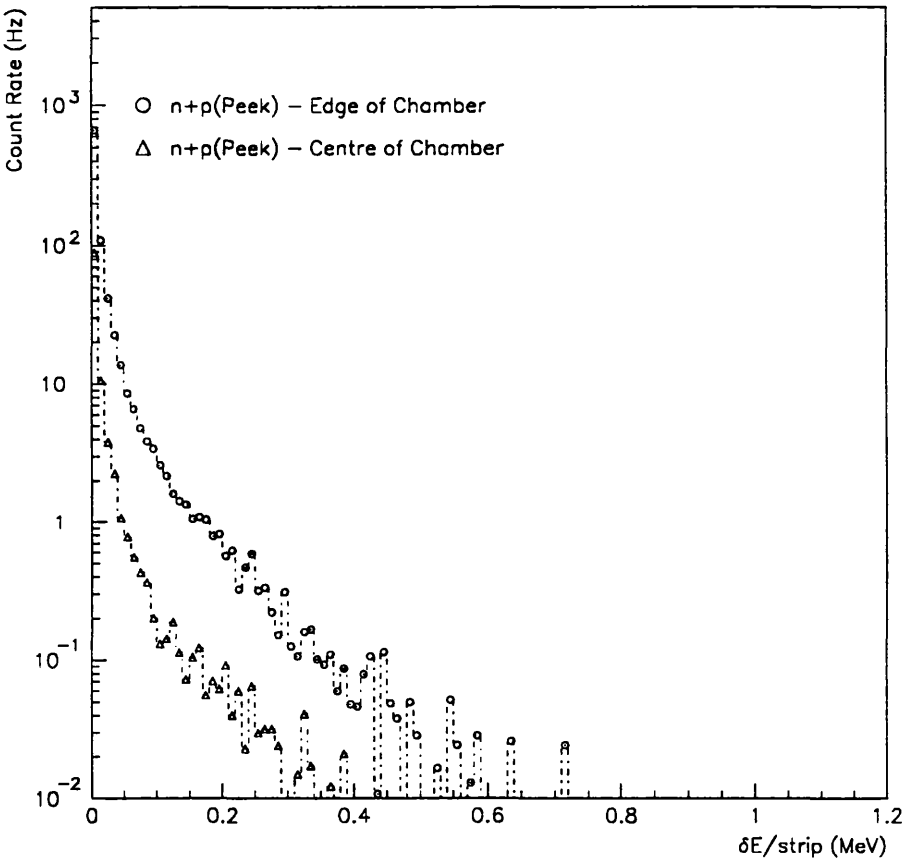

Figure 6.9: Monte Carlo simulation of neutron-induced energy depositions in MSGC filled with 50 % Argon/50 % DME in ATLAS. Au electrodes with 300 μm pitch.(E = 10 kV cm^{-1}, B = 2T).

Chapter 7

Conclusion

The inner detector at ATLAS will contain a high background flux of low energy neutrons arising from the surrounding calorimeters. In this work we have investigated some of the problems likely to be experienced by MSGCs, a particle detector proposed for use in the inner detector.

The results of an experiment at the ISIS proton synchrotron have been presented and a neutron-induced counting rate of $\sim$ 1 kHz cm^{-2} has been observed with energy depositions in the chamber due to neutrons exceeding 500 keV. A crude estimate of the neutron-induced counting rate in MSGCs expected at ATLAS based on these results was made.

The wide range of differences between the ISIS situation and that expected at ATLAS prompted the development of a Monte Carlo program to simulate the effects of neutron-induced processes in MSGCs. The model was compared with results obtained from the neutron irradiation experiments at ISIS and reasonable agreement was obtained. The model was then exploited to predict the effects on MSGCs of the neutron background predicted at ATLAS [30] using the proposed MSGC design [43] and used to calculate the increases in counting rate, occupancy and charge loading caused by such neutrons. The most important results obtained using the model are summarized here.

- The neutron-induced count rate in ATLAS will be between 0.8 and 4.9 % of the charged particle rate in the proposed ATLAS MSGC design [43].
- Based on work with the SPICE simulation [45], the neutron-induced occupancy of MSGCs as a fraction of charged particle occupancy is predicted to vary from 1.2 % to 7 % in ATLAS.
- The neutron-induced ion loading may present a problem for MSGCs in ATLAS as a result of large energy depositions by scattered ions. The increase in current drawn per strip as a fraction of that due to charged particles will be as much as 160 % for MSGCs with anode pitch of 200 μm.

We conclude from these predictions that the largest potential problem caused by the neutron background expected in ATLAS will come from the increased charge loading resulting from the large amounts of energy deposited in the chamber by scattered ions.

Bibliography

[1] ATLAS *Technical Proposal*, CERN/LHCC/94-43 (1994)

[2] ATLAS *Letter of Intent for a General-Purpose pp Experiment at the Large Hadron Collider at CERN*, CERN/LHCC/92-4 (1992)

[3] L. Didenko, B. Lund-Jensen *B-tagging of light Higgs Boson in Cascade Decays of Gluino*, Preprint (1994)

[4] F. Abe et al. *Evidence for top quark production in $p\bar{p}$ collisions at $\sqrt{s}$ = 1.8 TeV*, Phys. Rev. **D50** (1994) 2966

[5] CMS *Technical Proposal*, CERN/LHCC/94-38 (1994)

[6] ATLAS Collaboration *Staging/Down-grading of ATLAS*, (1993)

[7] RD28(UK) Collaboration *Proposal for a Prototype of a full MSGC Disc for the ATLAS Inner Detector*, (1993)

[8] A. Oed *Position-Sensitive Detector with Microstrip Anode for Electron Multiplication with Gases*, NIM **A263**(1988) 351

[9] R. Bouclier et al. *The Electrostatic Field in Microstrip Chambers*, Preprint (1992)

[10] G. D. Minakov *Performance of Gas Microstrip Chambers on Glass with Ionic and Electronic Conductivity.*, NIM **A326** (1993) 566

[11] J. E. Bateman, J. F. Conolly *Substrate-Induced Instability in Gas Microstrip Detectors.*, RAL-92-085 (1992)

[12] F. Angellini et. al. *The Micro-Gap Chamber*, NIM **A335** (1993) 69

[13] R. Bouclier et al. *High Flux Operation of Microstrip Gas Chambers on Glass and Plastic Supports*, CERN-PPE/92-53(1992)

[14] F. Sauli *Principles of Operation of Multiwire and Proportional Drift Chambers*, CERN 77-09 (1977)

[15] Particle Data Group *Review of Particle Properties*, Phys. Rev. D (1990)

[16] K. Kleinknecht *Detectors for Particle Radiation.* Cambridge University Press (1985)

[17] J. C. Giddings *Thesis: Electron Drift in the Zeus Central Tracking Detector*, (1992)

[18] V. Palladino, B. Sadoulet *Application of Classical Theory of Electrons in Gases to Drift Proportional Chambers*, NIM **128** (1975) 323

[19] M. Basile et al. *Dimethyl Ether Reviewed: New Results on using this gas in a High-Precision Drift Chamber*, NIM **A239** (1985) 497

[20] Y. Wang, G. Godfrey *Study of Dimethyl Ether for limited streamer tubes*, NIM **A320** (1992) 238

[21] T. McMahon *A study of the rate dependence of the gain of gas microstrip detectors with glass substrates in high intensity particle beams.*, NIM **A348** (1994) 293

[22] V. Grishkevich et. al. *MSGC on Substrates with modified Surface Resistivity*, ATLAS Internal Note INDET-NO-064 (1994)

[23] I. Duerdoth et al. *A Study of Breakdown in MicroStrip Gas Chambers*, NIM **A348** (1994) 356

[24] E. Bateman (Private communication)

[25] EG&G Ortec *Model 575A Amplifier, Operating and Service Manual.*

[26] EG&G Ortec *916A Hardware Manual.*

[27] G. R. Stephenson, J. S. Russ *Neutrons in Calorimeter Structures*, (1990)

[28] A. Ferrari et al. *Can we predict Radiation Levels in Calorimeters ?*, EAGLE Internal Note: CAL-N0-005 (1991)

[29] A. Ferrari *Update on Radiation Levels in the Inner Cavity*, (Unpublished 1994)

[30] A. Ferrari et al. *Background calculations for the ATLAS detector and hall*, ATLAS Internal Note GEN-NO-010(1994)

[31] J. Russ et. al Low-Energy Neutron Measurements in an Iron Calorimeter Structure Irradiated by 200 GeV/c Hadrons, CERN/TIS-RP/89-02 (1989)

[32] M. Edwards (Private communication)

[33] M. Edwards, D. R. Perry *The Radiation Hardness Test Facility.*, RAL-90-065 (1990)

[34] R. Stephenson *A low noise charge sensitive amplifier for use in vacuum photo-triode readout*, RAL-82-082

[35] Chilton, Shultis and Faw *Principles of Radiation Shielding*, Prentice Hall (1984)

[36] A. Romanov, S. Starodubtsev *The Passage of Charged Particles through Matter*, Jerusalem : Israel Program for Scientific Translations (1965)

[37] D. J. Hughes *Neutron Cross Sections*, (1955)

[38] J. B. Marion, J. L. Fowler *Fast Neutron Physics* , Interscience Publishers (1963)

[39] E. Segre *Nuclei and Particles*, Benjamin/Cummings (1977)

[40] R. J. Blin-Stoyle *Nuclear and Particle Physics*, (Chapman and Hall 1991)

[41] C. S. Wu, S. A. Moszkowski *Beta Decay* , Interscience Publishers (1966)

[42] R.M. Tennent *Science Data Book* Oliver & Boyd (1971)

[43] B. Payne et. al. *ATLAS Low mass MSGC design*, (Private communication)

[44] S. Snow (Private communication)

[45] L. Jones (Private communication)